博士論文

Development of Transparent Conducting Oxides with Improved Near-Infrared Transparency

（近赤外透過性に優れた透明導電性酸化物の開発）

中 尾　祥 一 郎

Abstract

Transparent conductive oxides such as In_2O_3, SnO_2, and ZnO are important materials for practical use in sustainable technologies: renewable energy production and energy saving technologies. In particular, doped SnO_2 thin films have been widely used as transparent electrodes of photovoltaic cells (PVCs) because of their desirable characteristics, which include excellent transparent conductive properties, low material and production costs, durability against reducing ambient, and availability on a mass-production scale. A crucial challenge for this application is to widen the transparent windows of SnO_2 films for next-generation PVCs that utilize the near-infrared (NIR) region of sunlight. In this study, I aimed to make clear the guiding principle of materials design for high mobility (μ_H) SnO_2 films with low carrier density (n_e) for transparency in the full ultraviolet-to-NIR spectrum of sunlight. I set the goal of this study to achieve a μ_H value of 80 $cm^2V^{-1}s^{-1}$ at $n_e = 1 \times 10^{20}$ cm^{-3}, which should yield free carrier absorption at 1400 nm less than 5%. I used pulsed laser deposition for film growth because of its suitability for exploratory studies. I first compared the transport properties of randomly oriented polycrystalline Ta-doped SnO_2 (TTO) films on glass substrates with those of epitaxial TTO films on Al_2O_3 (0001) substrates. The polycrystalline TTO films yielded much lower μ_H values than the epitaxial TTO films, suggesting that the high-angle grain boundary in polycrystalline films significantly suppresses μ_H. On the basis of this result, I conceived the idea that the use of appropriate seed layers would realize epitaxial growth of SnO_2 on glass substrates, and may enhance the μ_H of SnO_2 films. This idea was first tested by using materials that are

isostructural to SnO_2, rutile TiO_2 and NbO_2, as the seed layers. Consequently, 10-nm-thick rutile TiO_2 and NbO_2 seed layers on glass substrates were found to promote (110)-preferred growth of TTO. Furthermore, the TTO films grown on the seed layers showed high μ_H values of 66–68 $cm^2V^{-1}s^{-1}$, which are comparable with those of the epitaxial TTO films on Al_2O_3 (0001) substrates. These results clearly demonstrate that the seed layer method is effective for achieving high μ_H for SnO_2 films. Then, I expanded material exploration for the seed layer from rutile oxides to binary oxides with several selection criteria: oriented growth, high crystallinity, large grain size, availability, and nontoxicity. As a result, I found that anatase TiO_2 seed layers unexpectedly promote (100)-preferred growth of SnO_2. Furthermore, optimized TTO films on the anatase TiO_2 seed layers exhibited very high μ_H values of 83 $cm^2V^{-1}s^{-1}$ at $n_e = 2.7 \times 10^{20}$ cm^{-3}. Although this μ_H value slightly exceeded the target value of 80 $cm^2V^{-1}s^{-1}$, the n_e was too high to obtain the target NIR transparency. In order to obtain SnO_2 films with further reduced n_e and potentially enhanced μ_H, I took two approaches: dopant optimization, and the use of seed layers with complex composition. I explored several elements for a potential dopant that enhances not only n_e, but also μ_H. Consequently, I found that W-doped SnO_2 (WTO) films exhibited slightly better μ_H than TTO films. Finally, I extended material exploration for the seed layer of SnO_2 from binary oxides to ternary oxides. Using rutile $(Ti,Nb)O_2$ (TNO) solid solutions, I investigated the effects of lattice matching on the structure and transport properties of WTO films. The WTO films grown on heavily alloyed TNO seed layers showed (001)-oriented growth, which was probably realized by epitaxially stabilized (001) nuclei owing to a-axis matching of TNO to SnO_2. The WTO films with (001)-oriented growth exhibited an overwhelmingly

high μ_H value of 136 $cm^2V^{-1}s^{-1}$ at $n_e = 1.4 \times 10^{20}$ cm^{-3}. This μ_H value is 70% higher than the target value of 80 $cm^2V^{-1}s^{-1}$, which suggests that high μ_H values exceeding 80 $cm^2V^{-1}s^{-1}$ might be achieved for SnO_2 films, even if they were fabricated in disadvantageous processes, such as low-temperature deposition and sputtering. As a consequence of very high μ_H with reduced n_e, the WTO films with low sheet resistances of approximately 10 $\Omega sq.^{-1}$ exhibited low absorptions of 3.5% at a wavelength of 1400 nm. These properties sufficiently meet the requirement for the electrodes of next-generation full-spectrum PVCs.

List of Abbreviations

AFM: Atomic force microscope

CSP: Crystallographic shear plane

CVD: Chemical vapor deposition

FTO: F-doped SnO_2

ITO: Indium tin oxide

NIR: Near infrared

PLD: Pulsed laser deposition

PVC: Photovoltaic cell

PVD: Physical vapor deposition

TCO: Transparent conductive oxide

TEM: Transmission electron microscopy

TNO: $Ti_{1-z}Nb_zO_2$

TTO: Ta-doped SnO_2, $Sn_{1-x}Ta_xO_2$

WTO: W-doped SnO_2, $Sn_{1-y}W_yO_2$

XRD: X-ray diffraction

n_e: Carrier density

μ_H: Hall mobility

ω_p: Plasma frequency

ρ: Resistivity

R_s: Sheet resistance

Contents

Chapter 1 General Introduction

1.1 Introduction

We are living in an age where a historical turning point has been reached. It is an age where sustainable technologies have overtaken mass consumption, as predicted by Alvin Toffler in "The Third Wave" more than 30 years ago. From that perspective, modern sustainable technologies can be even regarded as a 21th century steam engine or agriculture. In this study, I have developed an essential material for use in sustainable technologies. It is a new class of transparent conducting oxides (TCOs). More specifically, it is a TCO that can transmit the full ultraviolet-to-near-infrared (NIR) spectrum of sunlight.

TCOs [1, 2, 3, 4, 5, 6] are degenerately doped wide-gap oxide semiconductors that exhibit both high electrical conductivity and transparency in the visible light region. Owing to those valuable properties, which are usually incompatible in a material, TCOs have been and will be essential for sustainable technologies [7]. For example, a TCO-based energy-saving window coating, or low-emissivity glass, can reduce the amount of energy used to air condition a building. White light-emitting diodes using TCO electrodes are gradually replacing electric light bulbs, leading to dramatically reduced power consumption. The Nobel Prize in Physics for 2014 was awarded to I. Akasaki, H. Amano, and S. Nakamura “for the invention of efficient blue light-emitting diodes which has enabled bright and energy-saving white light sources". Flat-panel displays such as liquid crystal displays and plasma panels have already replaced CRT displays, which were heavy, bulky, and

consumed a large amount of energy. This innovation in display technology was impossible without the development of transparent electrodes that utilize TCOs.

TCOs play a critical role in not only reducing energy consumption, but also producing renewable energy. Photovoltaic cells (PVCs), or solar cells, are among the most important pieces of technology capable of producing renewable energy. PVCs offer access to a ubiquitous energy supply on the earth, unlike other renewable energy such as wind, geothermal, biomass, and hydropower. Furthermore, PVCs allow us to harvest energy from outer space. It is true that energy produced in space is currently limited to self-consumption, but it could be an infinite energy source if microwave power transmission from space to the earth were to be realized. Thus far, various studies have been carried out in order to obtain PVCs with better performance and/or more affordable cost. Because transparent electrodes using TCOs significantly influence both the performance and cost [8] of PVCs, TCOs play an important role in PVC technology. In fact, improved TCOs are frequently cited as the future technical challenges for PVCs in Roadmap PV2030+ [7] by the New Energy and Industrial Technology Development Organization.

In this study, I successfully fabricated TCOs with improved NIR transparency. This development, which was even nominated as a long-term issue in PV2030+, will significantly contribute to improving the conversion efficiency of emerging full-spectrum PVCs: PVCs that utilize not only visible light but also the NIR region of sunlight. In the remainder of this chapter, a detailed background of this study is reviewed, followed by descriptions of strategy, aim, and the outline of this work.

1.2 Transparent Conductive Oxides

In general, transparency and conductivity cannot coexist in a material. Typical transparent materials such as glass and plastic are insulators, whereas conducting materials like metals are nontransparent. However, contrary to this naive knowledge, both transparency and conductivity can be obtained in exceptional materials known as TCOs. TCOs are degenerately doped wide-gap oxides semiconductors such as SnO_2, ZnO, and In_2O_3. Sn-doped In_2O_3 (indium tin oxide, ITO) has excellent properties among TCOs, and as a result has become very widely used in the industry. In fact, it is so widely used that ITO is sometimes regarded as a synonym for TCO. In addition to the three well-known compounds mentioned above, CdO, Ga_2O_3, and alloys of these materials have been investigated. To date, typical TCOs exclusively show n-type conduction. In spite of many efforts, practical p-type TCOs are yet to be discovered [9]; the conductivity of present p-type TCOs is one or two orders of magnitude lower than that of n-type TCOs, and is therefore insufficient for many applications. Although various non-oxides such as nitride (Zn_3N_2 and GaN), graphene, and metal nanowires have been extensively studied, it might take a long time to apply these materials to devices. In this study, I focus on n-type TCOs.

The mechanism behind the coexistence of transparency and conductivity in TCOs can be summarized as follows. Figure 1.1(a) shows the band structure of TCOs and their parent compounds, which are undoped wide-gap oxide semiconductors. The conduction band of TCOs and their parent compounds mainly consist of the s-orbital of cations, whereas the valence band is derived from the p-orbital of oxygen. The band gap, which is typically above 3 eV, is wide enough to prohibit visible-light absorption due to the

interband transition. Thus, in thin film form where the scattering of light is insignificant, the parent compounds of TCOs are transparent to visible light.

In principle, the origin of transparency, namely the wide band gap, is unfavorable to electrical conductivity because thermal excitation of carriers at room temperature is nearly impossible. Indeed, "pure" parent compounds such as ZnO, SnO_2, and Ga_2O_3 are highly resistive. However, the donor levels of certain dopants for these compounds can be set very close to the bottom of the conduction band, as shown in Fig. 1.1(b). Similar to typical elemental semiconductors such as Si and Ge, the shallow donor levels form an impurity band at low doping levels, which involve highly increased conductivity. As doping proceeds, the impurity band grows up and finally merges into the conduction band minimum, as shown in Fig. 1.1(c). Consequently, the Fermi level lies inside the conduction band, resulting in metallic conduction. Such heavily doped semiconductors with metallic conduction are called degenerate semiconductors.

It should be noted that the interband transition yields no visible light absorption in the degenerately doped state and the undoped state. Strictly speaking, the photon energy for the interband transition even shifts to a slightly higher energy level because the endpoint of the transition is not the conduction band minimum, but the Fermi level. This phenomenon, which is known as the Burstein–Moss shift [10, 11], is very important for materials with a relatively narrow band gap, such as CdO. As far as interband absorption is concerned, the transparent nature of the parent compound survives even in the degenerately doped state.

The transparency of TCOs is then determined by two components other than the interband absorption: ingap absorption and the optical response of the free carrier. The ingap absorption is rather difficult to analyze because its origin is often unknown.

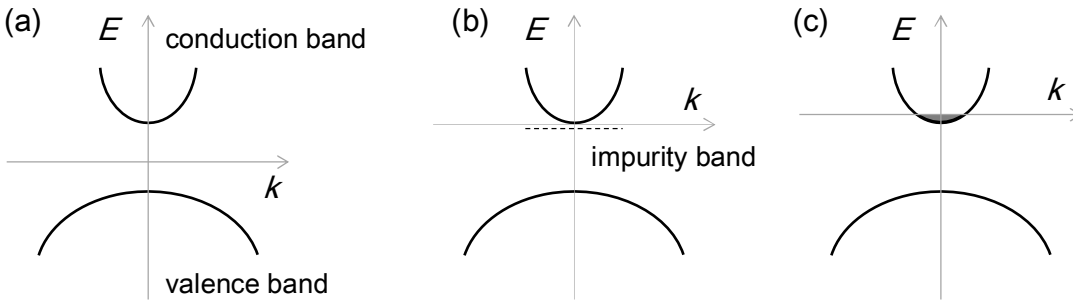

Fig. 1.1. Schematic drawings of band structures of (a) undoped, (b) non-degenerately doped, and (c) degenerately doped wide-gap oxide semiconductors.

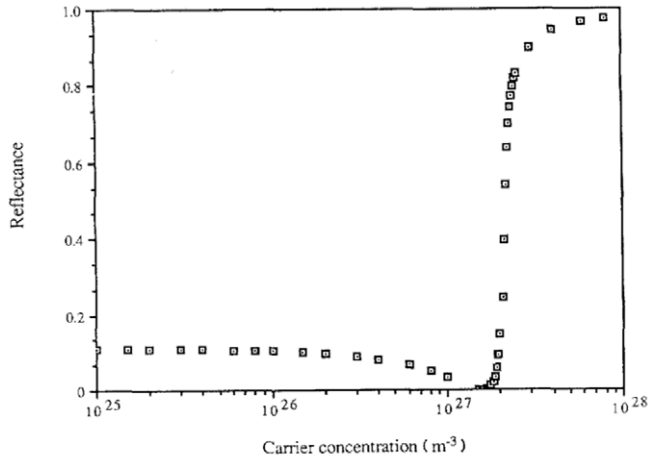

Fig. 1.2. Calculated reflectance at 800 nm as a function of carrier concentration assuming the Drude model [13]. (Copyright (1992) Chapman & Hall)

Fortunately, the intensity of ingap absorption is usually so weak that, in many cases, only the optical response of the free carrier is considered.

The Drude model successfully reproduces the optical response of free carriers in solids such as metals and semiconductors. It is well established that the optical properties of TCOs can be explained by the Drude model as well [12]. In short, an electromagnetic wave whose energy is below a certain threshold value cannot penetrate into solids, resulting in perfect reflection. On the other hand, above the threshold energy, the solid transduces the light. The threshold value, which is called the plasma frequency (ω_p), is determined by the carrier density (n_e) of solids in the following formula,

$$\omega_p^2 = (n_e q^2)/(m^* \varepsilon_o \varepsilon_\infty), \tag{1-1}$$

where q, m^*, ε_o, and ε_∞ are the electric charge, the effective mass of the electron, the permittivity of free space, and the high-frequency permittivity, respectively. Frequently, the wavelength at ω_p, or plasma wavelength,

$$\lambda_p = 2\pi c_0/\omega_p, \tag{1-2}$$

where c_0 is the speed of light, is used to describe the optical properties of solids. From (1-1) and (1-2), λ_p is inversely proportional to the square root of n_e. Thus, λ_p shifts to a shorter wavelength region with an increase in n_e. The origin of the shiny appearance of metals, i.e., the mirror reflection of visible light, is a consequence of the short λ_p below 400 nm due to

high n_e (~10^{22} cm^{-3}) of the metals. In order to achieve visible light transparency, λ_p should be above 800 nm. This requirement limits n_e values for TCOs. As shown in Fig. 1.2, Bellingham et al. [13] reported that the calculated limit for ITO and typical TCOs is approximately 2×10^{21} cm^{-3}, which is one order of magnitude lower than that for typical metals.

The (simple) Drude model predicts some unrealistic features, such as 100% reflection at the wavelength above λ_p (Fig. 1.2), and no optical absorption. Considering dissipation, which is the scattering of carriers, resolves the discrepancy with experimental data, leading to a successful quantitative analysis. The Lorenz oscillator model is used to include the dissipation term, where the relaxation time of carriers, τ_{opt}, is the parameter. This model reproduces two characteristic features: smeared spectra and free carrier absorption (FCA). At ω_p, rapid oscillations of the electron density, i.e., plasma oscillation occurs due to the nature of resonance. Thus, the dissipation is maximal at ω_p, resulting in FCA with peak at ω_p. As shown later, FCA leads to optical absorption in the visible light range, albeit ω_p above 800 nm.

It should be stressed here that τ_{opt} is closely related to DC electrical properties. Resistivity (ρ) is written as

$$1/\rho = qn_e\mu_H, \tag{1-3}$$

where μ_H is Hall mobility. From the Drude model for DC conductivity, μ_H is written as

$$\mu_H = q\tau/m^*, \tag{1-4}$$

where τ is the relaxation time for DC current. The length scales for the two relaxation times are considerably different from each other. Surprisingly, τ_{opt} deduced from optical spectra and τ determined from transport measurements sometimes agree with each other, as shown in Fig. 1.3 [14, 15]. This phenomenon is frequently observed for TCOs with high n_e values of approximately 10^{21} cm^{-3} [14, 15, 16, 17], indicating that intra-grain scattering, such as ionized impurity scattering, is a dominant factor for τ. On the other hand, TCOs with low n_e values of approximately 10^{20} cm^{-3} generally show different behavior; τ is shorter than τ_{opt}. This is because inter-grain scattering, such as grain boundary scattering, significantly contributes to τ. A detailed description and formula for scattering in carrier transport in TCOs are given in appendix A.

The dominant role of grain boundary scattering for μ_H in TCOs with low n_e has been frequently pointed out in many studies [6, 18]. The grain boundary scattering in polycrystalline semiconductors was successfully formulated by Seto in 1975 [19]. As shown in Fig. 1.4, in the model dangling bonds at grain boundary trap electrons or holes. Due to charge trapping, thin depletion layers are formed near the grain boundary. The charged grain boundary and the depletion layers result in the formation of a double Schottky barrier at the grain boundary. The barrier height increases with the increase in accumulated charge at the grain boundary, and thus shows the maximum at the doping concentration where the dangling-bonds are filled completely. Further increase in doping concentration reduces the barrier height due to the increase in the Fermi energy and thinned

depletion layers. Consequently, the Seto model predicts a dip structure in the n_e-μ_H plot, which has been experimentally observed in polycrystalline Si thin films. The position of the dip, or n_e at which the minimum μ_H value appears, reflects the trap density. Many researchers consider that the Seto model depicts (at least qualitatively) the physics behind the grain boundary scattering in TCOs, as well as the elemental semiconductors. The increase in μ_H at the low n_e region in the n_e-μ_H plot for TCOs is regarded as a recovery of μ_H. This is due to enhanced screening of the fully charged grain boundaries with the increase in n_e.

Now we turn to the optical properties of TCOs again. As shown above, the optical properties of TCOs are closely related to the electrical properties. This means that two fundamental properties of TCOs, electrical and optical properties, cannot be tuned independently. As shown in Fig. 1.5, Coutts et al. simulated the optical spectra of TCOs with various electrical properties to visualize this issue [20]. Figure 1.5(a) clearly demonstrates that the transparent "window" of TCO, i.e., the transparent region of the spectra is determined by n_e. In many applications (such as PVCs), absorption should be as low as possible in order to improve the efficiency of the application. For this purpose, it is better to set λ_p as long as possible, as shown in Fig. 1.5(b). Because FCA is a consequence of dissipation due to scattering of carriers, increased μ_H leads to reduced FCA. Although the simulation in Fig. 1.5(b) adopted some unrealistic μ_H values, such as 500 $cm^2V^{-1}s^{-1}$ and 1000 $cm^2V^{-1}s^{-1}$, the difference between FCA for 50 $cm^2V^{-1}s^{-1}$ and 100 $cm^2V^{-1}s^{-1}$ is clear. It should be noted that while both reduced n_e and increased μ_H are favorable for transparency, the former is unfavorable for conductivity. However, the increase in μ_H is limited by

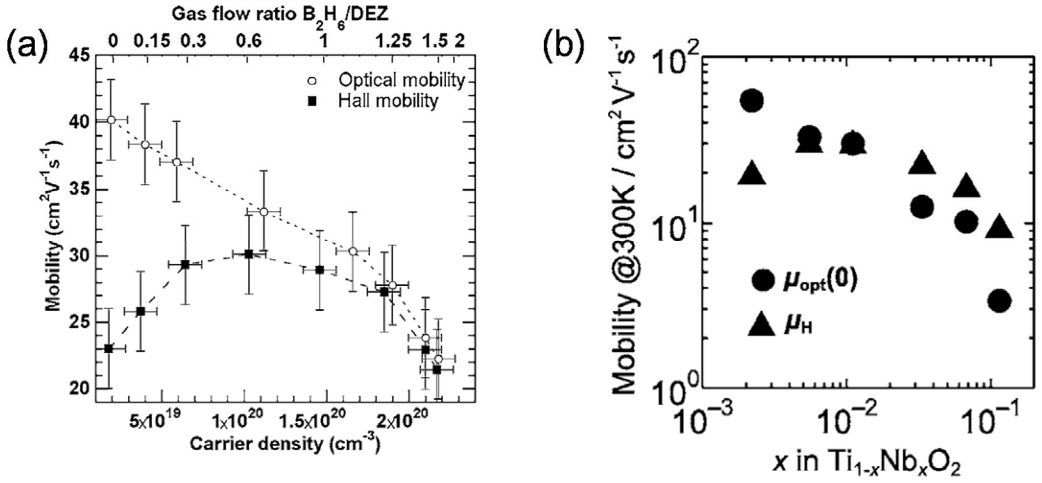

Fig. 1.3. Comparison between Hall mobility and optical mobility in (a) CVD B:ZnO films on glass substrates [14] (Copyright (2007) AIP Publishing LLC) and (b) PLD Nb:TiO_2 films on $SrTiO_3$ substrates [15] (Copyright (2007) AIP Publishing LLC).

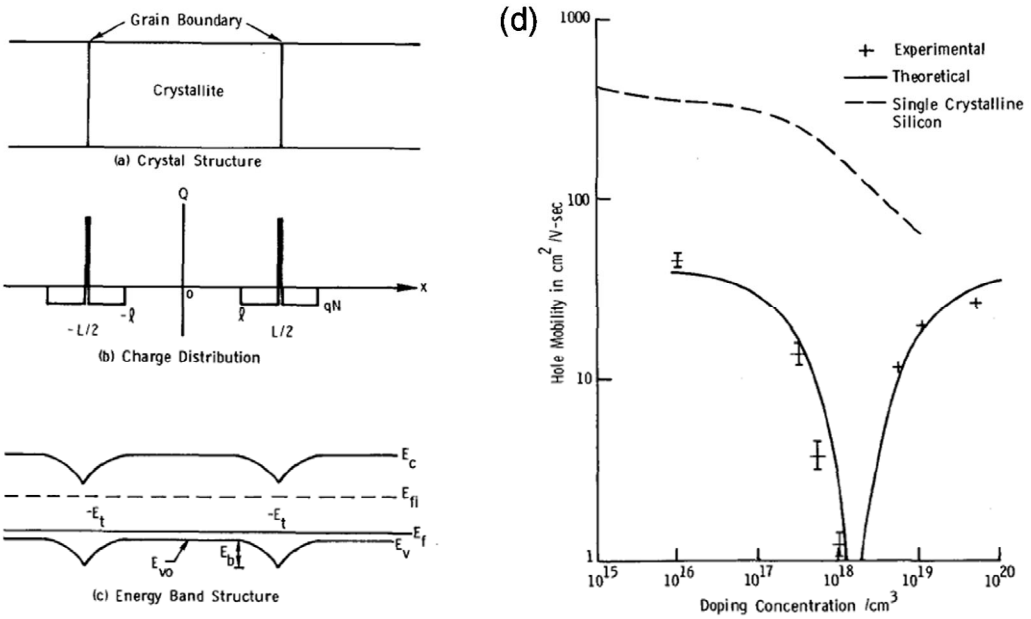

Fig. 1.4. (a) Model for the crystal structure of polycrystalline Si films. (b) The charge distribution within the crystallite and at the grain boundary. (c) The energy band structure for polysilicon crystallites. (d) Room-temperature hole Hall mobility vs doping concentration. The experimental result is plotted together with the theoretical solid curve. The broken line is data for single crystal Si [19] (Copyright (1975) AIP Publishing LLC).

intrinsic scattering, such as phonon scattering and ionized impurity scattering. In other words, no “best” TCO exists. Appropriate values for n_e and μ_H are chosen in order to satisfy the required electrical and optical properties for a specific application. The n_e and μ_H values targeted in this study will be presented later in this chapter.

In actual applications, ρ is not a good quantity to evaluate the electrical performance of TCOs. Instead, sheet resistance,

$$R_s = \rho / t, \tag{1-5}$$

where t is the film thickness, is used instead. Electrodes for PVCs transmit high current density and therefore require very low R_s in order to reduce losses due to joule heating. On the other hand, high R_s values are sufficient for some applications, such as antistatic coatings.

1.3 Transparent Conductive Oxides in Photovoltaics Cells

To date, several types of PVCs have been developed. Only exceptional PVCs where the active layer has a sufficiently low R_s value require no transparent electrodes; instead, metal comb electrodes are used for such PVCs. In general, the electrical and optical properties of TCOs are critical to the conversion efficiency of PVCs. For example, optical loss due to absorption of TCOs directly reduces short circuit current. Thus, absorption of TCOs should be as low as possible in the wavelength region where PVCs work. High R_s

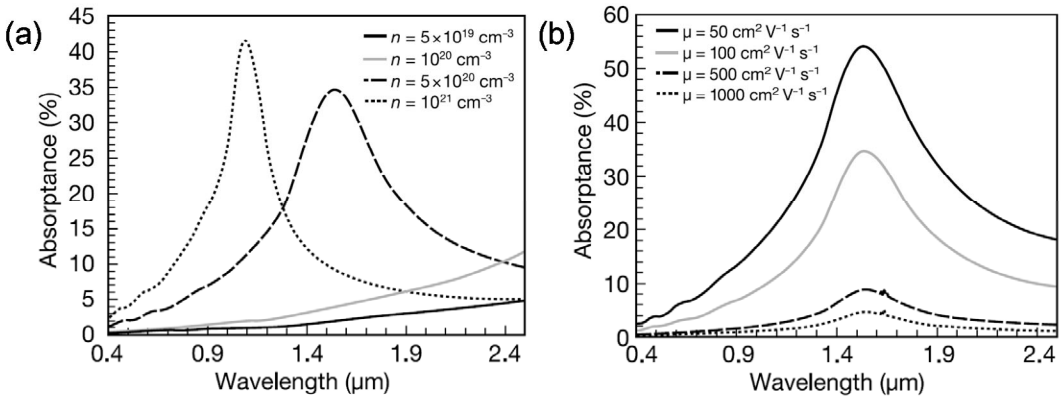

Fig. 1.5. Simulated free carrier absorption (a) with various n_e at fixed μ_H of 100 $cm^2V^{-1}s^{-1}$ and film thickness of 500 nm and (b) with various μ_H at fixed n_e of 5×10^{20} cm^{-3} [20] (Copyright (2000) Cambridge University Press).

Table 1.1. Various TCOs employed in photovoltaics devices [21] (Copyright (2007) Cambridge University Press).

Cell Type	TCO in Current Use	TCO Needs	Materials Goals
Heterojunction with intrinsic thin layer (HIT) cell	Indium tin oxide (ITO)	Smooth, good interfacial properties, very good conductivity, low-temperature deposition, light trapping	Indium zinc oxide (IZO), indium-free materials, ZnO
Copper indium gallium selenide (CIGS)	Intrinsic-ZnO/Al:ZnO	Interfacial stability to CdS, low-temperature deposition, resistance to diffusion and shorting, need to make/improve the junction	Single-layer TCO to replace two layers and CdS layer
CdTe	(SnO_2) Zn_2SnO_4/Cd_2SnO_4	Stable interface to CdS/CdTe at temperature, diffusion barrier	Doping of ZnSnOx materials, single-layer TCO
Nano-hybrid polymer cell	ZnO, SnO_2, TiO_2	Nanostructure with right length scale, work-function matching, interface with organic, correct doping level for carrier transport	Self-organized structures core–shell structures, new nonconventional TCOs
Grätzel cell	TiO_2	Nanostructure with high electron mobility	Improved TiO_2 morphology and possible use of doped materials, new non-TiO_2 materials
Amorphous Si	SnO_2, ITO, and ZnO; many cells employ two TCOs	Temperature stability, chemical stability, and appropriate texture for both TCO layers	Higher conductivity, texture, and ohmic contact for both TCO layers

values in TCOs reduce the fill factor through an increase in series resistance. A very low R_s value of approximately 10 $\Omega sq.^{-1}$ is required. In addition to the impact on the conversion efficiency, the cost for TCOs is rather high among the components of PVCs. For example, the cost of TCOs for dye-sensitized solar cells is estimated to be approximately 20% of the total production cost. Thus, improved TCOs with affordable cost are frequently cited as the future technical challenges for PVCs in Roadmap PV2030+.

In contrast to exclusive use of ITO in flat panel displays, various TCOs have been employed in PVCs, as listed in Table 1.1. This is because there are additional critical properties aside from electrical and optical properties. For example, PVCs with a substrate-type structure require TCOs with low process temperature because TCOs are deposited on the active layer. TCOs for thin-film silicon PVCs must endure the reductive atmosphere of atomic hydrogen, which is generated during the deposition of silicon. These types of requirements have led to the development of a variety of PVCs, which are listed in Table 1.

The problem addressed in this work is related to the fundamental challenge of high conversion efficiency: the realization of full spectrum PVCs. The conversion efficiency of the single-junction PVC has an intrinsic limitation known as the Shockley–Queisser limit [22]. In short, single-junction PVCs only use sunlight with energy higher than the energy-gap of the junction. Sunlight with longer wavelengths is discarded, resulting in the theoretical limit of a conversion efficiency of 33.7% for single junction PVCs. To overcome this limitation, multi-junction PVCs, or tandem solar cells, have been developed. In this structure, the low-energy sunlight unused by one junction is absorbed by the other junction. The low-energy sunlight is typically NIR light. Such PVCs have already been

commercialized as a-Si:H/μc-Si:H tandem PVCs, although NIR light only up to 1100 nm is used. Thus, the path forward to improve conversion efficiency is to utilize NIR light with a longer wavelength. The ideal form of multi-junction PVCs would utilize the full range of the sunlight spectrum, and therefore would be called full-spectrum PVCs. However, TCOs that have been optimized for full spectrum PVCs, or TCOs with improved transparency in the NIR region, are under development as reviewed below.

As stated in section 1.2, the first step is to consider the required R_s value and transparency, and to determine the targeted n_e and μ_H values. I have adopted the target values [23] set by the researchers of Asahi Glass Co., Ltd., which is the largest supplier of TCOs for thin film silicon solar cells. They considered that adding another junction of SiGe to a-Si:H/μc-Si:H tandem PVCs would extend the optical response above 1100 nm to approximately 1400 nm. From optical simulation, they concluded that in order to reduce absorption to less than 5% at 1400 nm with R_s = 12 Ωsq.$^{-1}$, TCOs with high μ_H values exceeding 80 cm^{2}V^{-1}s^{-1} at $n_e = 1 \times 10^{20}$ cm^{-3} are required. I consider this estimation by the authoritative company to be both realistic and important for future large-scale use, and I have therefore regarded μ_H = 80 cm^{2}V^{-1}s^{-1} as the milestone in this study.

As early as the year 2000, Coutts et al. pointed out the importance of μ_H for the optical properties of TCOs (Fig. 1.5). As described in section 1.2, a further decrease in ρ without increasing optical absorption is possible only by increasing μ_H. Coutts et al. explored such TCOs based on cadmium oxides like CdO and Cd_2SnO_4 [20]. However, cadmium oxides have two serious drawbacks: toxicity of Cd and narrow band-gap of CdO. In particular, the latter is a critical drawback to the PVC application.

Table 1.2. Deposition methods of impurity doped In_2O_3 with high μ_H [25] (Copyright (2010) Elsevier).

Dopant	Method	N (10^{20} cm^{-3})	μ (cm^{2}V^{-1}s^{-1})	ρ ($10^{-4}\Omega$ cm)	T_S (°C)
Mo	TRE	2.6	130	1.8	350
	RFMS	3.0	83	2.5	450[a]
	CSA	7.1	~18.3	4.8	350
	REHCS	4.1	80.3	1.9	290
	SP	4.98	~1.72	7.3	450
	Reactive DCMS	1.9	50	~5.0	350
	RFM co-sputtering	2.7	99	2.3	450[a]
	RFM co-sputtering	4.3	65.3	~2.22	550
	PLD	3.6	250	0.7	500
	Pulsed DCMS	5.0	77	1.6	500[b]
Ti	SPD	1.0	120	5.2	500
	REHCS	4.3	80.6	1.8	300
	Combinatorial RFMS	2.9	83.3	2.6	500
	DCMS	2.0	89.5	3.5	300
	PLD (quartz)	0.8	199	0.98	500
	RFMS + anneal	3.1	105	1.95	530
Zr	SP	0.8	170	4.6	500
	ALD	2.2	76	3.7	500
	RHCS	4.3	63.3	2.3	250
	PLD YSZ <111>	1.0	110	5.7	650
	RFMS	2.9	82	2.6	450
W	Reactive DCMS	4.0	57	2.7	380
	DCMS	2.9	73	3.0	300
	SP	2.4	26	10	525
	Reactive DCMS	2.8	67	2.8	320
	PLD (quartz)	~1.5	358	~1.1	500

Soon after the study by Coutts et al. was conducted, Meng et al. [24] reported high μ_H values exceeding 80 $cm^2V^{-1}s^{-1}$ in Mo-doped In_2O_3, deposited by thermal reactive evaporation. This finding triggered extensive exploration of dopants for high-μ_H In_2O_3 using various deposition methods, as listed in Table 1.2 [25]. Consequently, many elements other than Mo were found to effectively enhance μ_H in In_2O_3. These elements included W, Ti, Zr, and H. Furthermore, sputtering, which is the industrial method used for the deposition of ITO, was used in some of the studies. In particular, H-doped In_2O_3 exhibits an excellent μ_H value of 130 $cm^2V^{-1}s^{-1}$, with a low process temperature of approximately 200 °C [26, 27]. This unique feature makes it possible to deposit H-doped In_2O_3 on a-Si:H/c-Si heterojunction PVCs, resulting in the experimental demonstration of improved conversion efficiency by using NIR light [28].

At present, the mechanism behind improved μ_H in In_2O_3 by using the specific dopants remains unclear. In 2010, Calnan et al. reviewed experimental reports on high-μ_H In_2O_3 and proposed a hypothesis that the dopant elements with strong Lewis acid strength result in high μ_H [25]. However, this speculation fails to explain the excellent μ_H values obtained for H-doped In_2O_3. One possible explanation for this is the improved structural properties of H-doped In_2O_3, which were achieved by solid phase crystallization from amorphous precursors, with a significantly reduced population of crystalline nuclei [27].

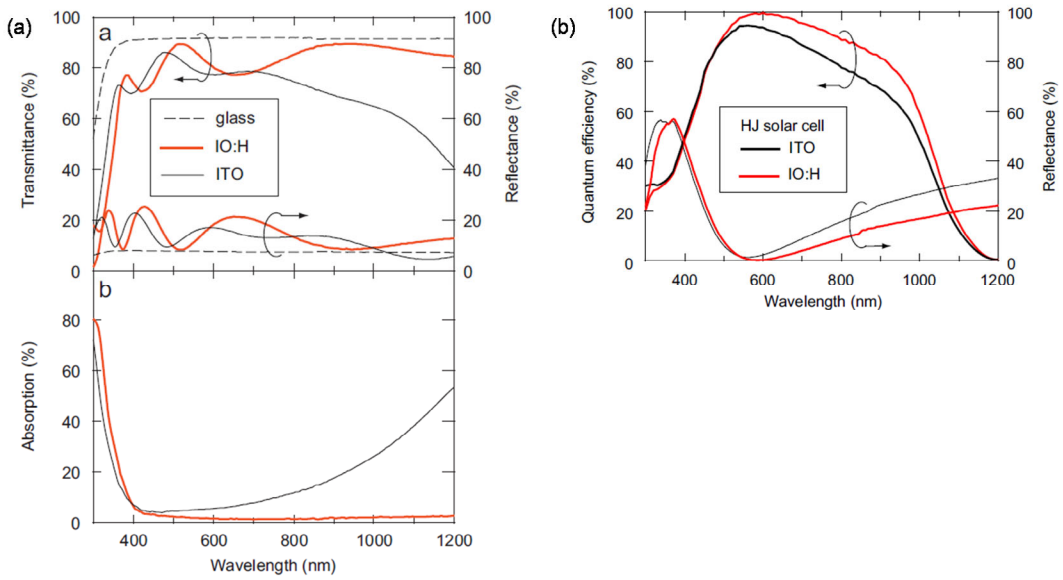

Fig. 1.6. (a) Optical properties of ITO and H-doped In_2O_3 and (b) external quantum efficiencies and reflectance of a-Si:H/c-Si heterojunction PVCs using ITO and H-doped In_2O_3 [28] (Copyright (2009) Elsevier).

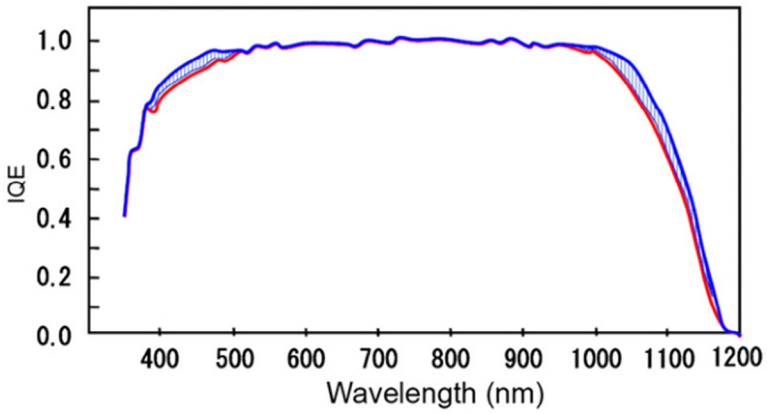

Fig. 1.7. Internal quantum efficiencies of a-Si:H/c-Si heterojunction PVCs [30] (Copyright (2011) Elsevier).

1.4 Search for High Mobility in SnO_2

As reviewed in the previous section, In_2O_3-based high-μ_H TCOs have already been developed. Several pioneering studies have shown the improved conversion efficiencies by using such TCOs. Furthermore, in 2014, the Panasonic Corporation demonstrated a record conversion efficiency of 25.6%, which was 0.6% higher than the previous record of PERL cells in 1999 for Si-based PVCs in module scale [29]. Although detailed information on their PVCs is still closed, improved TCOs with NIR transparency (which I speculate to be In_2O_3-based) were listed as one of the major breakthroughs [30]. As shown in Fig. 1.7, the internal quantum efficiency spectra showed improved efficiency in the NIR region from 1000–1200 nm. These studies [28, 30] clearly demonstrate that efficient use of NIR light is an effective method for improving conversion efficiency, and high-μ_H TCOs are critical to such PVCs.

Here it should be stressed that high-μ_H TCOs using parent compounds other than In_2O_3 are highly desirable because of the following drawbacks of In_2O_3. One group of drawbacks is related to In_2O_3 itself; namely, indium is an expensive and scarce element. This would be a considerable drawback for large-scale use in the future. In addition, the possible toxicity of In_2O_3 [31] may lead to lung cancer in those exposed to the material. As a result, the use of indium compounds has been strictly regulated in Japan since 2013. The other group of drawbacks is related to the requirements for device fabrication. As discussed in section 1.3, TCOs for PVCs require various properties, in addition to specific electrical

and the optical properties. One serious issue is the degraded transparency of In_2O_3 due to the reductive atmosphere of atomic hydrogen during Si deposition [6].

In this study, I focus on SnO_2-based TCOs, which are free from the drawbacks described above. SnO_2 crystallizes into the rutile structure with lattice parameters of a = 0.4738 nm and c = 0.3187 nm, as shown in Fig. 1.8(a). SnO_6 octahedrons are linked with each other by corner- and edge-sharing along the a- and c-axis, respectively, as shown in Fig. 1.8(b). SnO_2 can be found abundantly in mineral form (cassiterite) and therefore is inexpensive. As suggested by the unweathered facet surface of cassiterite shown in Fig. 1.8(c), SnO_2 is chemically stable and exhibits excellent mechanical properties. In general, such properties are favorable for PVC applications because the fabrication process is often intense, and the lifetime of PVCs should be more than 10 years in the field.

SnO_2 is the second oldest TCO material and is one of the most widely used. Sb- or F-doping are typically used to enhance conductivity. In particular, F-doped SnO_2 (FTO) grown by chemical vapor deposition (CVD) exhibits good electrical and optical properties. Large-area FTO-coated glass has been commercially available from companies such as Asahi Glass, where CVD apparatuses are built in mass-production lines of glass. Owing to its large-scale availability, FTO has been vastly used for low-emissivity glass and electrodes of thin-film silicon PVCs [2].

As discussed above, SnO_2 has various characteristics suitable for PVC electrodes, such as low cost, durability against reducing ambient, and availability on a mass-production scale. Thus, SnO_2 will be an ideal TCO for full spectrum PVCs, provided a high μ_H value is able to be attained. The potential for high μ_H in SnO_2 thin films can be directly estimated

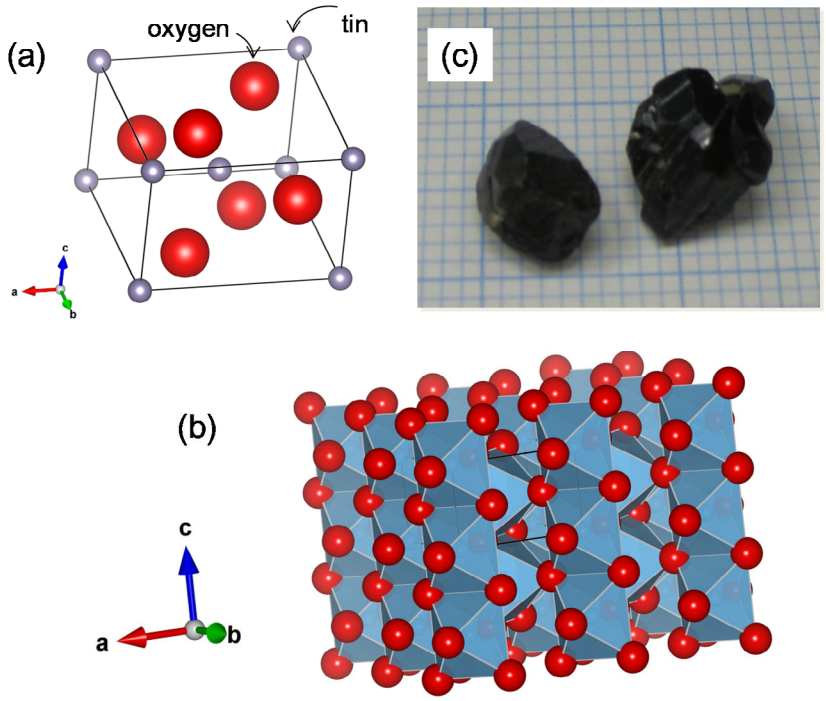

Fig. 1.8. (a) Crystal structure of SnO_2. (b) Structure of SnO_2 emphasizing edge-sharing along c-axis. (c) Photograph of mineral SnO_2 (cassiterite) from Kaneuchi mine at Kyoto.

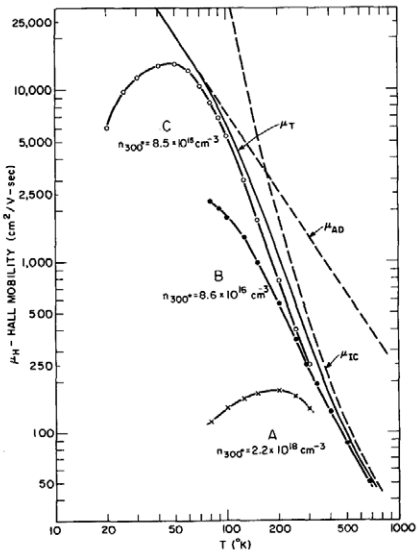

Fig. 1.9. Temperature dependence of μ_H for bulk single crystals of SnO_2 with various n_e [32] (Copyright (1970) AIP Publishing LLC).

from studies on bulk single crystals. Nearly half a century ago, several groups investigated the transport properties of SnO_2 single crystals grown by the chemical vapor transport method [32, 33]. The observed μ_H values at room temperature were in the range of 150–260 $cm^2V^{-1}s^{-1}$ [32, 34], which were dominated by phonon-scattering as shown in Fig. 1.9. Therefore, SnO_2 thin films will exhibit high μ_H values if thin films with equal quality to bulk single crystals are realized. In addition, cyclotron resonance measurements [35] on bulk single crystals provided experimentally determined m^*. Table 1.3 shows a comparison of various basic physical properties for the parent compounds of TCOs and Si [36]. It should be noted that SnO_2 has a slightly smaller m^* than In_2O_3. This suggests that SnO_2 films with sufficient quality might exhibit higher μ_H than In_2O_3 films.

Contrary to the expected high μ_H values, no study on doped SnO_2 films has reported high μ_H values exceeding 80 $cm^2V^{-1}s^{-1}$, despite a long history of available research on the material. Figure 1.10 shows a n_e-μ_H plot for typical SnO_2 thin films [6]. Although an exceptional study reported μ_H = 70 $cm^2V^{-1}s^{-1}$ for an amorphous SnO_2 thin film deposited by filtered vacuum arc deposition [37], no reproducibility for such high μ_H in amorphous SnO_2 has been confirmed (see appendix C). Typical μ_H values lie in the range of 10–40 $cm^2V^{-1}s^{-1}$, which are far less than the targeted value of 80 $cm^2V^{-1}s^{-1}$.

A hint to improve μ_H can be found in film-thickness dependence of transport properties of polycrystalline films. As shown in Fig. 1.11(a), it is widely observed that μ_H increases with an increase in film thickness, frequently involving enlarged crystalline grains [38, 39, 40]. Very recently, Isshiki et al. [40] analyzed the film-thickness dependence of the transport properties of FTO films on the basis of two-layer model, as shown in Fig. 1.11(b).

Table 1.3. Basic properties of SnO_2, In_2O_3, ZnO, and Si [36].

Properties	SnO_2	In_2O_3	ZnO	Si
Crystal structure	tetragonal, rutile	cubic, bixbyite	hexagonal, wurtzite	cubic, diamond
Average amount of the metal in the earth's crust (ppm)	40	0.1	132	2.58×10^5
Bad gap (eV)	3.6 (dir)	2.7 (indir) 3.6 (dir)	3.4 (dir)	1.12 (indir) 4.18 (dir)
Static dielectric constant	//*c*: 9.6 ⊥*c*: 13.5	9	//*c*: 8.75 ⊥*c*: 7.8	11.9
Effective electron mass m^*/m_e	//*c*: 0.23 ⊥*c*: 0.3	0.35	0.28	0.337

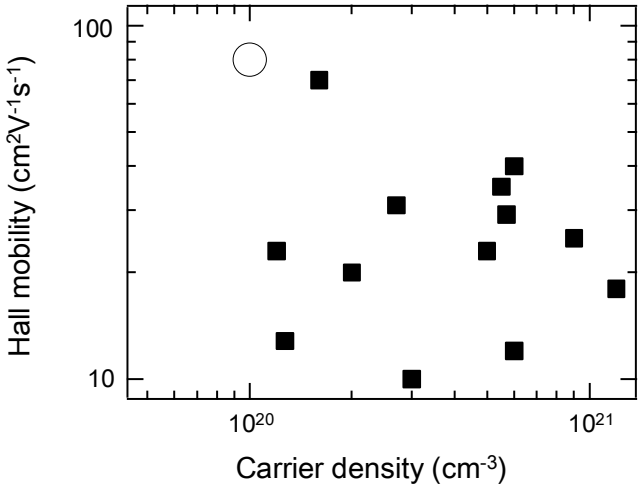

Fig. 1.10. μ_H as a function of n_e for amorphous or polycrystalline SnO_2-based TCO films thus far reported [6]. Open circle is the target value in this study.

Surprisingly, they found that the topmost layer in a 1-μm thick film with large grains is estimated to exhibit high μ_H values exceeding 90 $cm^2V^{-1}s^{-1}$, in spite of low μ_H values (~10 $cm^2V^{-1}s^{-1}$) of the initial layer. Thus, high-μ_H SnO_2 will be realized if one successfully develops a growth technique by which the quality of the topmost layer can be achieved in the initial stage of film growth.

One possible method to obtain such films is to grow films epitaxially on single crystalline substrates. Although the epitaxial films are unsuitable for practical PVCs due to limited scalability and high cost of the substrates, the transport data on the epitaxial films provide us with a significant clue to the realization of high μ_H. SnO_2 thin films can be grown epitaxially on single crystalline substrates such as corundum Al_2O_3 and rutile TiO_2 [41, 42, 43]. TiO_2 is isostructural to SnO_2, and therefore the epitaxial growth of SnO_2 films on TiO_2 substrates is, in principle, possible in any orientation [43]. A drawback of TiO_2 is large lattice-mismatch: 3.1% and 7.7% for a-axis and c-axis, respectively. In addition, the possible conductivity of TiO_2 formed in a reducing ambient during film growth might make it difficult to obtain reliable transport properties of SnO_2 thin films. On the other hand, Al_2O_3 is highly resistive and robust against a reducing ambient. Therefore, Al_2O_3 substrates are suitable for transport studies. A drawback of Al_2O_3 substrates is its complicated epitaxy, owing to the difference in crystal structure. For example, (100)-oriented SnO_2 thin films are grown on Al_2O_3 (0001) substrates with triple-domain structure.

To date, numerous studies reported epitaxial growth of SnO_2 thin films on single crystalline substrates. However, transport properties were rarely reported in those studies.

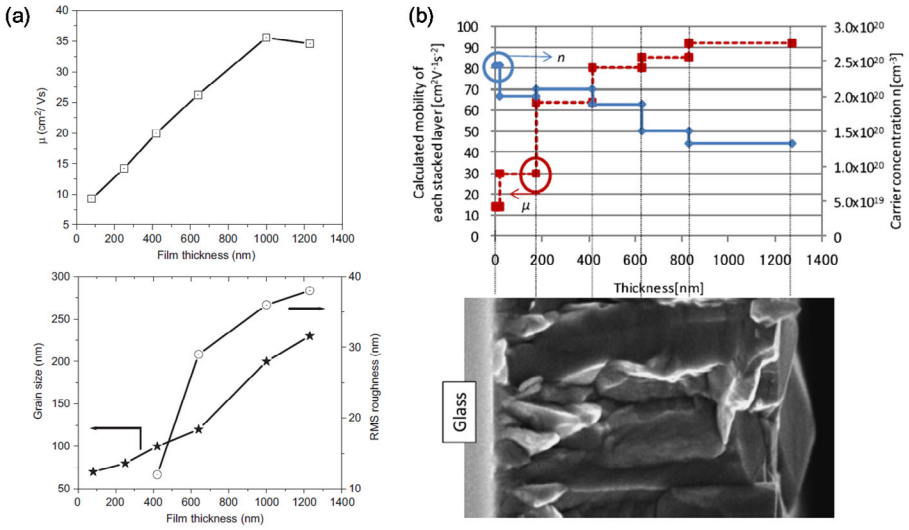

Fig. 1.11. (a) Film thickness dependence of μ_H (upper panel) and grain characteristics (lower panel) for FTO [39]. (b) Estimated transport properties of FTO based on two-layer model (upper panel) and corresponding cross sectional scanning electron microscope image (lower panel) [40] (Copyright (2009) Elsevier).

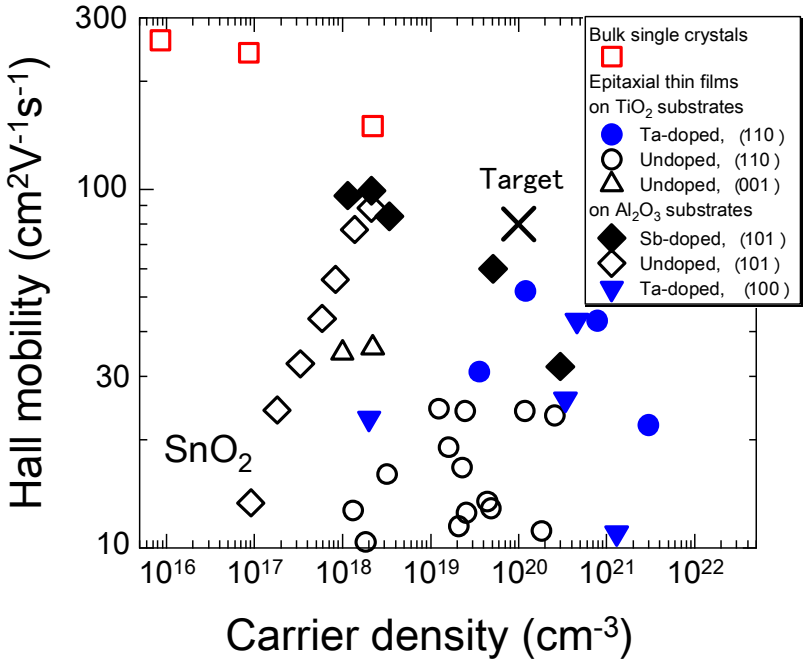

Fig. 1.12. Room temperature μ_H as a function of n_e for undoped (open symbols) and doped (closed symbols) SnO_2 bulk single crystals [32] and epitaxial films [44,45,47,48,54,55]. Cross is the target value in this study.

Okude et al. [44] grew undoped SnO_2 thin films on TiO_2 (001) substrates, which exhibit the best lattice-match among TiO_2 substrates with various orientations. The obtained μ_H at room temperature was 38 $cm^2V^{-1}s^{-1}$, which was significantly lower than those for bulk single crystalline SnO_2. Zhen et al. [45] investigated the transport properties of undoped SnO_2 thin films grown on TiO_2 (110) substrates. The substrates were characterized by a high-quality surface with a step and terrace structure, albeit a relatively large lattice-mismatch for this orientation. The maximum μ_H values for the (110) SnO_2 films was 35 $cm^2V^{-1}s^{-1}$, which was comparable with those for the (001) films. On the other hand, Tien et al. reported [46] that μ_H values for (100) SnO_2 films on Al_2O_3 (0001) substrates were less than 3 $cm^2V^{-1}s^{-1}$. This value was one order of magnitude lower than those for (110) and (001) films on TiO_2 substrates. A structural investigation on (100) SnO_2 films on Al_2O_3 (0001) substrates revealed that the in-plane structure of the films was characterized by highly populated dislocations and domains, which would be accountable for significantly reduced μ_H.

The n_e values in undoped SnO_2 thin films are somewhat uncontrollable because electrons are released from unintentional defects such as interstitial cations, anion vacancies, and dislocations. This suggests that high n_e values for undoped SnO_2 thin films are incompatible with high crystallinity [45]. Instead of undoped films, intentionally doped epitaxial films, where controlled carrier-doping is possible, are preferable in order to obtain insight into realization of high μ_H. However, studies conducted on doped epitaxial SnO_2 films thus far are even fewer in number than those conducted on undoped SnO_2 films. In 2008, Toyosaki et al. [47] investigated the dopant concentration

dependence of transport properties of Ta-doped SnO_2 (TTO) thin films on TiO_2 (110) substrates. The n_e values for the TTO epitaxial films were systematically changed from 10^{19} to 10^{21} cm^{-3} by Ta-doping. Similar systematic carrier doping was reported by Kim et al. [48] for TTO (100) films on Al_2O_3 (0001) substrates. Contrary to the naive expectation for high μ_H, even doped epitaxial films showed a rather low μ_H of 50 $cm^2V^{-1}s^{-1}$ at best [47], as shown in Fig. 1.12. Moreover, an increase in μ_H with the increase in n_e in the low n_e region in n_e-μ_H plot was observed [47, 48]. These results in combination with results obtained on undoped films suggest that grain boundary scattering plays an important role in carrier transport in epitaxial films as well as in polycrystalline films. One possible source of the grain boundary scattering is a small angle grain boundary due to island growth [44, 45, 48] and crystallographic shear plane (CSP) [49] induced by misfit dislocations [50].

Here, it is significantly insightful to review the experimental status in epitaxial films of other typical wide gap oxide semiconductors, i.e. ZnO and In_2O_3. In sharp contrast to the rather poor μ_H in SnO_2 epitaxial films, both ZnO [51] and In_2O_3 [52] epitaxial films reportedly exhibit higher μ_H values than bulk single crystals, as shown in Fig. 1.13. For example, self-buffered ZnO films grown on $ScAlMgO_4$ (0001) substrates, which show a very small lattice mismatch of 0.09% to ZnO along the a-axis, exhibited a room temperature μ_H of 440 $cm^2V^{-1}s^{-1}$. This value was significantly higher than those for bulk single crystals of ZnO, 200–209 $cm^2V^{-1}s^{-1}$. Similarly, In_2O_3 films grown on Y-stabilized ZrO_2 substrates, which show a rather small lattice mismatch of 1.6% to In_2O_3, exhibited high μ_H values that exceeded bulk values. As shown in Fig. 1.14, these high quality

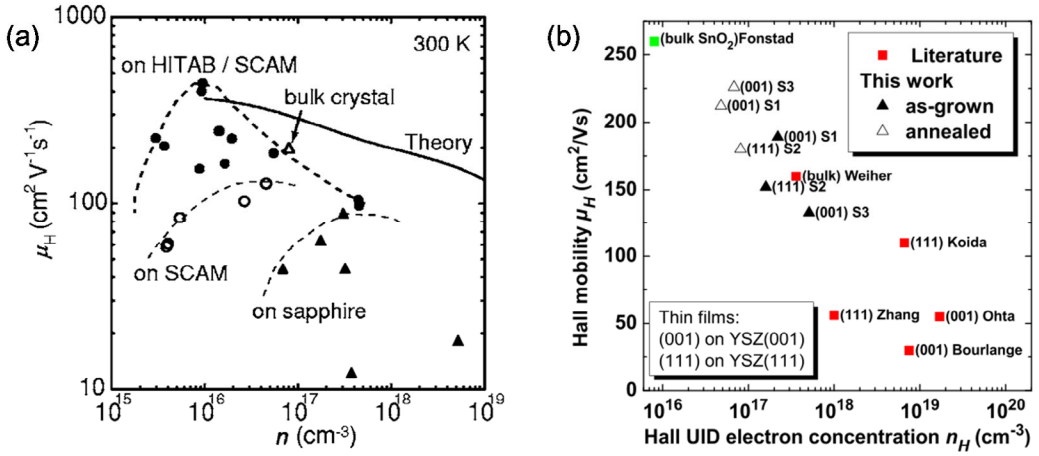

Fig. 1.13. Room temperature μ_H as a function of n_e for (a) ZnO [51] (Copyright (2006) AIP Publishing LLC) and (b) In_2O_3 [52] (Copyright (2010) AIP Publishing LLC) epitaxial films.

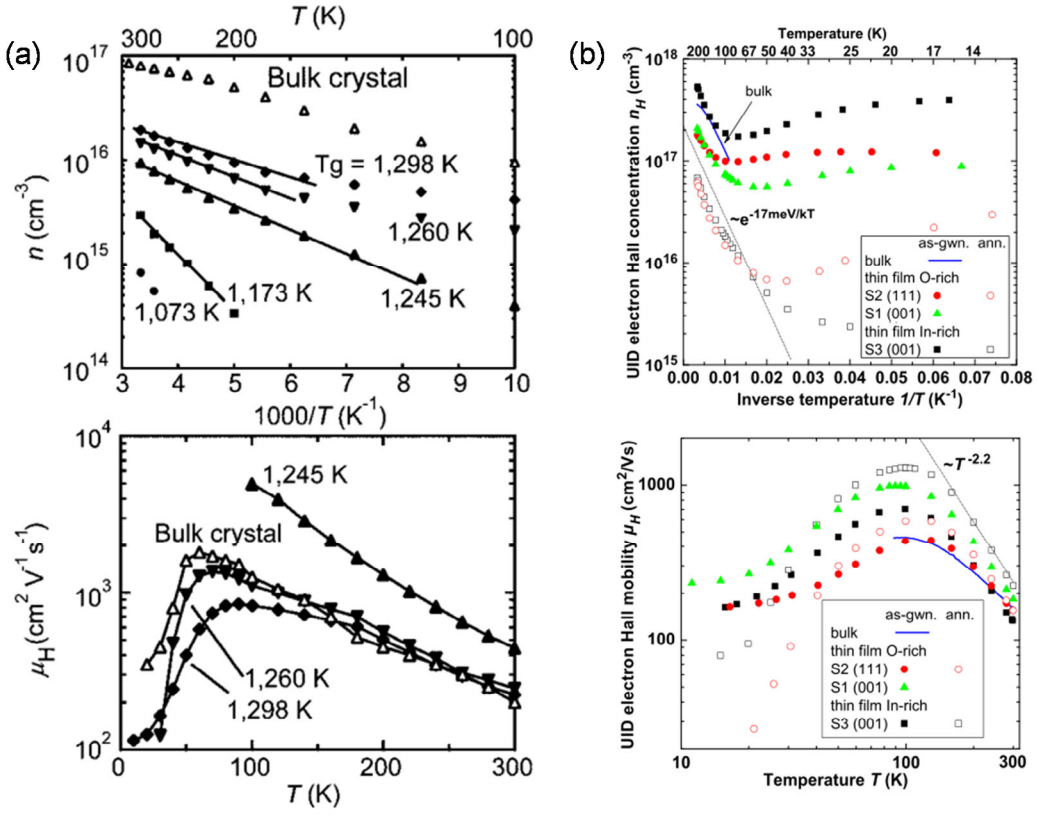

Fig. 1.14. Temperature dependence of n_e (upper panels) and μ_H (lower panels) for (a) ZnO [51] (Copyright (2006) AIP Publishing LLC) and (b) In_2O_3 [52] (Copyright (2010) AIP Publishing LLC) epitaxial films.

epitaxial films exhibited a strong negative coefficient in temperature dependence of μ_H, indicating that the dominant scattering in these films is phonon. The keys to these successes include high purity initial materials, carefully selected growth parameters, and the use of lattice matched substrates.

To overcome the unavailability of lattice-matched substrates for the epitaxial growth of SnO_2, White et al. [53, 54] used a very thick self-buffer layer. They deposited undoped and Sb-doped SnO_2 thin films on *r*-cut Al_2O_3 substrates by oxygen-plasma assisted molecular beam epitaxy. They first investigated the transport properties of undoped SnO_2 thin films as a function of film thickness. As shown in Fig. 1.15(b), μ_H and n_e rapidly increased and decreased, respectively, with the increase in film thickness. Very low n_e, as low as 3×10^{17} cm^{-3}, which was one or two orders of magnitude lower than typical undoped SnO_2 epitaxial films, was obtained. Such a low residual n_e indicates that the films were of high quality with low defects. In addition, the μ_H values of the films exceeded 100 $cm^2V^{-1}s^{-1}$ at room temperatures. The change in transport properties became gradual above a film thickness of 500 nm, where the density of dislocations was greatly reduced, as seen in Fig. 1.15(a). Therefore, they used 500-nm-thick undoped SnO_2 layers as the buffer layers for Sb-doped SnO_2 films. Surprisingly, the use of the thick self-buffer layers dramatically improved the transport properties of Sb-doped SnO_2 films, as shown in Fig. 1.15(c). First, the doping efficiency of Sb was approximately 100% in a wide doping range from 1×10^{18} to 3×10^{20} cm^{-3}. This result suggests that various defects that trap or release carriers were significantly reduced because of the lattice-matched buffer layer. Second, the increase in μ_H with the increase in n_e in the low n_e region was not observed

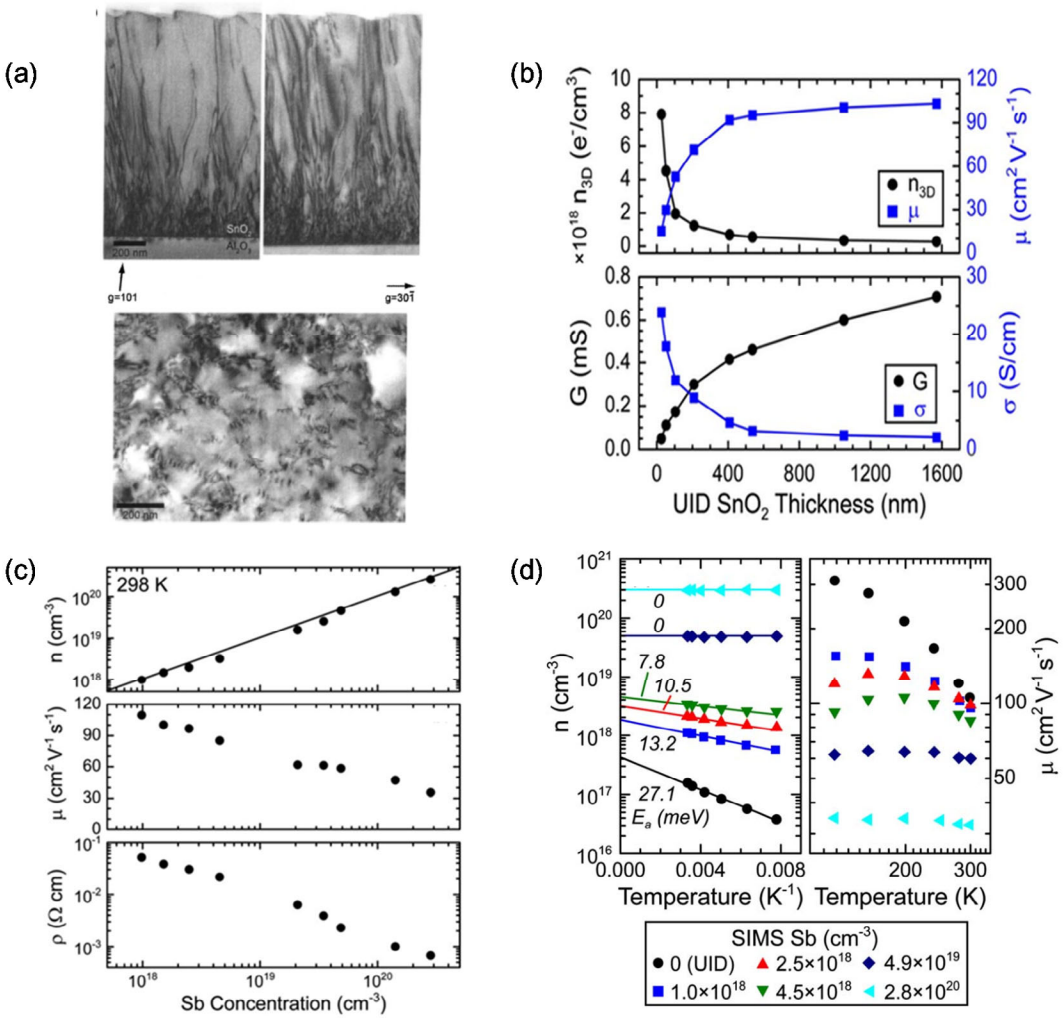

Fig. 1.15. (a) Cross sectional (upper panels) and plane view (lower panel) TEM images for a SnO_2 film grown on r-cut Al_2O_3 [53] (Copyright (2008) AIP Publishing LLC). (b) Film thickness dependence of room temperature transport properties of SnO_2 films grown on r-cut Al_2O_3. (c) Sb concentration dependence of room temperature transport properties of Sb-doped SnO_2 films grown on 500 nm-thick self-buffer layers. (d) Temperature dependence of the transport properties of the Sb-doped SnO_2 films grown on 500 nm-thick self-buffer layers. [54] (Copyright (2009) AIP Publishing LLC).

probably for the first time in SnO_2 thin films. Third, the negative coefficient in the temperature dependence of μ_H was observed as shown in Fig. 1.15(d), indicating that phonon scattering is the dominant factor of μ_H. Such behavior was observed only for bulk SnO_2 single crystals (Fig. 1.9) and extremely high-quality thin films of ZnO and In_2O_3 (Fig. 1.14). These features clearly demonstrate that lattice-matched epitaxial growth paves the way for high-μ_H SnO_2-based TCOs. A recent study has reinforced the importance of the self-buffer layer in the epitaxial growth of SnO_2 [55]. However, it should be noted that the obtained μ_H values, 50–60 $cm^2V^{-1}s^{-1}$ around 1×10^{20} cm^{-3}, were still lower than the target value of the present study, 80 $cm^2V^{-1}s^{-1}$ at 1×10^{20} cm^{-3}, as seen in Fig. 1.12. In addition, the deposition method and the substrates used in their study lack the scalability crucial for use in PVCs. Therefore, high-μ_H SnO_2-based TCOs on practical substrates by a deposition method scalable to industrial use still remain to be developed.

1.5 Strategy of This Study: Finding a Breakthrough with Pulsed Laser Deposition

Figure 1.16 shows the historical trend in reported ρ values for typical TCOs, namely ZnO, SnO_2, and In_2O_3 [18, 56]. The decrease in ρ for SnO_2 stopped in the 1980s, implying that the transport properties of SnO_2 thin films have been completely investigated. Therefore, it appears that there is no room for improvement. A novel method is necessary to enhance our understanding of the transport properties of SnO_2 thin films.

In this study, I have adopted pulsed laser deposition (PLD) to identify high μ_H values in SnO_2. Several advantages of PLD [57] enable us to explore high-μ_H SnO_2 efficiently. First, the available range of deposition parameters in PLD is much wider than those of other techniques, such as sputtering and CVD. For example, very high substrate temperatures (over 1000 °C) have been frequently used in PLD. The growth atmosphere of PLD can be systematically changed from a highly reductive atmosphere (ultra-high vacuum) to an oxidative one. An ultra-high vacuum is usually incompatible with sputtering due to the presence of electric power and cooling water lines. In addition, PLD exhibits much better controllability of the deposition parameters than sputtering; the oxidative condition in sputtering changes very rapidly from metallic to oxide mode and the actual substrate temperature during sputtering is sometimes difficult to be defined due to unintentional substrate heating. In particular, the control of the oxidative condition during deposition is very important because it determines film growth and defect formation in TCOs. Second, various materials and compositions can be explored more easily with PLD than with other techniques. Homemade sintered ceramic pellets and metal pieces can be used as targets for PLD. The use of these materials is in sharp contrast to the commercial ceramic disc and special reagent that are respectively required for sputtering and CVD. In addition, it is generally believed that PLD exhibits a stoichiometric transfer of materials from targets to films, whereas the elemental dependence of sputtering yield occasionally results in compositional deviation of sputtered film from that of the target. These features make it possible to explore various dopants and seed layers efficiently by using PLD. Third, so-called combinatorial techniques such as temperature gradient and compositional spread

can be used for exploration with high throughput. I expected that exploration for high μ_H values using PLD would end the 30-year stagnation period.

It should be noted that PLD shares two important characteristics with sputtering, both of which critically determine film properties. One is the energy of deposition particles, which is in the range of 1–10 eV [57], and the other is growth mode. Both PLD and sputtering are physical vapor deposition (PVD) techniques. Non-equilibrium growth via an energetically unstable vapor phase leads to the formation of defects, a metastable phase, and the extension of the solubility limit of dopant. In particular, Sn is favorably in Sn^{2+} (SnO) in the vapor phase [45, 58] and therefore oxygen vacancies, which are difficult to form in bulk SnO_2, tend to form in SnO_2 films by PVD. Owing to the similarity in film growth between PLD and sputtering, the knowledge obtained in PLD studies can be frequently transferred to sputtering. For example, the practical fabrication method for Nb-doped TiO_2 [59] TCO films (solid phase crystallization) was first found in a PLD study [60] and was then demonstrated in a sputtering study [61]. Even large-area coating [62] and high rate deposition [63] were successfully achieved in sputtered Nb:TiO_2, resulting in their application to electrodes in organic polymer PVCs [64]. As shown in Fig. 1.17, I witnessed and partly contributed to this dramatic development in Nb:TiO_2 fabrication [60, 64, 65, 66, 67, 68]. The difference of sputtering from PLD includes additional bombardments of high energy particles (recoiled Ar and negatively charged oxygen ions) and cosine-like angle of deposition particles. These are, however, insignificant in comparison with the large difference between highly non-equilibrium growth in PVD and nearly equilibrium growth in CVD.

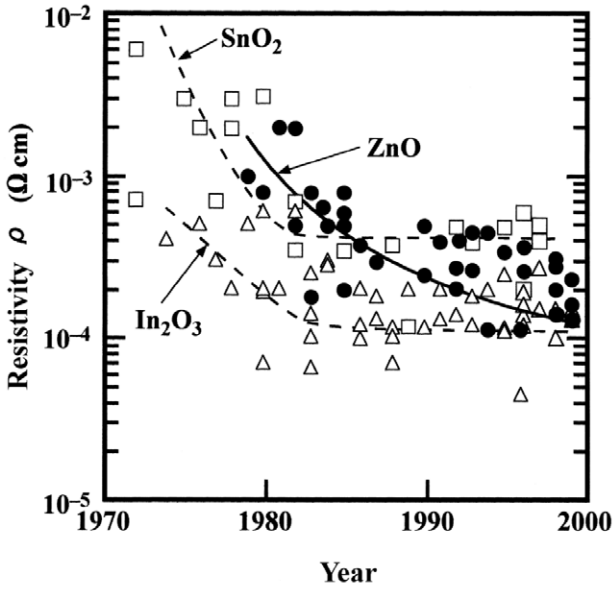

Fig. 1.16. Reported ρ values for ZnO, In_2O_3, and SnO_2 [18] (Copyright (2000) Cambridge University Press).

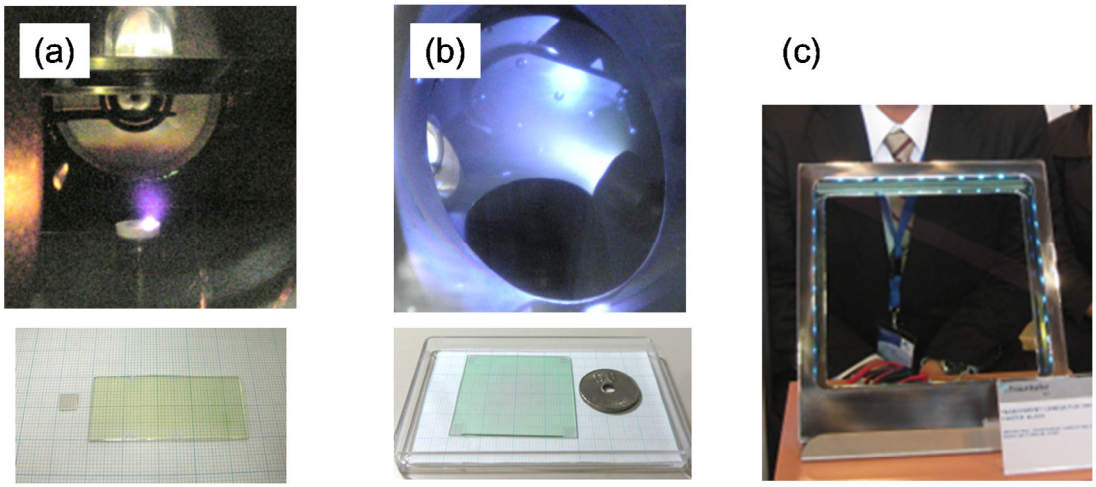

Fig. 1.17. Photographs demonstrating an essential role of PLD in development of Nb:TiO_2 TCO films. (a) Photograph of PLD deposition (upper photo). Nb:TiO_2 were first discovered in a PLD study [59] of epitaxial films. More importantly, practical fabrication method (solid phase crystallization) was found as well in a PLD study [60]. The deposition is from point source and thus the resultant films (left in lower photo) were typically 5 × 5 mm^2, which is much smaller than sputtered films (right in lower photo). (b) The material and the method found in PLD were successfully transferred to sputtering [61] where deposition is plane source (upper photo) and the result film was as large as 4 × 4 cm^2 (lower photo). (c) a 30 × 30 cm^2 Nb:TiO_2 film deposited by pulsed DC sputtering [62].

For the use of PVCs, in which large area TCOs are indispensable, the potential compatibility of PLD with sputtering is very important because PLD is unsuitable for large area coating due to limited scalability. I believe that the findings obtained in this study will be eventually transferred to sputtering, paving the road for industrial fabrication of high μ_H SnO_2 for full spectrum PVCs.

1.6 Aim of This Study

In this study, I aimed to make clear the guiding principle of materials design for high-μ_H SnO_2 thin films suitable for full spectrum PVCs. The SnO_2 thin films should transmit not only visible light, but also NIR light up to 1400 nm with sufficiently low R_s values. For large scale applications and mass production, the SnO_2 films must be grown on glass substrates. A milestone value was set for μ_H at 80 $cm^2V^{-1}s^{-1}$.

1.7 Outline of This Study

This study is organized as follows. In chapter 2, experimental procedures such as film growth and characterization are presented. In chapter 3, the structural and transport properties of SnO_2 epitaxial films are compared with those of SnO_2 polycrystalline films, demonstrating that epitaxial growth increases the μ_H value of SnO_2. In chapter 4, epitaxial

growth using a seed-layer on glass is proposed for improving μ_H, and is demonstrated by using rutile TiO_2 and NbO_2 seed layers. In chapter 5, the first instance of μ_H exceeding 80 $cm^2V^{-1}s^{-1}$ in doped SnO_2 films is reported by using a seed layer of anatase TiO_2, which is not isostructural to SnO_2. A detailed investigation of growth parameter dependence on the films is presented in chapter 6. In chapter 7, exploration of various dopants for improving μ_H is summarized. In chapter 8, a rutile $(Ti,Nb)O_2$ solid solution seed layer is finally proposed and demonstrated, resulting in an extremely high μ_H value that exceeds 130 $cm^2V^{-1}s^{-1}$. In chapter 9, a summary of this study is presented and future prospects are discussed.

Chapter 2 Experimental Procedure

The experimental procedure is presented in this chapter. Film growth in particular is described in detail because important factors for reliable and reproducible results may not be well known. On the other hand, the characterization of the films is briefly documented because the methods used in this study are rather basic, and there is a sufficient amount of information currently available in the literature [6].

2.1 Film Growth

In this study, a commercially available PLD system (Pascal, PAC-LMBE) equipped with a KrF excimer laser (LAMBDA PHYSIK, COMPex 102) was used to grow thin films. The wavelength of the laser (248 nm) was sufficiently short to deposit not only SnO_2, but also various materials including oxides and metals. The only one material that I failed to deposit was MgF_2 with a bandgap of 11.8 eV.

Figure 2.1(a) shows the actual outlook of the PLD system used in this study. The PLD system consisted of two vacuum chambers: the growth chamber and the load-lock chamber. The growth chamber was evacuated by a turbo molecular pump with a pumping speed of 800 l/s. The base pressure in the growth chamber after baking was approximately 2×10^{-9} Torr. Typical base pressure before film growth in this study was approximately 5×10^{-9} Torr due to routine deposition with high process pressure up to 1×10^{-1} Torr.

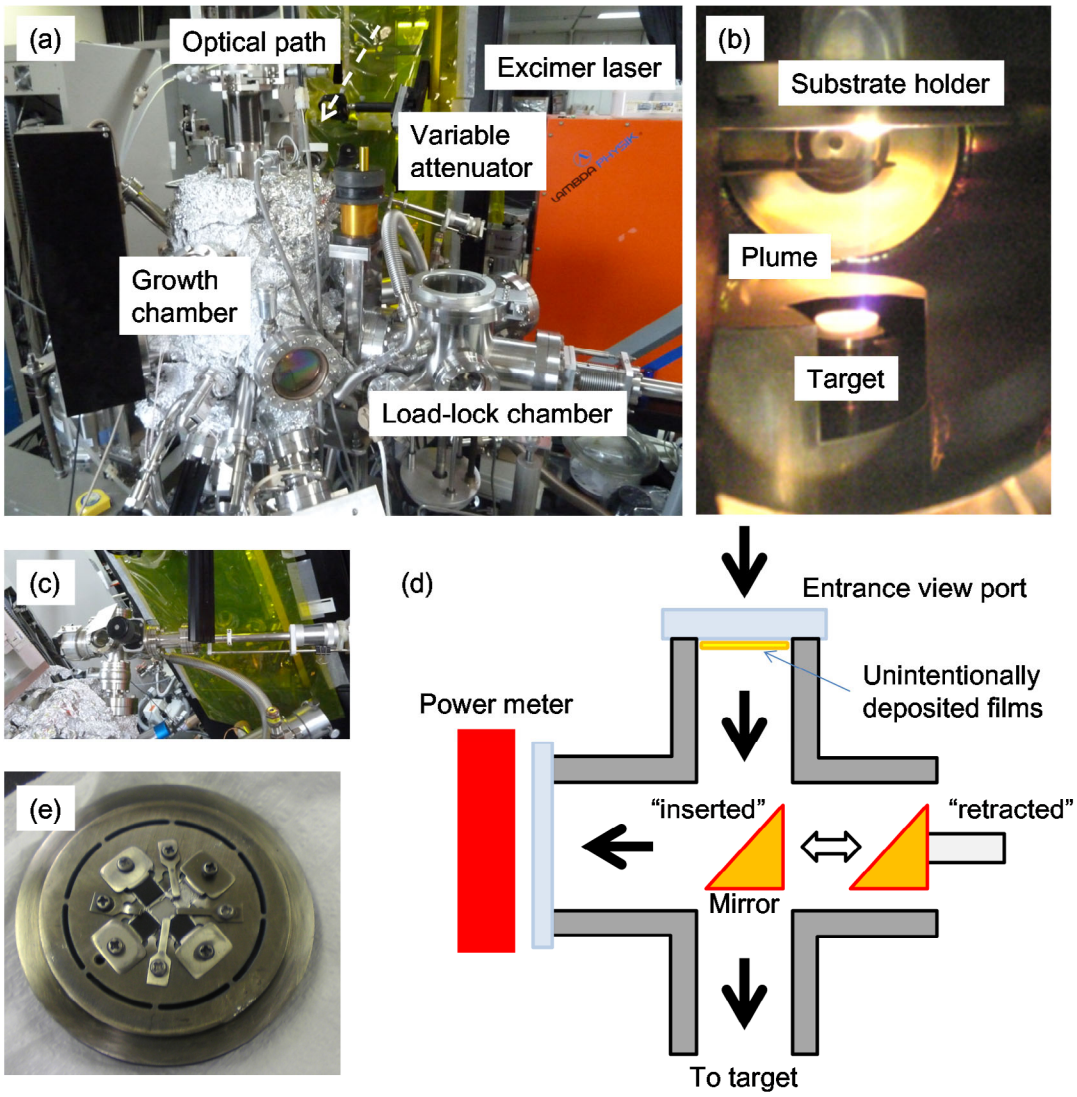

Fig. 2.1. (a) Photograph of outlook of PLD used in this study. (b) Photograph of the inside of growth chamber during deposition. (c) Photograph of "laser power monitor" option. (d) Schematic drawing of "laser power monitor" option. Laser is irradiated to targets if the mirror is retracted. During deposition, view port for power meter and the mirror are protected by shutters (not shown) from film deposition. On the other hand, laser is irradiated to the power meter if the mirror is inserted. Laser power measured by this option is free from loss due to unintentionally deposited films at the entrance view port. (e) Photograph of a substrate holder with four substrates mounted. Pt paste is painted at the center of the holder to measure temperature of the substrate holder by a pyrometer.

The base pressure was measured with an ion (Bayard–Alpert hot-cathode ionization) gauge, whereas the process pressure was measured with a capacitance diaphragm gauge. As process gas, high-purity oxygen (99.999%) was introduced into the growth chamber by using a variable leak valve.

The substrate can be heated up to 800 °C by a halogen lamp. The substrate holders were made of Inconel 600. The substrate holders were initially heated to 900 °C in an ambient atmosphere to form oxidized layers, which efficiently absorbed the light of the halogen lamp. Substrate temperature is a crucial parameter that determines film-quality, although precise determination of the substrate temperature is sometimes difficult. In this study, the temperature of the holders was measured with a pyrometer and has been defined as “substrate temperature”. The substrates were thermally contacted with the substrate holders by silver pastes. Without the silver pastes, actual substrate temperature was > 100 °C lower than that of the substrate holder, whereas the discrepancy was less than 30 °C when using thermal contact with silver paste. The substrate holders were rotated during film growth in order to obtain a homogeneous film thickness and composition. The distance between the substrate holder and the target in this study was fixed at 50 mm. A photograph taken during deposition is shown in Fig. 2.1(b)

Precise control of the laser condition is indispensable in a systematic and reproducible study using PLD. Ohnishi et al. [69, 70, 71] pointed out that various parameters of the laser condition significantly affected film properties by using a specially designed PLD, as shown in Fig. 2.2(a). Most importantly, they pointed out that the actual laser power irradiated to targets is much less than the nominal power monitored outside the PLD chamber, and the power shows a continuous decrease as the deposition run number

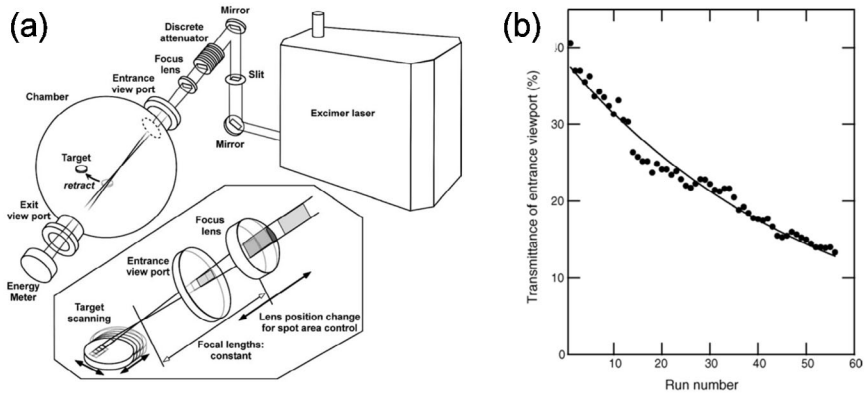

Fig. 2.2. (a) Schematic drawing of PLD designed for in-situ measurement of laser power. (b) Transmittance of laser energy through the entrance view port of the vacuum chamber plotted as a function of deposition run number [69] (Copyright (2006) Elsevier).

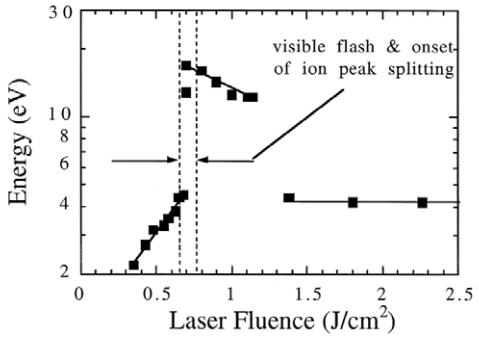

Fig. 2.3. Kinetic energy of Zn+ ion from ZnO target as a function of laser fluence [72] (Copyright (1998) Elsevier).

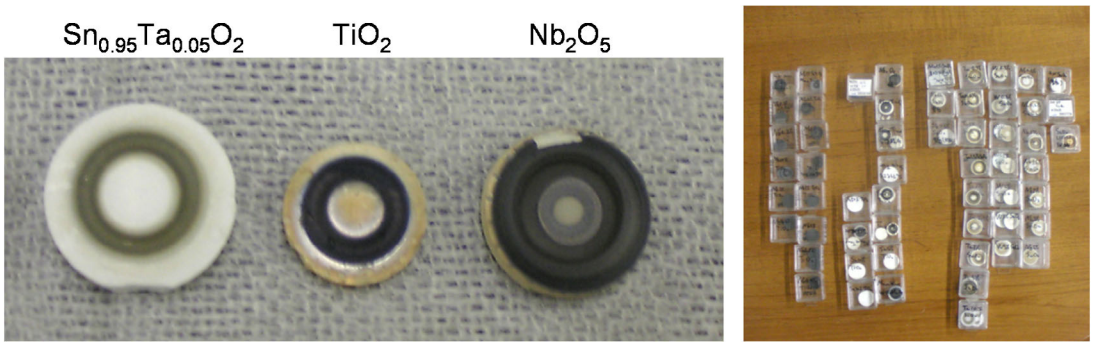

Fig. 2.4. Photographs of typical homemade targets used in this study.

increases. This is because unintentionally deposited films on the entrance view port reduce laser power, as shown in Fig 2.2(b). Laser power and laser fluence are critical parameters that determine the threshold for deposition, the deposition rate, the energy of the deposition particles, and the composition of the plume (i.e., atom and ion species), as shown in Fig. 2.3 [72]. These characteristics significantly affect film growth. Therefore, keeping laser power and laser fluence constant is critically important in order to obtain films in a systematic and reproducible manner.

Furthermore, Ohnishi et al. pointed out that the operating voltage of an excimer laser affects the energy profile of the beam, claiming that operating voltage should be fixed. In this study, the "laser power monitor" option (Fig. 2.1(c) and (d)), which was implemented by Prof. Hirose, has been attached to PLD. Furthermore, a variable attenuator was installed in the optical path (Fig. 2.1(a)) to adjust laser power without changing the operating voltage. Thanks to these apparatuses, I set the laser power and operating voltage at 20 mJ and 27.5 kV, respectively. The lens of the optical path was adjusted to yield the smallest spot area on the target. The laser fluence was 1–2 Jcm^{-2} due to the uncertainty associated with determining the spot area. The repetition rate of the laser was in the range of 2–5 Hz.

The quality of the targets is an important factor determining quality and reproducibility of the films. For example, targets with a low sintered density occasionally yield unstable deposition in sputtering (arcing) and the formation of particles in PLD. Thus, special care should be taken to prepare targets. Using a commercial target is preferable because very high sintered density is often realized by a state-of-the-art method, such as hot isostatic pressing. For example, commercial ITO targets exhibit 99% sintered density,

which is among the key technologies that make ITO a practical material. However, homemade targets were mainly used in this study because exploratory studies inevitably require many targets. I created targets using the solid state reaction method. Photographs of typical targets are shown in Fig. 2.4. The starting powders were grinded and mixed by an agate mortar. The powders were pressed into pellets and then sintered for 12 h in air at 1150 °C and 1350 °C for SnO_2 and $(Ti,Nb)O_2$, respectively. Because SnO_2 is well-known for being difficult to densify, special care was taken. SnO_2 powder with 99.9% purity (Sigma-Aldrich, 244651) was found to be suitable for PLD targets; however, the sintered density of the SnO_2 targets made from the powder was low (approximately 55%). The surface of the targets after laser irradiation was smooth, similar to single crystalline targets. Consequently, particle-free films were obtained from the target. On the other hand, 99.99% pure SnO_2 powder (Nilaco, SN-447100) yielded targets with lower sintered density. Such targets collapsed after laser irradiation; films from the targets were characterized by many particles and were not used in this study. The 99.9% purity SnO_2 powder contained an Sb impurity of 0.01–0.02%, which might be the source of n_e in the nominally undoped SnO_2 films obtained in this study. Prior to deposition, the surface of the targets were cleaned by laser irradiation, which is called “pre-ablation”, for 10 min at base pressure.

The substrate used in this study was alkaline-free glass (Corning 1737 or corning Eagle XG). The strain point for the glass is approximately 670 °C, and thus we restrained substrate temperature to a maximum of 600 °C. For comparison, Al_2O_3 (0001) single crystalline substrate was used in chapter 3. The Al_2O_3 substrates were annealed in air at 1000 °C for 3 h to obtain step and terrace surface. As shown in Fig. 2.1(e), four different substrates can be mounted on one substrate holder at a time. All of these substrates were cut

into 5 × 5 mm^2 pieces and were then ultrasonically cleaned in acetone, followed by ethanol-rinsing and N_2-drying. Metal Ti shadow masks were employed to fabricate Hall-bar shape films for transport measurements.

2.2 Characterization

Film thickness was measured with a stylus profiler (Veeco, Dektak 6M). At least six points per a sample were measured and the averaged value was defined as the film thickness. Due to a thickness gradient caused by the point-source nature of PLD, a 10% maximum deviation in thickness for a film, which determined the accuracy of the ρ and n_e values, was observed. However, R_s and μ_H, which are more important than ρ and n_e in this study, are more accurate because film thickness is not included or cancelled out in evaluation of these values. In this study, error bars were typically within the size of the symbols.

The crystal structures of the films were evaluated using X-ray diffraction (XRD). This was achieved by using a four-circle diffractometer equipped with a two-dimensional area detector (Bruker AXS, D8 Discover with GADDS). The surface morphology of the films was measured with an atomic force microscope (AFM, Seiko Instruments, SPI-4000) with a cantilever tip with a curvature radius of 20 nm. The microstructures of the films were observed by cross-sectional transmission electron microscopy (TEM). The texture structures of the films were characterized using a polarized light microscope with nearly crossed polarizers.

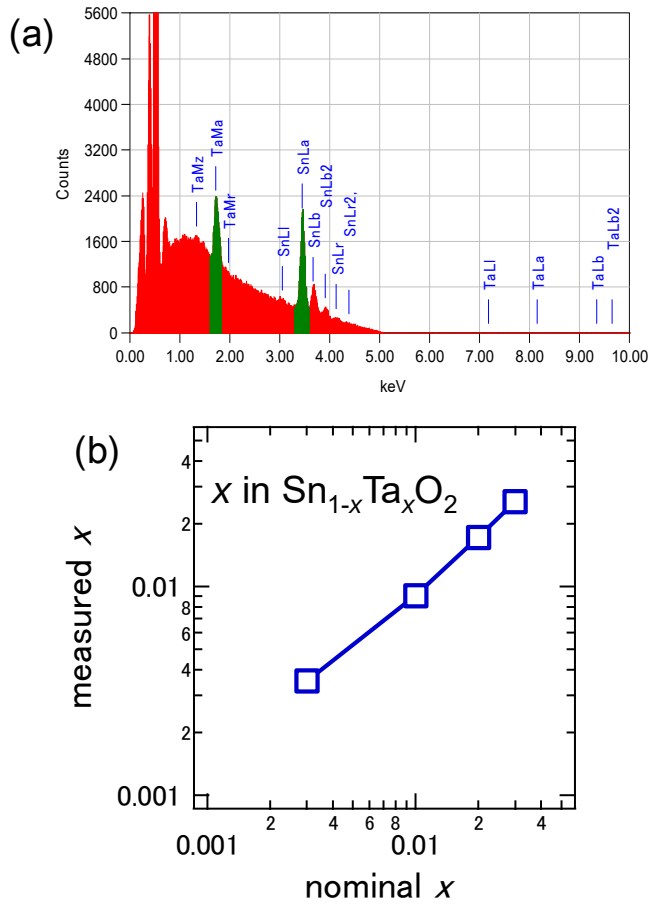

Fig. 2.5. (a) Typical energy dispersive X-ray spectra for an amorphous $Sn_{0.97}Ta_{0.03}O_2$ film. Acceleration voltage was set to 5 kV to minimize signals from substrates. (b) Relation between nominal ($Sn_{1-x}Ta_xO_2$ targets) composition and measured composition of films.

The transport properties of the films (ρ, n_e, and μ_H) were measured using a four-probe ρ measurement and Hall measurement in typical six-probe Hall-bar geometries. The Hall-bar width and the distance between voltage terminals for four-probe measurements were 1 mm and 2.4 mm, respectively. For comparison, the transport properties of a few 5×5 mm^2 square films were measured with the van der Pauw method, resulting in essentially the same results. Ohmic electrodes were prepared by mechanically pressing In pieces onto the film surface. The In electrodes showed good ohmic contact with low contact resistance and are thus sufficient for room temperature measurements. For temperature dependence measurements, Ag electrodes deposited by vacuum evaporation or sputtering were used. A laboratory constructed system equipped with a two tesla electromagnet was used for room temperature measurements. Applied current was generated by a Keithley 2410 SourceMeter or 6487 Picoammeter, whereas voltage was measured with Keithley 2000 or Agilent 34401 multimeters. Current–voltage characteristics and Hall voltage-magnetic field characteristics were measured repeatedly (at least twice) to confirm the reliability and reproducibility of the measurements. The temperature dependence of the transport properties were measured with a commercially available system (Quantum design, physical properties measurement system (PPMS Model 6000)) equipped with a nine tesla superconducting magnet. The two independent systems for transport measurement yielded consistent results with each other, with a few % discrepancies.

The optical transmittance spectra at normal incidence and reflectance spectra at near-normal incidence (5 °) in a wavelength range of 250–2500 nm were measured at room

temperature using an ultraviolet-visible-NIR spectrophotometer (JASCO, V-670). The optical properties in the NIR region were also measured with Fourier transform infrared spectrometers (JASCO, FT/IR-6100) to obtain a better S/N ratio. The absorption spectra were calculated as the difference between unity and the sum of the reflectance and transmittance spectra. The reference for the optical measurement was the air, and thus loss due to glass substrates was not extracted in the data.

Compositional analysis was performed on amorphous Ta-doped SnO_2 films used in appendix C by using an energy dispersive X-ray analyzer (JEOL, JED-2300) equipped with a scanning electron microscope (JEOL, JSM-7001F). As shown in Fig. 2.5, the analyzed compositions were consistent with the nominal values, demonstrating generally believed stoichiometric transfer in PLD. Thus, the nominal compositions of targets were used to represent the chemical compositions of films throughout this study.

Chapter 3 Comparison of Transport Properties between Polycrystalline and Epitaxial Ta-doped SnO_2 Films*

In this chapter, I compared the XRD patterns and transport properties of TTO epitaxial films on Al_2O_3 (0001) and polycrystalline films on glass grown in the same deposition run. The crystal structure of epitaxial films was almost independent of Ta content, while the preferred growth plane of the polycrystalline films was significantly influenced by Ta doping. The polycrystalline films exhibited approximately three times higher ρ values than the epitaxial films, mainly due to reduced μ_H. This result clearly demonstrates that epitaxial growth is useful for enhancing μ_H in SnO_2 films.

3.1 Introduction

As reviewed in chapter 1, transport properties of polycrystalline and epitaxial SnO_2 thin films have been investigated by various deposition methods. To my knowledge, however, no comparative study on polycrystalline and epitaxial films has been reported. Therefore, it was unclear how epitaxial growth affected transport properties of SnO_2. In this

* A version of this chapter has been published in Thin Solid Films 518, 3093 (2000).

study, I grew both polycrystalline and epitaxial SnO_2 films in the same deposition run and compared their structure and transport properties.

In this study, Ta was employed as a dopant for carrier doping for a few reasons. First, very high doping efficiency approaching 100%, which was not confirmed in Sb-doped SnO_2 [73] and FTO [74] by PLD, has been reported for TTO films [47]. This indicates that TTO films are unlikely to contain inactive dopant (Ta^{4+}) acting as neutral impurity and unfavorable defects such as clustered dopants and accepter-like defects. Second, Sb and F might be re-evaporated during high temperature deposition whereas Ta is nonvolatile. Third, possible toxicity of Sb might regulate future large scale use of Sb-doped SnO_2. For this reason, a number of studies [47, 48, 75, 76, 77, 78, 79, 80, 81] including this study investigated TTO films for this decade.

3.2 Film Growth

$Sn_{1-x}Ta_xO_2$ (TTO) thin films with x = 0~0.1 were fabricated on alkaline-free glass (Corning 1737) and Al_2O_3 (0001) single-crystalline substrates by PLD. Sintered pellets composed of SnO_2 and Ta_2O_5 were used as PLD targets. The substrate temperature and the oxygen partial pressure during deposition were set to 600 °C and 3×10^{-3} Torr, respectively. Repetition rate of the laser for deposition was 2 Hz. The films were 110 ± 20 nm thick.

3.3 Results and Discussion

Figures 3.1(a) and (b) show the XRD patterns of TTO films grown on Al_2O_3 (0001) and glass substrates, respectively. As seen from the figures, the TTO films on glass were in the polycrystalline state without preferential orientation, whereas the epitaxial films on Al_2O_3 (0001) were *a*-oriented [41, 42, 46, 48]. No impurity phase such as $SnTa_4O_{11}$, $SnTa_2O_6$, and Ta_2O_5 could be detected up to $x = 0.1$ for both the polycrystalline and the epitaxial films. In the epitaxial films, the rocking curve of the 200 diffraction exhibited a full width at half maximum of ~0.08 °, irrespective of x. Furthermore, the intensities of the 200 and 400 diffractions are essentially constant with respect to x. Thus, it is concluded that an excellent crystallinity is maintained up to $x = 0.1$ in the epitaxial films. On the other hand, polycrystalline films on glass exhibit a rather complex structural behavior. The XRD pattern of the undoped film ($x = 0$) is similar to that of bulk SnO_2 (JCPDS 41-1445). With increasing x, the intensity of the 200 diffraction is monotonically suppressed, whereas a peak assigned to 101 abruptly evolves. Other diffraction peaks, such as those for 110 and 211, exhibit maximum intensities at $x = 0.01$–0.05. These imply that the preferred growth plane of the TTO polycrystalline films varies depending on the Ta content. Such a phenomenon was also reported in cases where SnO_2 was doped with other elements, such as Sb [82] and F [83]. It has not yet been clarified why the dopant concentration affects the preferred growth. I speculate that, similar to oxygen partial pressure dependence [84], dopant elements could affect the stability of the low index surfaces and thus the nucleation.

Figure 3.2 shows typical AFM images for the polycrystalline and epitaxial TTO films. As shown in Fig. 3.2(a), surface morphology of the polycrystalline film was

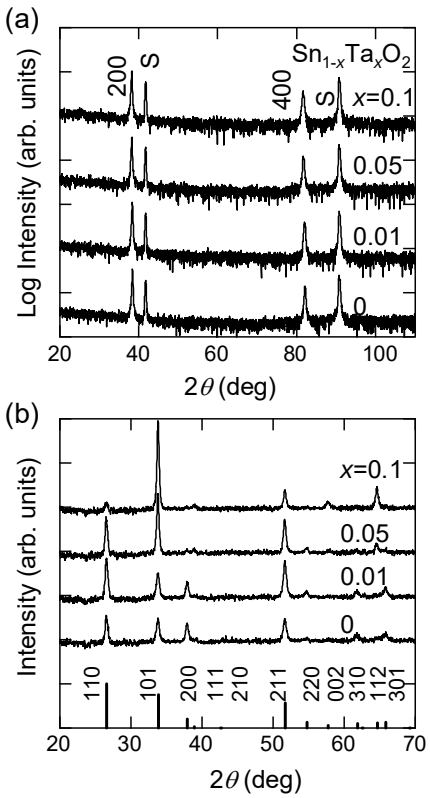

Fig. 3.1. XRD patterns of TTO thin films on (a) Al_2O_3 (0001) and (b) glass substrates. Bar graph shows the XRD pattern of bulk SnO_2 (JCPDS 41-1445). S denotes substrate peaks.

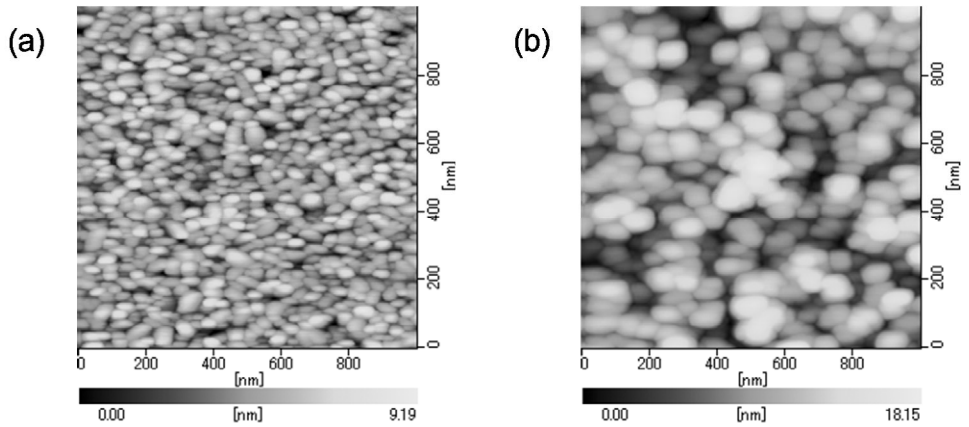

Fig. 3.2. AFM images of $Sn_{0.95}Ta_{0.05}O_2$ films grown on (a) glass and (b) Al_2O_3 (0001) substrates.

characterized by fine grains. Grain structure was observed for the epitaxial film (Fig. 3.2(b)) as well although the film was grown on a single crystalline substrate with step and terrace structure. This is probably because SnO_2 tends to grow in Volmer-Weber mode [44, 45]. Triple domain structure [46, 48] might well contribute to grain formation.

Finally, I discuss transport properties. Fig. 3.3 shows a comparison between the transport properties of the polycrystalline and epitaxial TTO films. The epitaxial films exhibited 2.4×10^{-4} Ωcm at $x = 0.025$~0.03, which is comparable with the previously reported values for CVD films on Al_2O_3 (0001) (3.1×10^{-4} Ωcm) [48] and PLD films on TiO_2 (110) (1.1×10^{-4} Ωcm) [47], as shown in Fig. 3.3(e). On the other hand, the polycrystalline TTO films showed approximately three times higher ρ values of 7×10^{-4} Ωcm at $x = 0.015$~0.03. As shown in Fig. 3.3(b), both polycrystalline and epitaxial films showed systematic increase in n_e as Ta-doping concentration increased. In particular, very high doping efficiency approaching 100% was achieved for the epitaxial films at $x < 0.01$. Maximum n_e values for the polycrystalline and epitaxial films were 5.2×10^{20} cm^{-3} and 7.6×10^{20} cm^{-3}, respectively. The difference in n_e might be attributable to the difference in crystallinity of the films. As shown in Fig. 3.3(c), μ_H values for the epitaxial films were two times higher than those for the polycrystalline films at $x \geq 0.02$, resulting in the large difference in ρ values. The highest μ_H for the epitaxial films was 53.2 $cm^2V^{-1}s^{-1}$ obtained at $x = 0.015$ whereas the highest μ_H for the polycrystalline films was 35.5 $cm^2V^{-1}s^{-1}$ obtained at $x = 0$. The enhanced μ_H values for the epitaxial films are probably owing to absence of high angle grain boundary. This result clearly demonstrates that epitaxial growth is useful for enhancing μ_H in SnO_2 films. It should be noted, however, that μ_H value

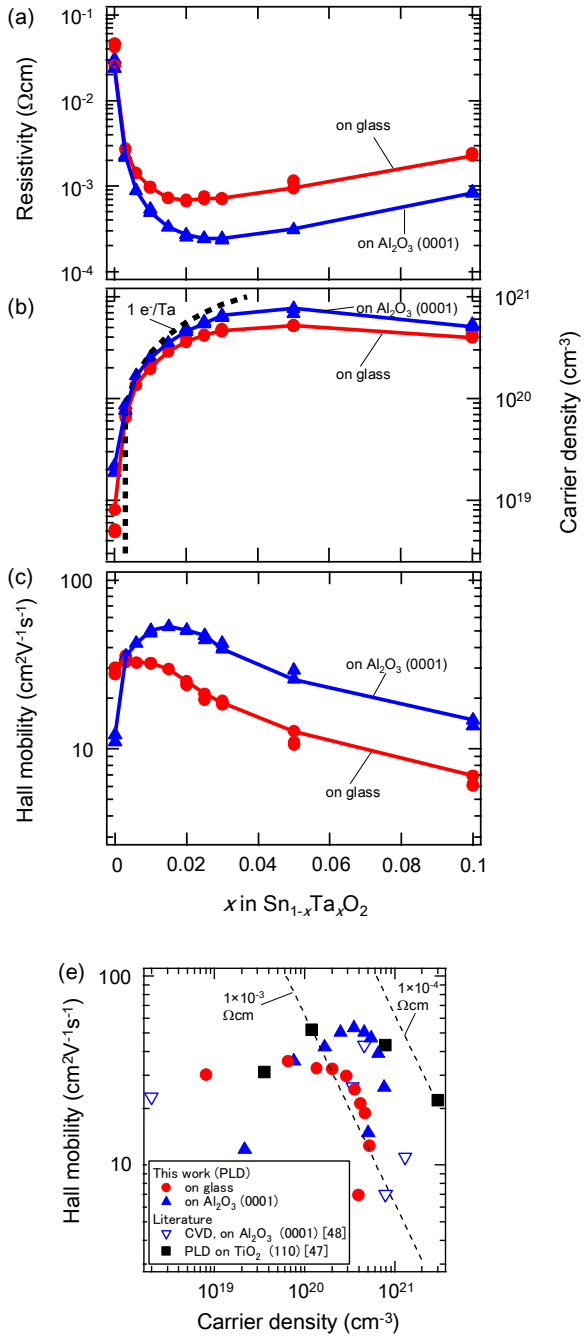

Fig. 3.3. Room temperature (a) ρ, (b) n_e, and (c) μ_H of TTO films on glass (circles) and Al_2O_3 (00101) (squares) as a function of Ta content, x, in $Sn_{1-x}Ta_xO_2$. The solid lines are guides to eyes. The dashed line in (b) is the expected carrier density assuming that all the doped Ta^{5+} ions substitute Sn^{4+} sites and generate one electron per Ta. (e) Comparison of the transport properties in this work with those for TTO epitaxial films thus far reported [47,48].

for the epitaxial films decrease as x decreased and was finally lower than that for the polycrystalline film at $x = 0$. Decreasing tendency in μ_H with the decrease of n_e is indicative of grain boundary scattering, and is determined by various characteristics of the grain boundary such as grain size and defect density at the grain boundary. Therefore, it is highly crucial to identify quantitatively defects that act as grain boundaries in the epitaxial TTO films to explain the behavior in Fig. 2.3(c). Possible candidates are boundaries at triple domains, small angle grain boundary due to island growth, and {101} CSP. At present, identification, estimation, and separation of the effect of these defects on μ_H are extremely challenging and are beyond the scope of this study.

3.4 Summary

I compared the XRD patterns and transport properties of TTO epitaxial films on Al_2O_3 (0001) and polycrystalline films on glass grown in the same deposition run. The crystal structure of epitaxial films was almost independent of Ta content, while the preferred growth plane of the polycrystalline films was significantly influenced by Ta doping. The epitaxial films exhibited 2.4×10^{-4} Ωcm at $x = 0.025$~0.03 comparable with the previous reports whereas the polycrystalline films showed approximately three times higher ρ values of 7×10^{-4} Ωcm at $x = 0.015$~0.03. The reduced ρ values in the epitaxial films mainly resulted from μ_H values two times higher than those for the polycrystalline films at $x \geq 0.02$. The highest μ_H for the epitaxial films was 53.2 $cm^2V^{-1}s^{-1}$ obtained at

$x = 0.015$ whereas the highest μ_H for the polycrystalline films was 35.5 $cm^2V^{-1}s^{-1}$ obtained at $x = 0$. This result clearly demonstrates that epitaxial growth is useful for enhancing μ_H in SnO_2 films.

Chapter 4 Enhanced Mobility in Ta-doped SnO_2 on Glass Substrates by Seed Layer Method*

In this chapter, I investigated the use of rutile oxides like TiO_2 and NbO_2 as seed-layers for SnO_2. These materials are isostructural to SnO_2 and are thus expected to promote epitaxial-like growth of SnO_2 on glass substrates. The TTO films grown on the 10-nm-thick seed-layers exhibited (110)-preferential growth and enlarged crystalline grains. Very high μ_H values of 66~68 $cm^2V^{-1}s^{-1}$ were obtained for the TTO films on both rutile TiO_2 and NbO_2. These values are even higher than those obtained for epitaxial TTO films grown on Al_2O_3 (0001).

4.1 Introduction

As shown in the previous chapter, epitaxial growth is useful for enhancing μ_H in SnO_2 films. A feasible method to achieve epitaxial growth on glass substrates is seed-layer method: a thin seed-layer deposited on glass is used as a template on which high-quality SnO_2 films are grown. The seed layer method has been successfully applied to TiO_2- [85] and CdO-based [86] TCOs whereas the effect of seed layer was ambiguous in ITO [87] probably due to insignificant role of grain boundary scattering in ITO.

* A version of this chapter has been published in Thin Solid Films 518, 3093 (2000).

The criteria for selecting materials as the seed layers are summarized as follows. First, the materials should promote epitaxial growth of the main layers; crystal structure and lattice parameters of the seed layers are preferably as close to those of main layers as possible. Second, the materials should exhibited oriented growth, high crystallinity, and/or large grain even with thin thickness, none of which can be achieved by self-seed layer of SnO_2. Third, the materials should be easily available and nontoxic. Fourth, the materials should be transparent in the wavelength of interest.

In this chapter, I explored rutile oxides, which are isostructural to SnO_2, for use as seed layer of SnO_2. Figure 4.1(a) shows lattice parameters of various materials with rutile structure. Apparently, rutile TiO_2 and NbO_2, which are rather easily available and nontoxic, exhibit lattice parameters relatively close to SnO_2 and are thus expected to work as the seed layer for SnO_2. Efforts to fabricate better-lattice-matched TaO_2 and MgF_2 ended in vain.

4.2 Film Growth

TTO thin films with x = 0.003~0.1 in $Sn_{1-x}Ta_xO_2$ were fabricated on alkaline-free glass substrates (Corning 1737) with and without rutile TiO_2 and NbO_2 seed layers. The structure of the prepared films, including the glass substrate, seed-layer and the TTO film grown on top, is schematically illustrated in Fig. 4.1(b). 10-nm-thick seed-layers were deposited on unheated glass substrates by PLD with the oxygen partial pressure during the deposition set at 1×10^{-6} Torr and $<3 \times 10^{-8}$ Torr (i.e., no oxygen introduction) for rutile TiO_2 and NbO_2, respectively. Sintered pellets of TiO_2 and Nb_2O_5 were used as the targets.

For TTO deposition, the substrate temperature and the oxygen partial pressure were set to 600 °C and 3×10^{-3} Torr, respectively. Sintered pellets composed of SnO_2 and Ta_2O_5 were used as PLD targets. Repetition rate of the laser for deposition was 2 Hz. The film thickness of the TTO layer was 110 ± 20 nm.

4.3 Results and Discussion

Figure 4.1(c) shows the XRD patterns of TTO films with x = 0.05 grown on seed-layers and on bare glass. On bare glass without the seed-layer, the 101 diffraction peak is quite prominent. In contrast, the 110 peak becomes significant on the seed-layers, as is evident from the XRD pattern of the TTO films on rutile TiO_2. As shown in Fig. 4.2, the (110) preferential growth on the seed-layers occurs in the entire doping range, in sharp contrast to the complicated behavior of the films on bare glass (Fig. 3.1(b)). This suggests that the seed-layers promote the (110) preferential growth of the TTO films through an epitaxial-like interaction, similar to the case of the epitaxial TTO films on Al_2O_3 (0001) (Fig. 3.1(a)). (110) is considered to be the most energetically stable surface in TiO_2 [89]. Therefore, exposed surface of the TiO_2 seed layer might consist of (110) planes, which can explain (110)-preferred growth of TTO on the seed layer. On NbO_2, the (110) preferential growth was less significant as shown in Fig. 4.1(c). I speculate that NbO_2 is partly oxidized to Nb_2O_5 during the initial stage of the TTO film growth, resulting in the suppression of the epitaxial interaction between the TTO films and the NbO_2 seed-layer.

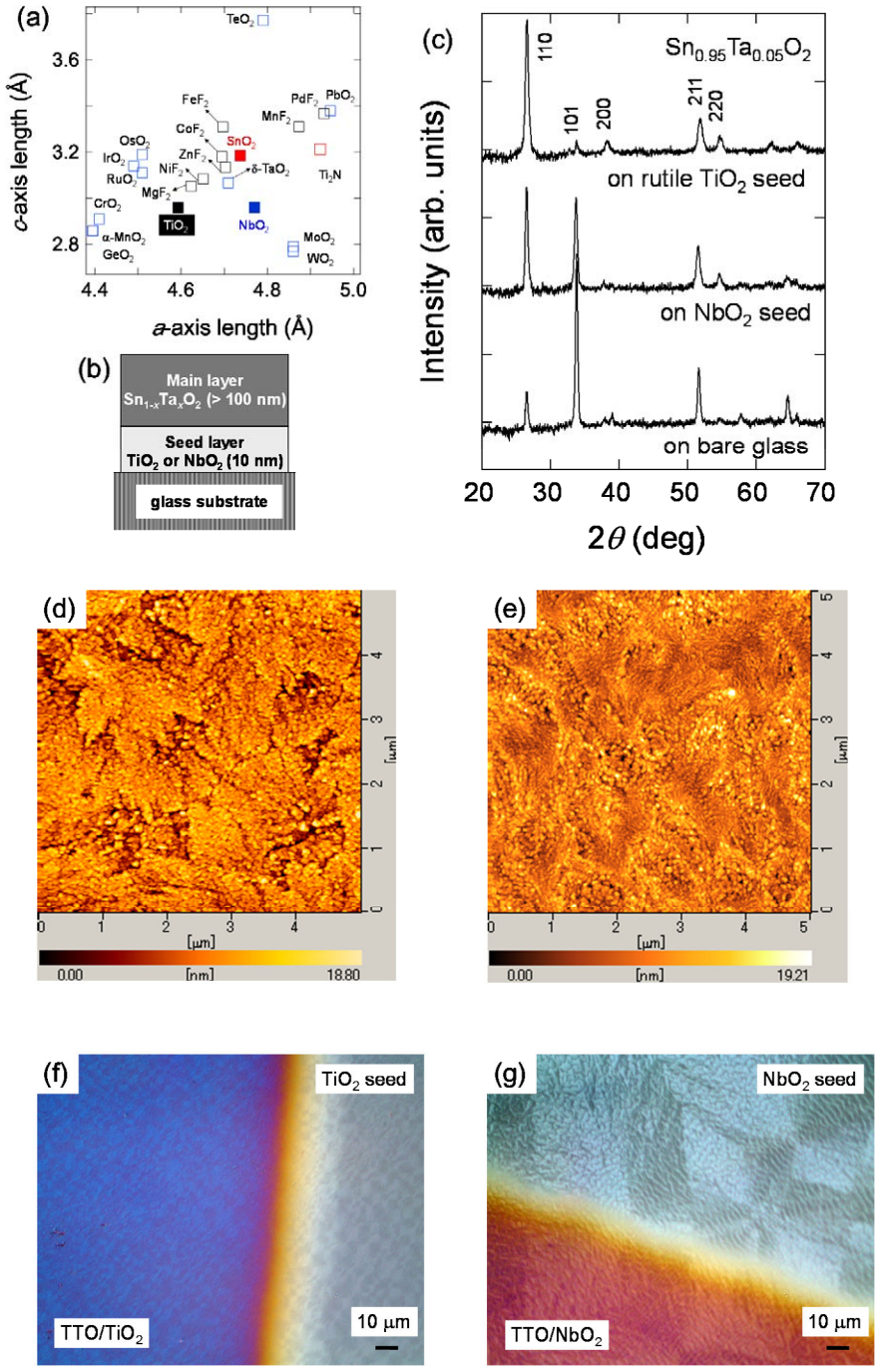

Fig. 4.1. (a) Lattice parameters of materials with rutile structure. Data are taken from ref 88. (b) Schematic of the film structure. (c) XRD patterns of $Sn_{0.95}Ta_{0.05}O_2$ thin films on various seed-layers. AFM images for the $Sn_{0.95}Ta_{0.05}O_2$ thin films grown on (d) rutile TiO_2 and (b) NbO_2 seed layers. Polarized light microscope images for the $Sn_{0.95}Ta_{0.05}O_2$ thin films grown on (d) rutile TiO_2 and (b) NbO_2 seed layers. The images were taken near the edge of the main layers.

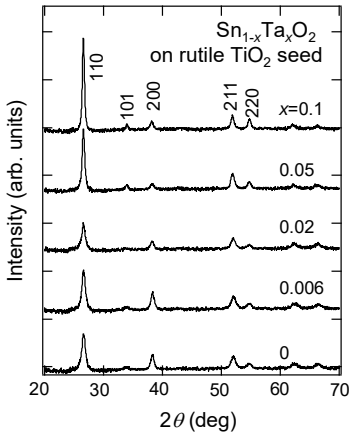

Fig. 4.2. XRD patterns of TTO thin films on rutile TiO_2 seed layers.

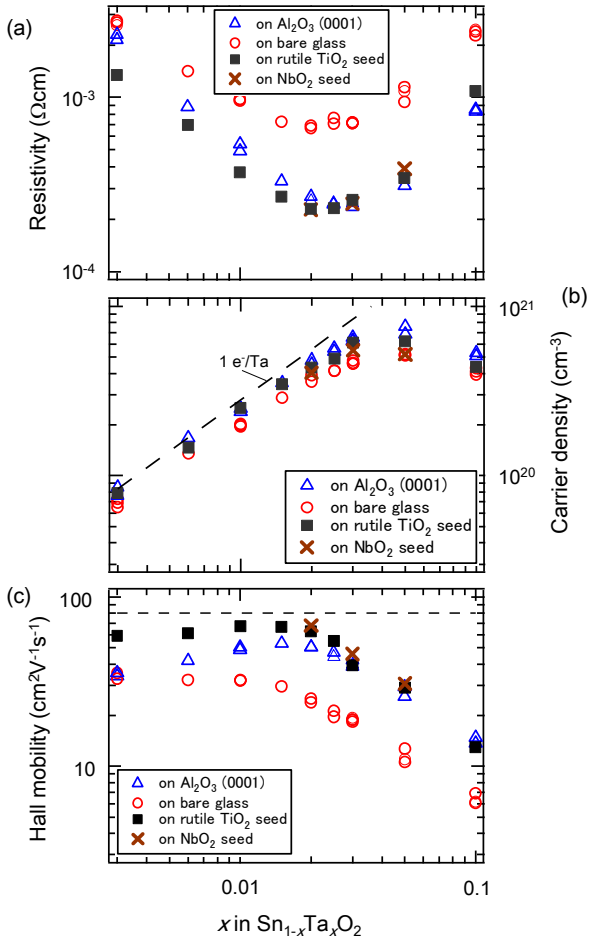

Fig. 4.3. Room temperature (a) ρ, (b) n_e, and (c) μ_H of TTO films on Al_2O_3 (00101) (triangles), bare glass (circles), rutile TiO_2 (squares) and NbO_2 (crosses) seed layer as a function of x. The dashed line in (c) is the target value (80 $cm^2V^{-1}s^{-1}$).

The seed layer affected not only growth orientation but also grain size of TTO. Figs. 4.1(d) and 4.1(e) shows AFM images of the TTO films obtained on the rutile TiO_2 and NbO_2 seed-layers. On bare glass (Fig 3.2(a)), the grain size estimated using the surface morphology is at most a few tens of nanometers, whereas the TTO films on the seed layers and Al_2O_3 (0001) exhibit grain sizes of several tens of nanometers. These results suggest that nucleation of the TTO films on the seed layers are similar to that on single crystalline substrates. In addition to the crystalline grains, μm-scale structures were observed for the TTO films on both rutile TiO_2 and NbO_2 seed layers. As seen in polarized light microscope images (Figs. 4.1(f) and 4.1(g)), the structures originated from the seed-layers grown by solid phase crystallization [90].

Owing to the oriented growth and enlarged grains by the seed layer, the TTO film grown on the seed layer exhibited dramatically improved transport properties. Fig. 4.3 shows the transport properties of the TTO films on the rutile TiO_2 and NbO_2 seed layers together with the data for the polycrystalline an epitaxial TTO films (Fig. 3.3). Clearly, the TTO films on the seed layers exhibited transport properties similar to that for the epitaxial films grown on Al_2O_3 (0001). The lowest ρ values for the films on both rutile TiO_2 and NbO_2 were 2.3×10^{-4} Ωcm, which was even slightly lower than that for the epitaxial film, 2.4×10^{-4} Ωcm. More importantly, the μ_H values for the TTO films on the seed layers were clearly higher than those for the epitaxial films, as seen in Fig. 4.3(c). Very high μ_H values of 66~68 $cm^2V^{-1}s^{-1}$ at n_e of $2.5\sim4.3 \times 10^{20}$ cm^{-3} were obtained for the TTO films on both rutile TiO_2 and NbO_2. These values are even higher than a criterion for high μ_H TCOs proposed by Calnan and Tiwari, 62.5 $cm^2V^{-1}s^{-1}$ [25].

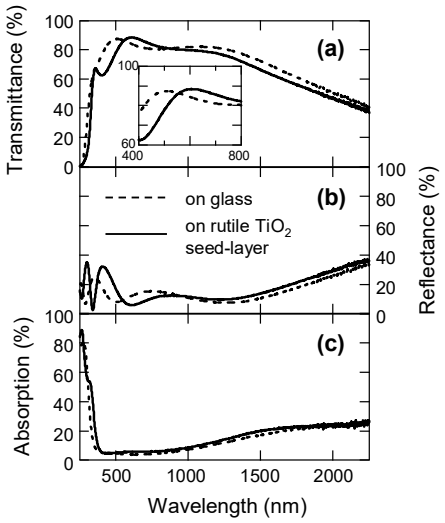

Fig. 4.4. (a) Transmittance, (b) reflectance, and (c) absorption spectra of a 130-nm-thick $Sn_{0.95}Ta_{0.05}O_2$ film on glass (dashed) and on 10-nm-thick rutile TiO_2 seed-layer (solid). The inset of (a) shows the magnified transmittance spectra in the visible region. (Copyright (2010) Elsevier)

Finally, we briefly mention the optical properties of TTO films grown on the seed layers. Fig. 4.4 shows the transmittance, reflectance, and absorption spectra of a 130-nm-thick TTO film on bare glass and on a 10-nm-thick rutile TiO_2 seed-layer. The absorption spectra of both films were almost identical and exhibited low absorption in the visible region at the wavelength of 400~800 nm. Consequently, both films exhibited high transparency in the visible region, as shown in the inset of Fig. 4.4(a). The averaged transmittance values in the visible region are 83% and 81% for the TTO films on glass and on the rutile seed-layer, respectively. Such high transparency was also observed in the TTO films on the NbO_2 seed-layer. Therefore, I conclude that 10-nm-thick seed-layers have little effect on the transparency.

4.4 Summary

I employed a seed-layer method, using NbO_2 and rutile TiO_2 with a thickness of 10 nm as a template for epitaxial-like growth of the TTO film on glass substrates in order to improve μ_H of TTO. The TTO films grown on the 10-nm-thick seed-layers exhibited (110)-preferential growth and enlarged crystalline grains. Very high μ_H values of 66~68 $cm^2V^{-1}s^{-1}$ were obtained for the TTO films on both rutile TiO_2 and NbO_2. These values are even higher than those obtained for epitaxial TTO films grown on Al_2O_3 (0001). These findings indicate that the seed-layer method is effective for fabricating highly μ_H TTO thin films on glass substrates.

Chapter 5 High Mobility Exceeding 80 $cm^2V^{-1}s^{-1}$ in Ta-doped SnO_2 Thin Films on Glass Using Anatase TiO_2 Seed Layers*

In this chapter, I explored oxides having different crystal structure from SnO_2 for the use of seed layer for SnO_2. The use of 10-nm-thick polycrystalline anatase TiO_2 seed layers was found to lead to the preferred growth of (200)-oriented TTO films, resulting in a 30% increase in n_e and a more than two times increase in μ_H, compared with films grown directly on glass substrates. The maximum μ_H obtained was 83 $cm^2V^{-1}s^{-1}$ ($n_e = 2.7 \times 10^{20}$ cm^{-3}, $\rho = 2.8 \times 10^{-4}$ Ωcm) at $x = 0.01$ in $Sn_{1-x}Ta_xO_2$. This μ_H value was even the highest among those for doped SnO_2 films thus far reported. Although further reduction in n_e without reducing μ_H was required, this is the first result that achieved the target μ_H value of 80 $cm^2V^{-1}s^{-1}$.

* Two versions of this chapter have been published in Appl. Phys. Express 3, 031102 (2010). and MRS proc. 1604 (2014).

5.1 Introduction

In the previous chapter, enhanced μ_H in TTO films on glass was successfully demonstrated by epitaxial-like growth using seed layer of isostructural oxides such as rutile TiO_2 and NbO_2. However, even optimized films exhibited μ_H lower than the target value (80 $cm^2V^{-1}s^{-1}$). Therefore, further exploration for the seed layer is necessary.

In this chapter, I extended the exploration of seed layer from rutile oxides to other materials such as rutile fluorides and oxides having different crystal structures. Although several rutile fluorides have lattice parameters close to those of SnO_2 as shown in Fig. 4.1(a), rutile fluorides are often unsuitable for the seed layer for several reasons. First, fluorides are in general unstable; they are reactive with moisture in air and volatile in vacuum at high temperature. Second, some of the fluorides shown in Fig 4.1(a) are nontransparent. For example, CoF_2 and NiF_2 are, respectively, pink and green to human eyes. An exceptional and promising rutile fluoride for the seed layer of SnO_2 might be MgF_2 owing to several excellent properties: wide band gap (and thus excellent transparency), fair stability both in air and at high temperatures, easy availability in industry as low refractive index coatings, and lattice parameters close to SnO_2. However, the band gap of MgF_2 was too wide to ablate with the KrF excimer laser used in this study. Therefore, I abandoned fluorides and focused on oxides having different crystal structure from SnO_2 for the use of seed layer.

Epitaxial growth with large lattice mismatch exceeding 10% (so-called domain match epitaxy) has been reported for some oxides [91]. Therefore, in this chapter, I ignored

lattice matching and explored oxides for the seed layer of SnO_2 from other criteria mentioned in chapter 4: oriented growth, high crystallinity, large grain, availability, and nontoxicity. ZnO was apparently promising owing to c-axis oriented growth on glass substrates. Indeed, ZnO seed layers promoted (100)-oriented growth of SnO_2 (see appendix B, Fig. B.1). However, no clear improvement in μ_H was observed for the (100)-oriented SnO_2 films grown on the ZnO seed layers. I speculated that Zn diffused into the grain boundary of the SnO_2 during high temperature deposition and suppressed the μ_H of the SnO_2 films.

Another candidate is anatase TiO_2. Anatase TiO_2 grown from amorphous precursor [60] exhibits various excellent properties suitable for seed layers: high crystallinity as confirmed by μ_H comparable with epitaxial films [60, 92] and large crystalline grains exceeding 10 μm [93] with domains exceeding 100 nm [63, 94]. In this chapter, I found anatase TiO_2 an excellent seed layer for SnO_2. The use of 10-nm-thick polycrystalline anatase TiO_2 seed layers was found to lead to the preferred growth of (200)-oriented TTO films, resulting in a 30% increase in n_e and a more than two times increase in μ_H, compared with the polycrystalline TTO films. An optimized film exhibited very high μ_H of 83 $cm^2V^{-1}s^{-1}$ ($n_e = 2.7 \times 10^{20}$ cm^{-3}, $\rho = 2.8 \times 10^{-4}$ Ωcm), which exceeded the target μ_H value of 80 $cm^2V^{-1}s^{-1}$.

5.2 Film Growth

Both the TiO_2 seed layers and TTO films with x = 0.003~0.1 in $Sn_{1-x}Ta_xO_2$ were deposited by PLD at a repetition rate of 2 Hz. Amorphous TiO_2 seed layers with a thickness of 10 nm were deposited on unheated alkaline-free glass (Corning, 1737) at an oxygen partial pressure of 3×10^{-3} Torr. The as-deposited seed layers were then annealed at 600 °C in the PLD chamber to produce a polycrystalline anatase TiO_2 phase. TTO films were subsequently grown on the TiO_2 seed layers at an oxygen partial pressure of 3×10^{-3} Torr and a substrate temperature of 600 °C. The typical thickness of the TTO films was 110 ± 20 nm. Thicker films with R_s below 10 $\Omega sq.^{-1}$ were used for optical measurements.

5.3 Results and Discussion

Figures 5.1(a) and (b) show XRD patterns of TTO films deposited on glass with and without anatase TiO_2 seed layers (hereafter in this chapter shortly referred to as the seed layer), respectively. From the XRD patterns for the TTO films on glass without the seed layers, it can be seen that the film is polycrystalline with random grain orientations. The films on glass showed a typical fine columnar structure as observed by TEM in Fig. 5.2(a). From the AFM image shown in Fig. 5.1(c), the dimensions of the grains are a few tens of nanometers at the surface. In addition, I estimated grain size from the 211 diffraction peak of the TTO film on glass by using the Scherrer equation where 0.9 was used as shape factor. The obtained value of 20 nm was consistent with the AFM observation.

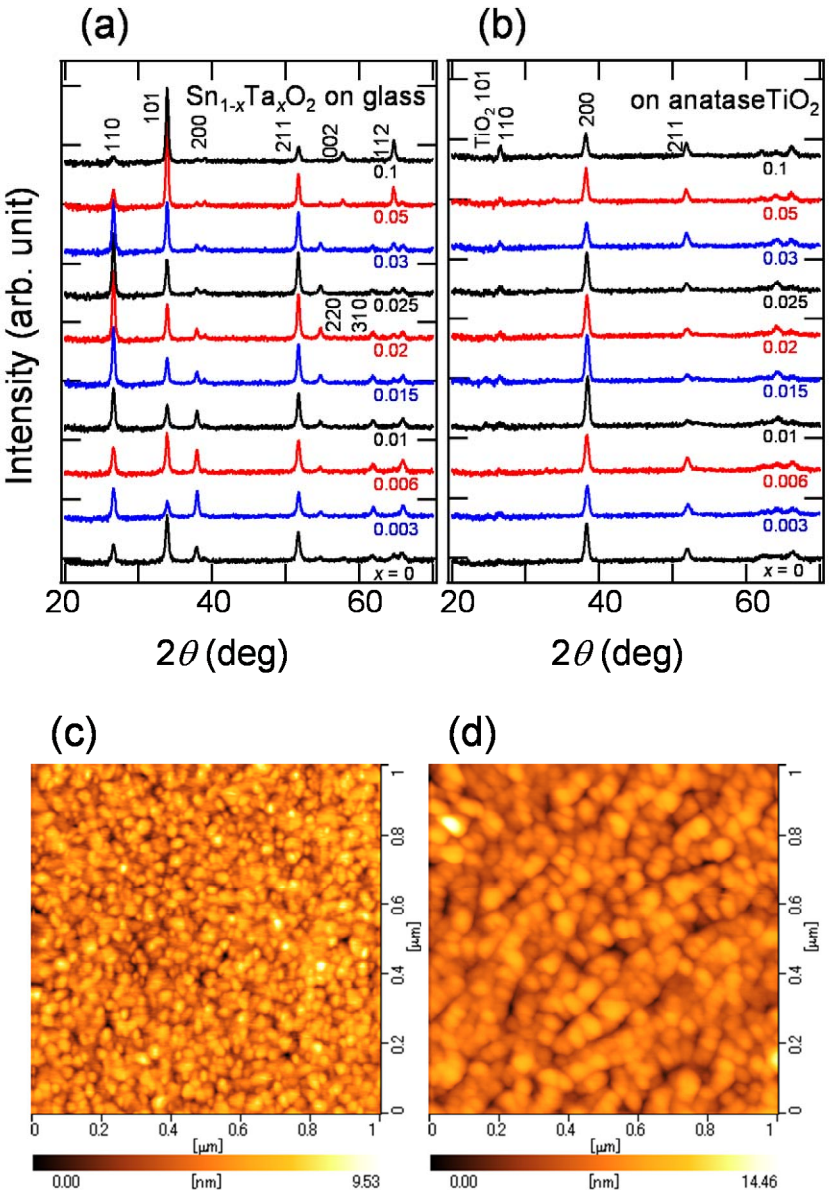

Fig. 5.1. XRD patterns of TTO films on (a) glass and (b) anatase TiO_2 seed layers. AFM images of TTO (x = 0.02) films on (c) glass and (d) anatase TiO_2 seed layer.

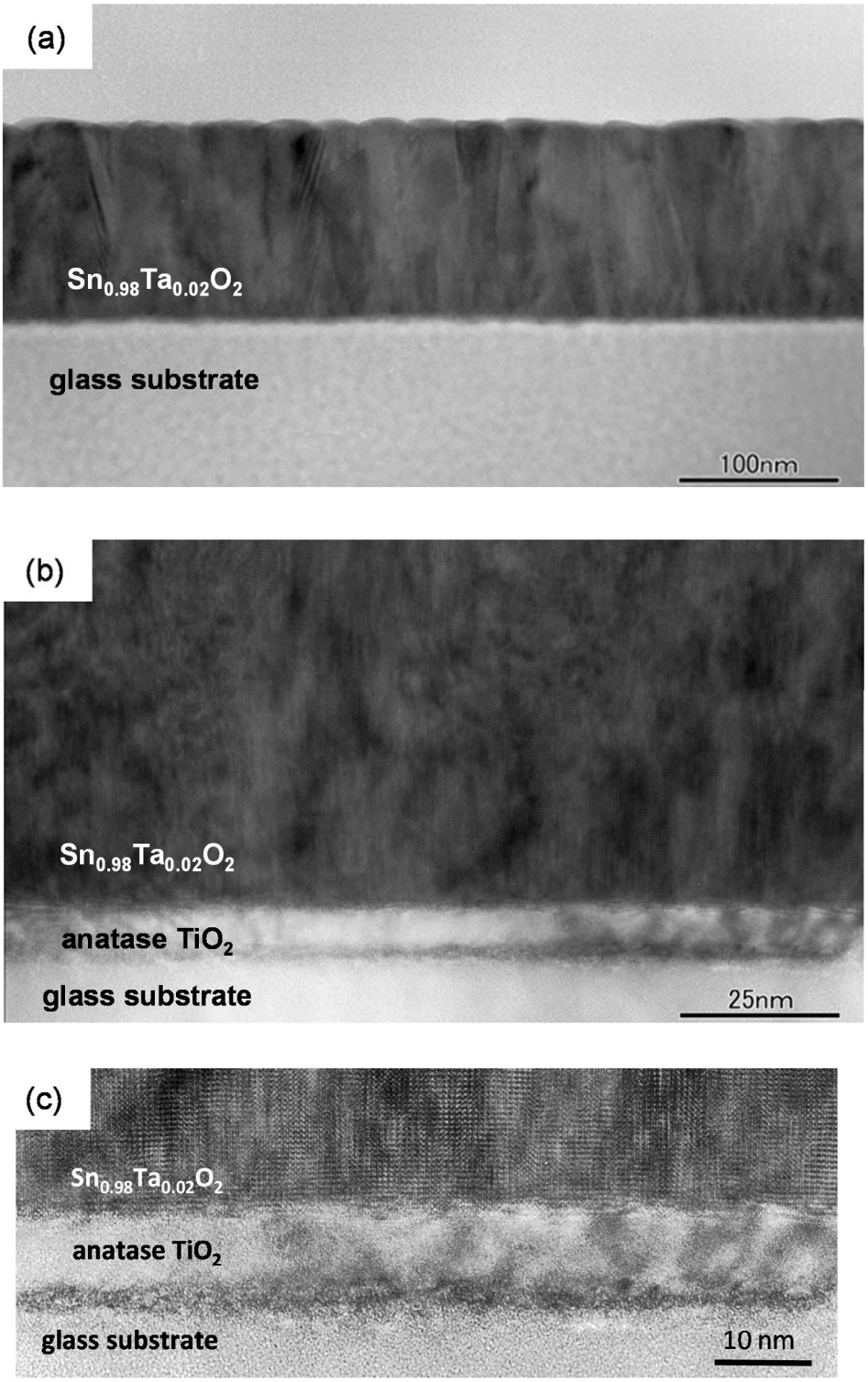

Fig. 5.2. Cross sectional TEM images of $Sn_{0.98}Ta_{0.02}O_2$ films on (a) glass and (b) anatase TiO_2 seed layer. (c) High magnification TEM image of (b) near the seed layer.

These characteristics are typical for polycrystalline films on glass substrates. In contrast, the TTO films on the seed layers exhibit a preferred (200) orientation, as evidenced by the strongly enhanced (200) peak intensity. I confirmed that films with a preferred (200) orientation could be produced for the entire doping range examined in this study, as shown in Fig. 5.1(b). The (200) orientation was also confirmed by cross-sectional TEM observations [Fig. 5.2(c)]. Furthermore, cross sectional TEM observation reveled that high angle grain boundaries were absent in the films as shown in Fig. 5.2(b). The TTO films on the seed layers exhibited larger grains with dimensions of several tens of nanometers, as shown in Fig. 5.1(d). This result was, however, inconsistent with grain size of 16 nm obtained from the 200 diffraction peak of the TTO films on the seed layers by using the Scherrer equation. This is probably because peak broadening in epitaxially strained films led to underestimation of grain size using the Scherrer equation. At present, the mechanism behind the preferred (200) growth on the polycrystalline anatase seed layer is unclear. However, it should be noted that the c-axis spacing of anatase TiO_2 (0.951 nm) is approximately double the a-axis spacing of SnO_2 (0.474 nm). This suggests that the epitaxial relationship between SnO_2 (100) and anatase TiO_2 (100) planes may promote the preferred (200) growth of SnO_2.

Figure 5.3 shows the room-temperature transport properties of the TTO films. In the low doping region with $x < 0.01$, the n_e value of the TTO films on the seed layer is proportional to x and follows the dotted line representing 100% ionization efficiency, indicating that each Ta^{5+} ion substituting for an Sn^{4+} ion contributes a single carrier electron. Such a high activation efficiency is a characteristic feature of TTO [47]. For $x > 0.03$, n_e becomes saturated at a value of $\sim 7 \times 10^{20}$ cm^{-3}.

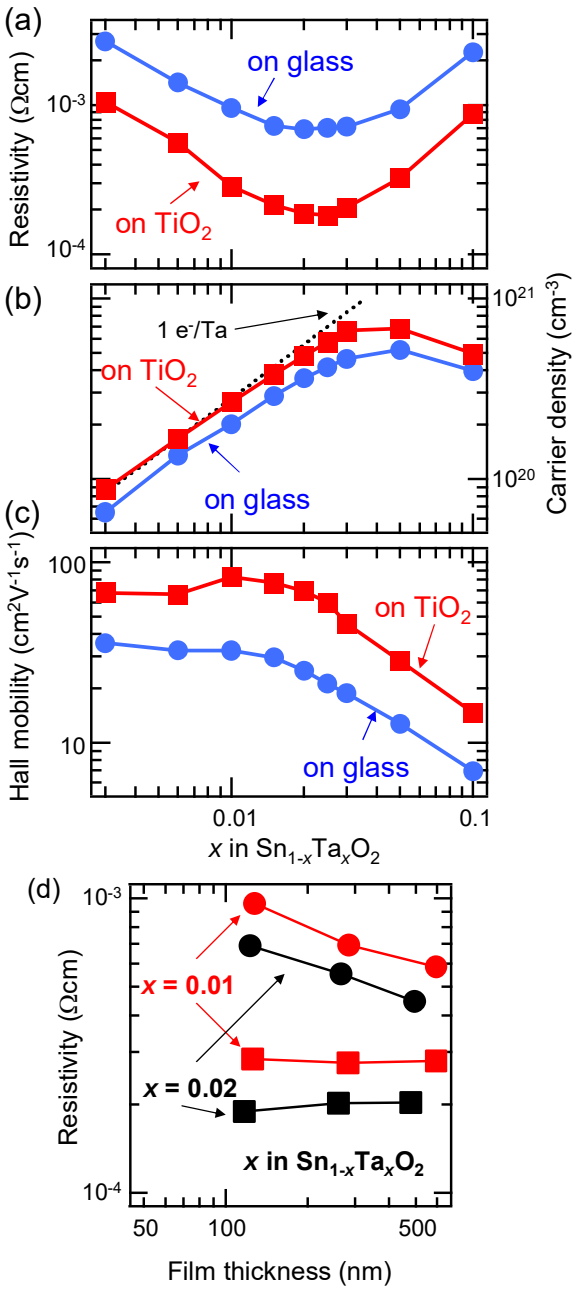

Fig. 5.3. (a) ρ, (b) n_e, and (c) μ_H of TTO films on glass (circles) and anatase TiO_2 seed layers (squares) as a function of Ta content, x, in $Sn_{1-x}Ta_xO_2$. The dashed line represents 100% activation efficiency. (d) Film thickness dependence of ρ for TTO films on glass (circles) and anatase TiO_2 seed layers (squares).

The n_e values of the TTO films are approximately 30% lower than those of the TTO films on the seed layer. In addition to crystallinity discussed in chapter 3, I speculate that the random grain orientation leads to the presence of a variety of defects which compensate for the carriers generated by Ta-doping. Bélanger *et al.* [38] examined the transport properties of doped SnO_2 films as a function of thickness and found that for thinner films with thickness below 1 μm, the carrier concentration decreased with the decrease of the thickness. Considering the charge neutrality of the surfaces, they proposed that polar surfaces such as (110) and (101) tend to contain Sn^{2+} ions, which behave as traps for carriers, whereas the nonpolar (200) surface does not contain such traps [38, 95].

As observed in Fig. 5.3(c), the μ_H values of TTO films on the seed layer are systematically 2–3 times larger than those of the TTO films on glass and reach a maximum of 83 $cm^2V^{-1}s^{-1}$ ($n_e = 2.7 \times 10^{20}$ cm^{-3}, $\mu_H = 2.8 \times 10^{-4}$ Ωcm) at $x = 0.01$. This remarkably high μ_H value is the largest ever reported for doped epitaxial or polycrystalline SnO_2 thin films as shown in the inset of Fig. 5.4, and is comparable to the μ_H values of high-μ_H In_2O_3-based TCOs (Table 1.2). More importantly, this is the first result that achieved the target μ_H value of 80 $cm^2V^{-1}s^{-1}$ although further reduction in n_e without reducing μ_H was required as shown in Fig. 5.4. This high μ_H value can be attributed to the preferred (200) growth orientation in addition to the larger grain size in the films, which result in reduced carrier scattering at grain boundaries. I obtained a minimum ρ of 1.8×10^{-4} Ωcm ($n_e = 5.7 \times 10^{20}$ cm^{-3}, $\mu_H = 60$ $cm^2V^{-1}s^{-1}$) at $x = 0.025$, which is one of the lowest ever reported for SnO_2 films [47, 96, 97]. I confirmed that the ρ values of the TTO films on the seed layers were independent of the thickness of the TTO layers as shown in Fig. 5.3(d).

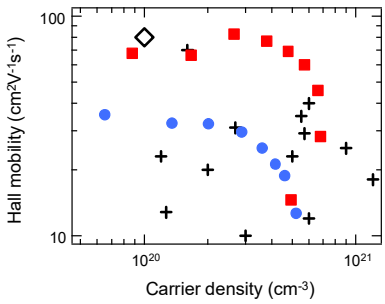

Fig. 5.4. Comparison of n_e and μ_H values for the TTO films on glass (circles) and anatase TiO_2 seed layers (squares) with those of SnO_2-based TCOs (crosses) previously reported in Ref. 6 and the target value in this study (diamond).

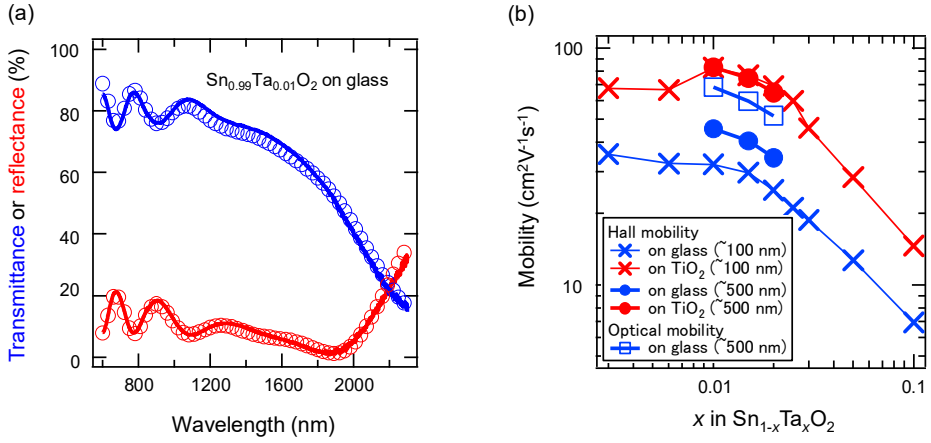

Fig. 5.5. (a) Typical optical properties (solid lines) of the TTO films and corresponding fit (circles) based on the Drude model. (b) Comparison of optical mobility (squares) and μ_H (crosses and circles) of the TTO films.

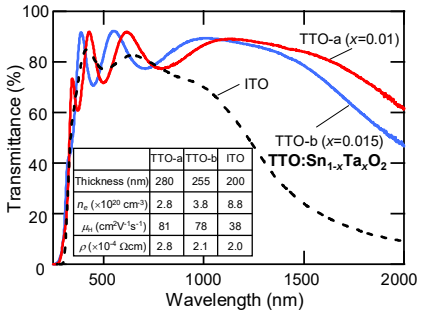

Fig. 5.6. Comparison between optical transmittance spectra of the TTO (x = 0.01 and x = 0.015) films on anatase TiO_2 seed layers and a typical ITO film. The inset shows the electrical properties of these films. (Copyright (2010) The Japan Society of Applied Physics)

This result indicates that no interfacial conductivity contributes to the ρ values of the TTO films on the seed layers. Moreover, I directly measured ρ of a 10-nm-thick anatase TiO_2 seed layer after etching off TTO film. As a result, I found that the seed layer showed $\rho = 1 \times 10^{-1}$ Ωcm ($n_e = 3 \times 10^{19}$ cm^{-3}, $\mu_H = 2$ $cm^2V^{-1}s^{-1}$), which is a reasonable value for undoped polycrystalline anatase TiO_2 [60]. Therefore, the seed layer has a negligible influence on the ρ of TTO films on the seed layers. These results clearly demonstrate that the excellent transport properties of the TTO films on the seed layers were derived from the TTO layers. Here, we noted that the TTO films on glass showed reduced ρ with the increase in the film thickness, which has been widely reported in FTO films by CVD [39, 40]. Very recently, Isshiki *et al.* investigated film thickness dependence of transport properties of FTO films in detail [40]. They found that the topmost layer in 1-μm-thick films with large grains is estimated to exhibit high μ_H of ~80 $cm^2V^{-1}s^{-1}$ in spite of low μ_H (~10 $cm^2V^{-1}s^{-1}$) of initial layer. Thus, μ_H of SnO_2 films free from grain boundary scattering can be as high as ~80 $cm^2V^{-1}s^{-1}$. The seed layer method allows us to obtain such high μ_H even in the initial stage of the film growth.

In order to confirm reduced grain boundary scattering in the TTO films on the seed layer, optical mobility was estimated from transmittance and reflectance spectra as shown in Fig. 5.5. Fitting results on the experimental data were fair for the TTO films on glass as shown in Fig. 5.5(a). On the other hand, no satisfactory fitting results on the experimental data were obtained for the TTO films on the seed layers due to multilayer structure. As shown in Fig. 5.5(b), the optical mobility values for the TTO films on glass were much higher than the μ_H for the film, demonstrating that grain boundary scattering dominates the

μ_H for the TTO films on glass. Interestingly, the optical mobility values for the TTO films on glass were close to the μ_H values for the TTO films on the seed layers. This suggests that grain boundary scattering in the TTO films on the seed layers is indeed negligible.

Finally, I discuss the optical properties of the TTO films on the seed layers. Figure 5.6 shows a comparison of the transmittance spectra of the TTO (x = 0.01 and 0.015) films and that of a typical ITO with an equivalent ρ. The TTO films maintain high transmittance up to the NIR region (>1000 nm), in sharp contrast to ITO, whose NIR transmittance abruptly decreases with increasing wavelength owing to light absorption by free carriers. This indicates that the transmission window of the TTO is much wider than that of ITO, and is a direct consequence of the high mobility (~ 80 $cm^2V^{-1}s^{-1}$) of the TTO films, which leads to substantially reduced absorption by free carriers in the NIR region. A transmittance of greater than 70% is obtained in the wavelength regions of 400~1640 nm and 400~1850 nm for x = 0.015 and x = 0.01, respectively. Such high transparency in the NIR region makes these films promising candidates for use in the next-generation PVCs by allowing the efficient use of the NIR region of sunlight.

5.4 Summary

I have fabricated polycrystalline TTO films on seed layers of anatase TiO_2 using PLD. The use of the 10-nm-thick TiO_2 seeds promoted preferred (200) growth together with the enlargement of grains, resulting in a 30% increase in n_e and a more than two times increase in μ_H. I obtained μ_H = 83 $cm^2V^{-1}s^{-1}$ ($n_e = 2.7 \times 10^{20}$ cm^{-3}, $\rho = 2.8 \times 10^{-4}$ Ωcm) at

x = 0.01, which is the highest value ever reported for SnO_2-based transparent conductors and is comparable to the values for high- μ_H In_2O_3-based TCOs. Although further reduction in n_e without reducing μ_H was required, this is the first result that achieved the target μ_H value of 80 $cm^2V^{-1}s^{-1}$. Furthermore, a minimum $\rho = 1.8 \times 10^{-4}$ Ωcm ($n_e = 5.7 \times 10^{20}$ cm^{-3}, μ_H = 60 $cm^2V^{-1}s^{-1}$) was attained with a slightly higher Ta content of x = 0.025. The TTO films with x = 0.01 exhibited an optical transmittance of over 70% at wavelengths ranging from 400 to 1850 nm, demonstrating NIR transparency suitable for the next-generation PVCs.

Chapter 6 Effects of Growth Parameters on Structure and Transport Properties of Ta-doped SnO_2 Films on Anatase TiO_2 Seed Layers*

In this chapter, I investigated how the growth parameters such as oxygen partial pressure and substrate temperature affect structure and transport properties of TTO films in detail. (101)-preferred growth, which probably originated from energetically stable nature of oxygen deficient (101) plane, was observed for TTO films on glass grown under oxygen poor ambient or at low substrate temperatures. TTO films grown under oxygen rich ambient showed reduced n_e, suggesting carrier compensation in the film due to excess oxygen. On the other hand, TTO films grown under oxygen poor ambient showed no decrease in n_e but drastic decrease in μ_H. As substrate temperature decreased, TTO films both with and without anatase TiO_2 seed layers showed gradual and rapid decrease in n_e and μ_H, respectively. At low substrate temperatures, amorphization and (101)-preferred growth of TTO competed with epitaxial growth on the seed layer. Introducing sufficient process oxygen suppressed such unwanted film growth, resulting in the epitaxial growth of the TTO films on the seed layer and thus improved transport properties.

* A version of this chapter has been published in MRS proc. 1604 (2014).

6.1 Introduction

In the previous three chapters, growth parameters for the TTO films were fixed at a substrate temperature of 600 °C and oxygen partial pressure of 3×10^{-3} Torr on the basis of initial preliminary experiments (not shown). In this chapter, effects of the growth parameters on structure and transport properties of TTO films were investigated in detail for the following reasons. First, process window in oxygen partial pressure during deposition is important information because the process window is crucial for practical fabrication. For example, ITO shows very wide process window [6]; very low ρ can be obtained in a wide range of oxygen partial pressure during deposition. This is one of the reasons why ITO has been widely used in industry. Second, lower temperature deposition than 600 °C is preferable because heat sensitive substrates such as plastic (maximum temperature for use: 100~200 °C) and soda-lime glass (maximum temperature for use: 450 °C) are unavailable at 600 °C. Use of such substrates instead of rather expensive alkaline-free glass would reduce cost and/or weight of PVCs. Last, the growth parameters dependence of various properties is important in its own right because it might lead to better understanding of the defects in TTO.

6.2 Film Growth

Both the TiO_2 seed layers and TTO films were deposited by PLD at a repetition rate of 2 Hz. Amorphous TiO_2 seed layers with a thickness of 10 nm were deposited on

unheated alkaline-free glass (Corning, 1737) at an oxygen partial pressure of 3×10^{-3} Torr. The as-deposited seed layers were then annealed at 600 °C in the PLD chamber to produce a polycrystalline anatase TiO_2 phase. TTO films were subsequently grown on the anatase TiO_2 seed layers (hereafter in this chapter shortly referred to as the seed layer). Substrate temperature and oxygen partial pressure during TTO deposition were 300~600 °C and 3×10^{-4}~1×10^{-1} Torr, respectively. The film thickness of the TTO films was 110 ± 20 nm.

6.3 Results and Discussion

(1) Oxygen Partial Pressure Dependence

Figure 6.1 shows oxygen partial pressure dependence of XRD patterns for $Sn_{0.95}Ta_{0.05}O_2$ films deposited at a fixed substrate temperature of 600 °C. Prominent (101)-preferred growth was observed for the $Sn_{0.95}Ta_{0.05}O_2$ films on glass deposited under oxygen-poor ambient as shown in Fig. 6.1(a). The preferred growth gradually changed from (101) to (110) with the increase of oxygen partial pressure. In addition, 211 peaks were observed for all the $Sn_{0.95}Ta_{0.05}O_2$ films on glass. The competition between (101)- and (110)-preferred growth has been widely observed for sputtered SnO_2 thin films [84]. The origin of (110)-preferred growth is energetically stable nature of (110) surface [98], whereas (101)-preferred growth can be stabilized with the introduction of oxygen vacancies [84]. In addition to energetically stable (110) and (101) nuclei, recent TEM observation of initial growth stage of SnO_2 films revealed numerous (211) nuclei [99], which might be stabilized by the (101) twin plane [100]. In contrast to the $Sn_{0.95}Ta_{0.05}O_2$ films on glass,

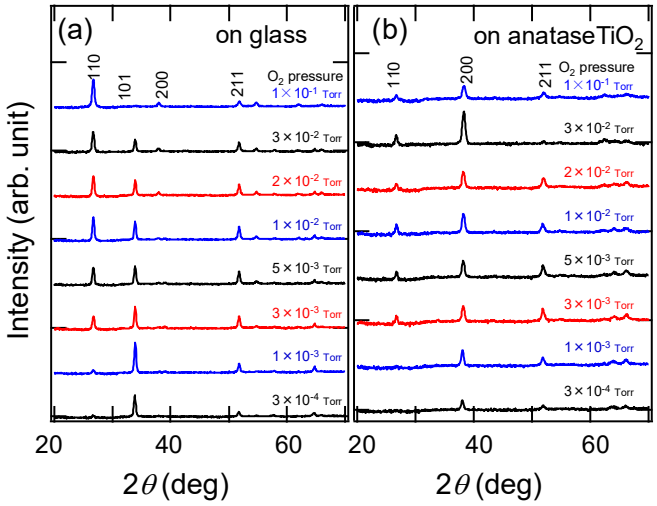

Fig. 6.1. XRD patterns of $Sn_{0.95}Ta_{0.05}O_2$ films on (a) glass and (b) anatase TiO_2 seed layers deposited at various oxygen partial pressures. Substrate temperature was fixed at 600 °C.

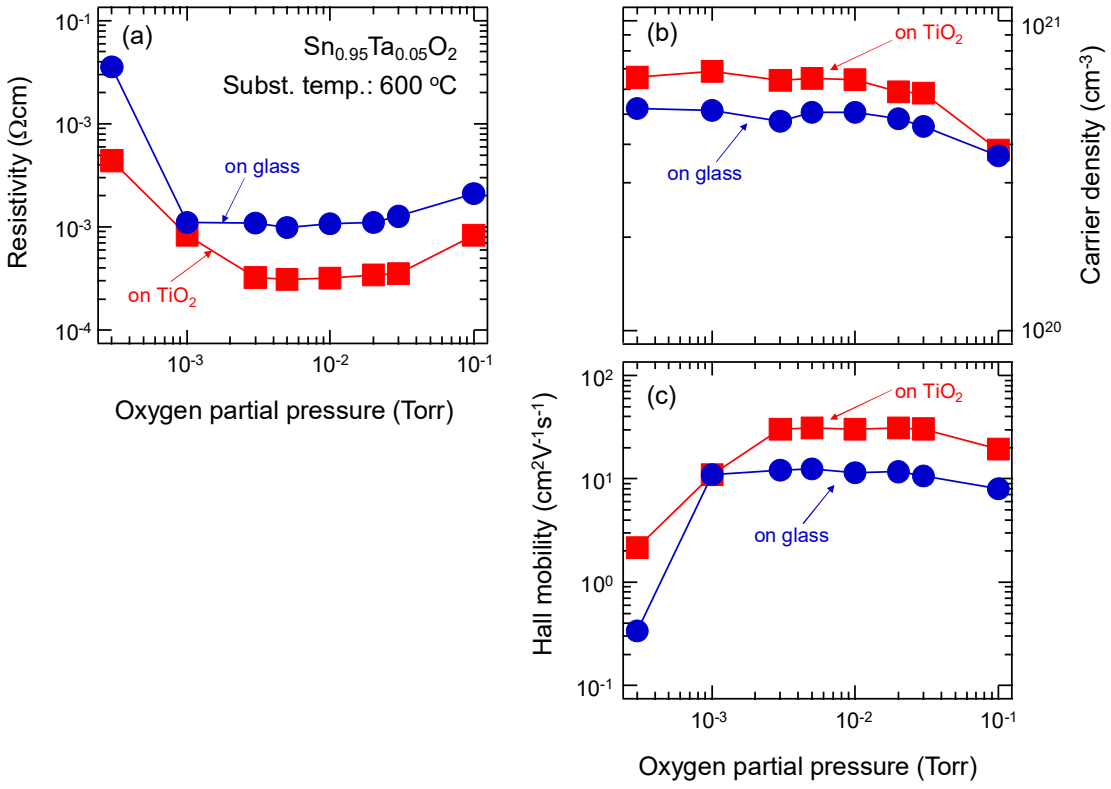

Fig. 6.2. (a) ρ, (b) n_e, and (c) μ_H of $Sn_{0.95}Ta_{0.05}O_2$ films on glass (circles) and anatase TiO_2 seed layers (squares) deposited at various oxygen partial pressures. Substrate temperature was fixed at 600 °C.

the structure of the $Sn_{0.95}Ta_{0.05}O_2$ films on the seed layers was insensitive to oxygen partial pressure as shown in Fig. 6.1(b); 200 diffraction peaks were dominant for all the $Sn_{0.95}Ta_{0.05}O_2$ films on the seed layers. This means that film growth of the $Sn_{0.95}Ta_{0.05}O_2$ films on the seed layers was governed by the seed layer with epitaxial stabilization.

Next, we discuss transport properties. Figure 6.2 shows comparison of transport properties between $Sn_{0.95}Ta_{0.05}O_2$ films with and without the seed layers. The $Sn_{0.95}Ta_{0.05}O_2$ films on the seed layers exhibited much lower ρ than the films on glass. In particular, low ρ of ~3×10^{-4} Ωcm was obtained for the $Sn_{0.95}Ta_{0.05}O_2$ films on the seed layers in wide oxygen partial pressure range from 3×10^{-3} to 3×10^{-2} Torr. This result clearly demonstrates wide process window in oxygen partial pressure for TTO fabrication. The reduced ρ resulted from 30% increase in n_e and tripled μ_H, which I attributed to reduction of grain boundary scattering due to epitaxial growth as well as the enlargement of grain sizes. Here it should be noted that, while high n_e values were obtained for TTO films irrespective of oxygen partial pressure, TTO films grown under oxygen poor ambient showed significantly decreased μ_H. I found slight decrease in deposition rate for such low-μ_H films deposited at oxygen poor ambient. Recently, Zhen *et al.* reported re-evaporation of Sn from growth surface of SnO_2 films [45]. Thus, I speculated that possible re-evaporation of Sn at low oxygen partial pressure could increase the defect density at the grain boundary, resulting in low μ_H. The TTO films grown under oxygen rich ambient showed decrease in n_e, suggesting carrier compensation due to excess oxygen in SnO_2 as well as ITO [101] and Nb:TiO_2 [85, 102].

(2) Substrate Temperature Dependence

Figure 6.3 shows substrate temperature dependence of XRD patterns for $Sn_{0.985}Ta_{0.015}O_2$ films deposited at fixed oxygen partial pressure of 3×10^{-3} Torr. The TTO films on glass showed (101)-preferred growth at low substrate temperatures (350 and 400 °C), followed by amorphization at ≤ 300 °C (data not shown). The amorphous films were characterized by high ρ of > 10^5 Ωcm and yellowish appearance. Details of the transport properties of amorphous SnO_2 films deposited at much lower substrate temperatures are described in appendix C. As shown in Fig. 6.3(b), (101)-preferred growth was observed even for the $Sn_{0.985}Ta_{0.015}O_2$ films on the seed layers grown at low substrate temperatures (350 and 400 °C). At 600 °C (Figs. 5.1 and 6.1), (101)-preferred growth observed for low oxygen partial pressure and high Ta concentration was suppressed by the (200) growth due to the seed layer. These results indicate that (101)-preferred growth competes with (100) epitaxial growth on the seed layer, and reduced adatom mobility at low substrate temperatures is favorable for (101)-preferred growth.

Figure 6.4 shows substrate temperature dependence of the transport properties. The $Sn_{0.985}Ta_{0.015}O_2$ films both with and without the seed layers showed gradual and rapid decrease in n_e and μ_H, respectively, as substrate temperature decreased. The decrease in n_e suggests formation of inactive dopant (Ta^{4+}) and unfavorable defects such as clustered dopants and accepter-like defects, which would reduce μ_H as well. More importantly, the $Sn_{0.985}Ta_{0.015}O_2$ films on the seed layer showed significant decrease in n_e and μ_H at substrate temperatures of 350 and 400 °C, where (101)-preferred growth occurred even on the seed layer; the transport properties of the TTO films with and without the seed layers were

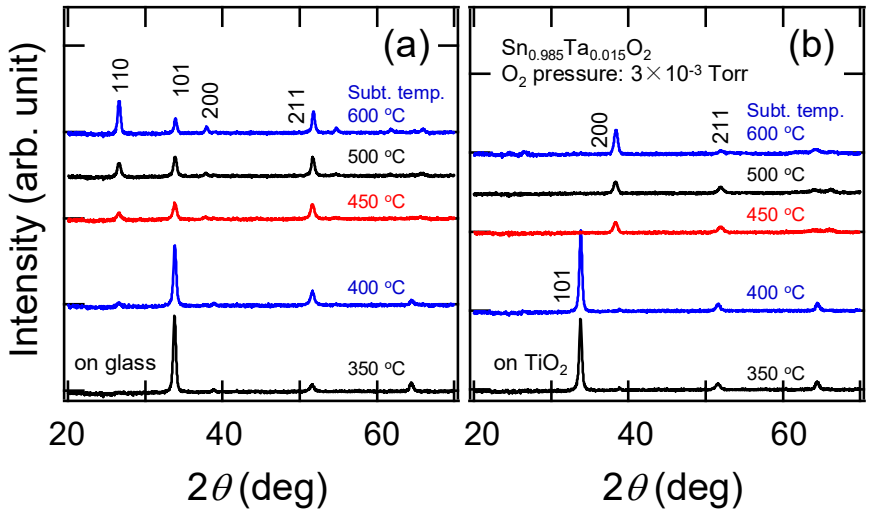

Fig. 6.3. XRD patterns of $Sn_{0.985}Ta_{0.015}O_2$ films on (a) glass and (b) anatase TiO_2 seed layers deposited at various substrate temperatures.

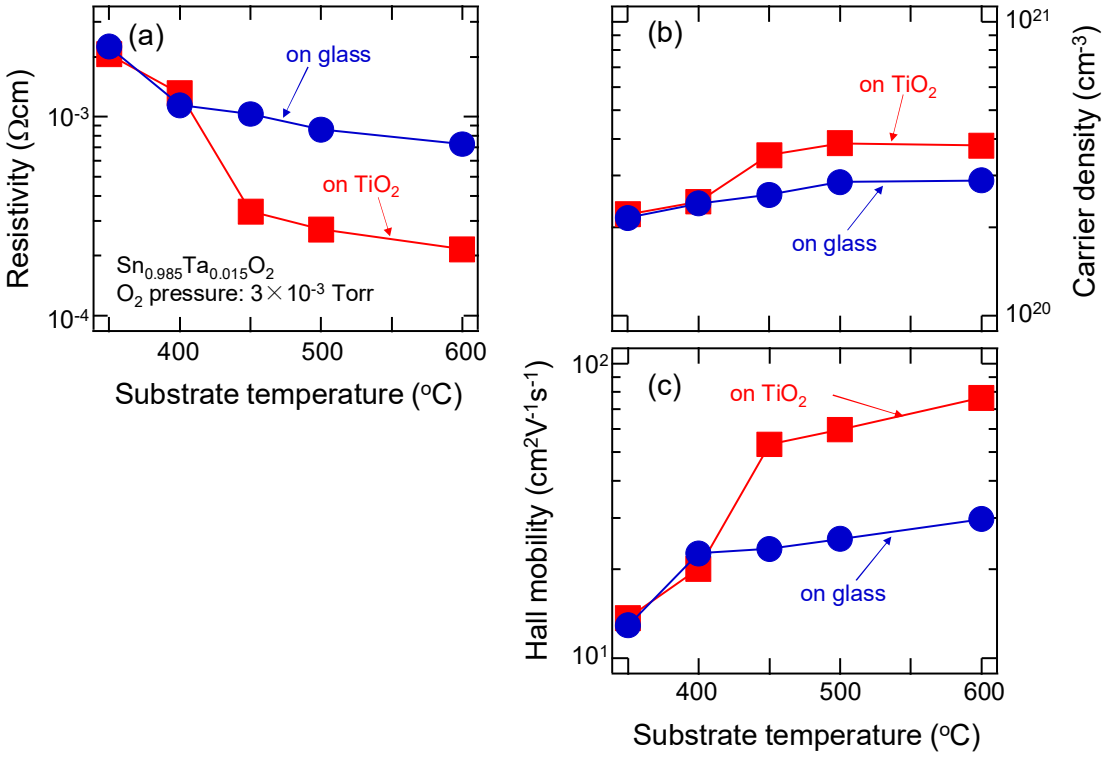

Fig. 6.4. (a) ρ, (b) n_e, and (c) μ_H of $Sn_{0.985}Ta_{0.015}O_2$ films on glass (circles) and anatase TiO_2 seed layers (squares) deposited at various substrate temperatures.

almost identical. This result indicates that epitaxial growth is crucial for the improvement of the transport properties by using the seed layer.

(3) Effect of Oxygen Partial Pressure at Low Substrate Temperatures

As shown above, at low substrate temperatures, unwanted film growth such as amorphization and (101)-preferred growth competes with epitaxial growth on the seed layer, resulting in poor transport properties. Because (101)-preferred growth can be suppressed with the increase of oxygen partial pressure (Fig. 6.1), I investigated effect of oxygen partial pressure at low substrate temperature in order to improve the transport properties of TTO films.

Figure 6.5 and 6.6 show, respectively, XRD patterns and optical properties of the $Sn_{0.985}Ta_{0.015}O_2$ films grown at 300 °C. The film on glass deposited at oxygen partial pressure of 3×10^{-3} Torr were amorphous with yellowish appearance. With the increase of oxygen partial pressure, transparent and polycrystalline films were obtained as seen in drastic increase in transmittance over the 400~600 nm region (Fig. 6.6). The $Sn_{0.985}Ta_{0.015}O_2$ film on glass deposited at oxygen partial pressure of 1×10^{-2} Torr exhibited ρ of 1.1×10^{-3} Ωcm ($n_e = 2.3 \times 10^{20}$ cm^{-3}, $\mu_H = 25$ $cm^2V^{-1}s^{-1}$). Moreover, the $Sn_{0.985}Ta_{0.015}O_2$ film on the seed layer deposited at oxygen partial pressure of 1×10^{-2} Torr showed (100)-growth, and exhibited reduced ρ of 5.1×10^{-4} Ωcm ($n_e = 3.1 \times 10^{20}$ cm^{-3}, $\mu_H = 40$ $cm^2V^{-1}s^{-1}$). These results demonstrated that, at low substrate temperatures, introducing sufficient process oxygen suppressed unwanted film growth such as

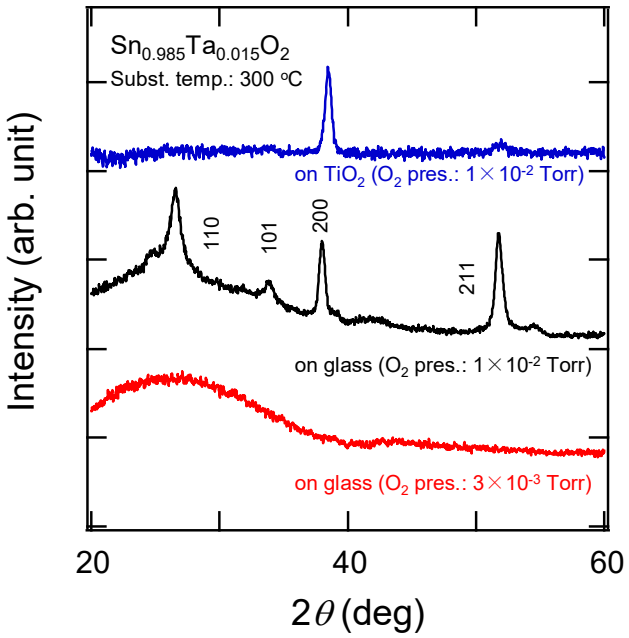

Fig. 6.5. XRD patterns of $Sn_{0.985}Ta_{0.015}O_2$ films deposited at 300 °C.

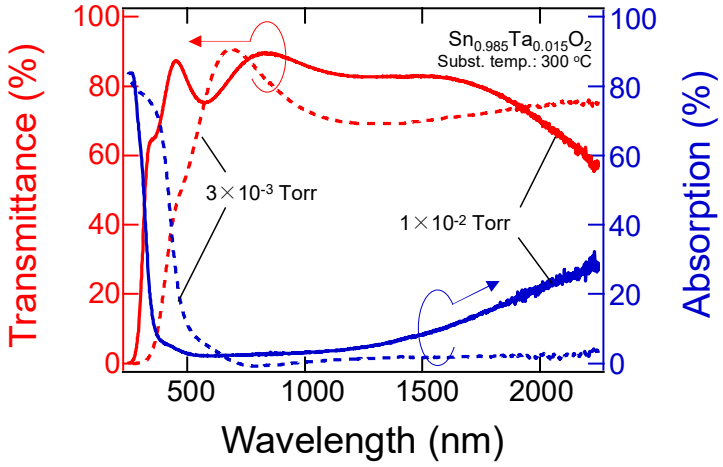

Fig. 6.6. Transmittance and absorption spectra of $Sn_{0.985}Ta_{0.015}O_2$ films on glass deposited at substrate temperature of 300 °C and oxygen partial pressures of 3×10^{-3} Torr (dotted lines) and 1×10^{-2} Torr (solid lines).

amorphization and (101)-preferred growth, resulting in the epitaxial growth on the seed layer and thus improved transport properties. Although substrate temperature of 300 °C is still too high to deposit on ordinary plastic substrates, deposition on polyimide and soda-lime glass substrates is possible at the temperature. These findings would eventually pave the way for future PVCs with low cost and/or weight.

6.4 Summary

I investigated how the growth parameters such as oxygen partial pressure and substrate temperature affect structure and transport properties of TTO films in detail. (101)-preferred growth, which probably originated from energetically stable nature of oxygen deficient (101) plane, was observed for TTO films on glass grown under oxygen poor ambient. The preferred growth gradually changed from (101) to (110) with the increase of oxygen partial pressure, probably due to lowest surface energy of stoichiometric (110) plane. TTO films grown under oxygen rich ambient showed reduced n_e, suggesting carrier compensation in the film due to excess oxygen. On the other hand, TTO films grown under oxygen poor ambient showed no decrease in n_e but drastic decrease in μ_H. As substrate temperature decreased, TTO films both with and without anatase TiO_2 seed layers showed gradual and rapid decrease in n_e and μ_H, respectively. At low substrate temperatures, amorphization and (101)-preferred growth of TTO competed with epitaxial growth on the seed layer. Introducing sufficient process oxygen suppressed such unwanted film growth,

resulting in the epitaxial growth of the TTO films on the seed layer and thus improved transport properties.

Chapter 7 Transport Properties of W-Doped SnO_2 Films: Possible Enhanced Mobility*

In this chapter, transport properties of SnO_2 films doped with various elements such as Sb, Nb, Mo, and W were compared with those of undoped SnO_2 and TTO films. W-doped SnO_2 (WTO) films exhibited high values in both n_e and μ_H comparable with TTO films whereas Sb-, Nb-, and Mo-doped SnO_2 films showed rather poor transport properties. Optimized WTO films grown on anatase TiO_2 seed layers exhibited μ_H of 84 $cm^2V^{-1}s^{-1}$ at $n_e = 2.1 \times 10^{20}$ cm^{-3}. The μ_H value was slightly higher than those for TTO films, and was obtained at reduced n_e compared with the TTO films. Furthermore, the WTO films on bare glass substrates showed moderately high μ_H exceeding 50 $cm^2V^{-1}s^{-1}$ even without the seed layers. These results suggest that W-doping might improve μ_H of SnO_2 possibly due to passivation of dangling bonds at grain boundaries via partial segregation.

7.1 Introduction

In the previous chapters, Ta was used as the dopant for SnO_2 to obtain appropriate n_e without deteriorating crystallinity due to excessive oxygen vacancies. In this chapter, I

* A version of this chapter has been published in Phys. Status Solidi C 8, 543 (2011).

explored several elements for a potential dopant that enhances not only n_e but also μ_H, as demonstrated in In_2O_3-based TCOs (Table 1.2).

To date, F, Sb, and Ta have been extensively investigated as the dopants for SnO_2 whereas other elements have been rather poorly studied. Halogen elements such as Cl, Br, and iodine have been regarded as dopants with lower doping efficiency than F [103, 104]. Pnictogens (Group 15 elements) such as N, P, As, Bi have been sometimes investigated because Sb is one of the most well-known dopants for SnO_2. A few studies clearly showed carrier generation in SnO_2 by P- [105, 106] and As-doping [97] whereas neither N nor Bi has been regarded as dopants at present. H and Li at interstitial sites are sometimes supposed to act as potential dopants for oxides. To date, however, the site of H [107] and Li in SnO_2 lattice has been controversial. A group 5 element, Nb, and group 6 elements, Mo and W, are potential candidates owing to close ionic radius to Ta^{5+} and Sn^{4+} [108]. Unlike Ta exhibiting very high doping efficiency, no studies on Nb-doped SnO_2 have reported such high doping efficiency (see introduction of appendix B). Effect of Mo-doping on SnO_2 has been controversial; a study on Mo-doped SnO_2 by reactive evaporation [109] reported high n_e for the films whereas sputtered Mo-doped SnO_2 showed identical transport properties to those for undoped SnO_2 [110]. In contrast to Nb and Mo, low ρ and high n_e have been found in W-doped SnO_2 (WTO) [111, 112, 113, 114, 115, 116]. However, none of these studies focused on possible enhancement in μ_H.

In this chapter, I explored various dopants other than Ta for higher μ_H: Sb, Nb, Mo, W, and Bi. However, preliminary experiments on Bi-doped SnO_2 revealed that increase in ρ and coloration of the films, suggesting that Bi exited as Bi^{3+} rather than Bi^{5+} [117].

Therefore, I focused on Sb, Nb, Mo, and W. Transport properties of SnO_2 films doped with these elements grown on various substrates were investigated in the former part of this chapter. I found that the transport properties of WTO comparable with TTO. Then, WTO films grown on anatase TiO_2 seed layer were optimized in the later part of this chapter, resulting in high μ_H exceeding 80 $cm^2V^{-1}s^{-1}$ with reduced n_e.

7.2 Experimental

SnO_2 films doped with 1 at% Sb, Nb, Mo, and W were deposited by PLD with a repetition rate of 2 Hz at an oxygen partial pressure of 3×10^{-3} Torr and a substrate temperature of 600 °C. To suppress possible sublimation of dopants, $Sn_{0.99}Mo_{0.01}O_2$ and $Sn_{0.99}W_{0.01}O_2$ targets were sintered at 500 °C and 850 °C, respectively. A target of $Sn_{0.99}Sb_{0.01}O_2$ was purchased from Toshima MFG. Substrates for the film growth were bare glass, Al_2O_3 (0001), and glass covered with rutile and anatase TiO_2 seed layers. The preparation method for the seed layers were described in chapters 4 and 5. The thickness of the SnO_2 films was 135 ± 25 nm.

$Sn_{1-y}W_yO_2$ (WTO) films with y = 0.003~0.05 were deposited on glass with and without anatase TiO_2 seed layers by PLD with a repetition rate of 2 Hz at an oxygen partial pressure of 1×10^{-2} Torr and a substrate temperature of 600 °C. The typical thickness of the WTO films was 200 nm. Thicker films with R_s below 10 $\Omega sq.^{-1}$ were used for optical measurements.

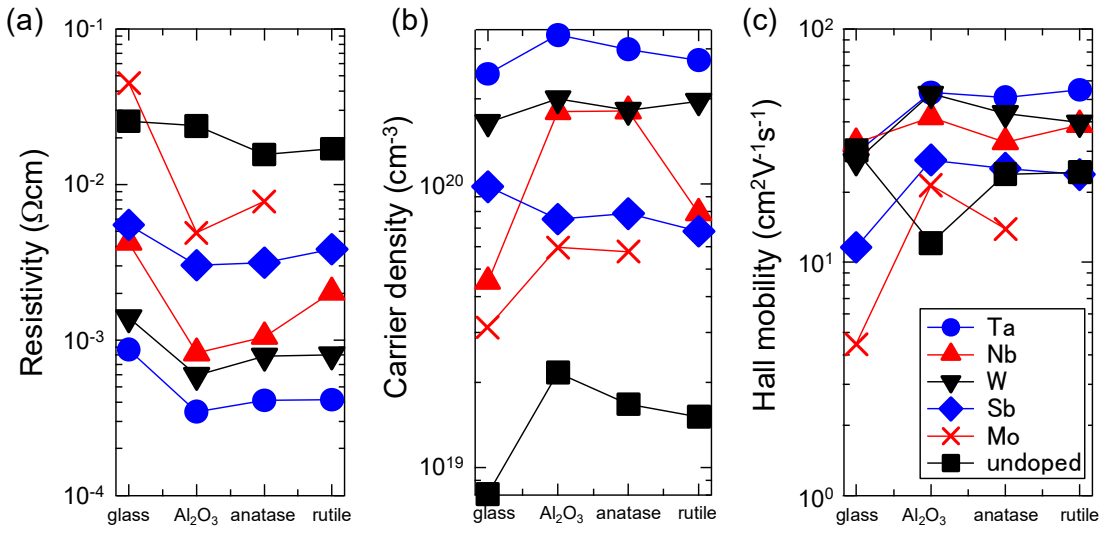

Fig. 7.1. (a) ρ, (b) n_e, and (c) μ_H of undoped SnO_2 (squares) and SnO_2 doped wit Ta (circles), Nb (triangles), W (inverted triangles), Sb (diamonds), and Mo (crosses) on various substrates. Al_2O_3 denotes Al_2O_3 (0001) single crystalline substrate whereas anatase and rutile denote glass substrates covered with 10-nm-thick anatase and rutile TiO_2 seed layers, respectively. Solid lines are guides to eyes.

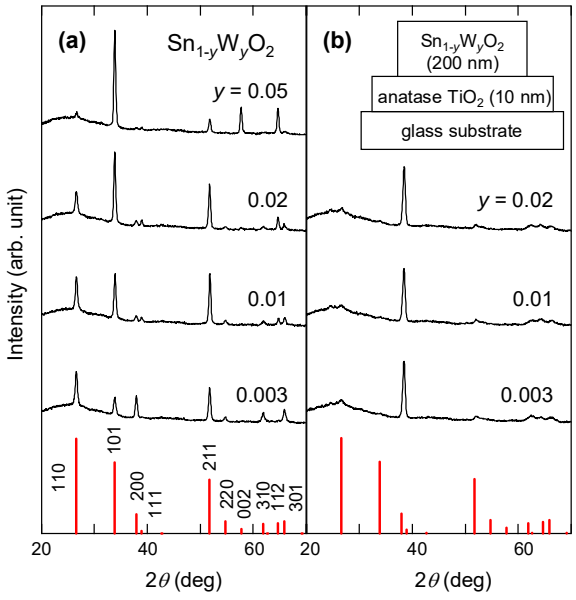

Fig. 7.2. XRD patterns of WTO films on (a) bare glass and (b) glass covered with anatase TiO_2 seed layers. The bar charts show the XRD pattern of bulk SnO_2 (JCPDS 41-1445). The inset of (b) shows a schematic drawing of the film structure.

7.3 Results and Discussion

(1) Comparison of Sb-, Nb-, Mo-, and W-Doped SnO_2 with Undoped and Ta-Doped SnO_2

Structures of the SnO_2 films doped with 1 at% Sb, Nb, Mo, and W were mainly determined by substrates and rather insensitive to dopant species in a similar manner to chapters 3, 4, and 5. The films on bare glass, Al_2O_3 (0001), and glass covered with rutile and anatase TiO_2 seed layers were polycrystalline, (100)-epitaxial, (110)-preferred, and (100)-preferred films, respectively. Figure 7.1 shows a comparison of transport properties of the films with undoped SnO_2 and TTO. As shown in Fig. 7.1(b), the n_e values of these films were higher than those for undoped SnO_2 films (1~2 × 10^{19} cm^{-3}), demonstrating that doped elements more or less released electrons. W-doped films exhibited rather high n_e of approximately 2 × 10^{20} cm^{-3} together with high μ_H comparable with TTO. Thus, detailed transport properties of W-doped films were investigated further and were presented later in this chapter. Interestingly, n_e values for Nb-doped films showed strong dependence on substrates, which is discussed in appendix B. Contrary to the previous study [54] on Sb-doped epitaxial films, in which 100% doping efficiency and high n_e up to 3 × 10^{20} cm^{-3} were reported, Sb-doped films were characterized by rather low n_e less than 1 × 10^{20} cm^{-3}. Because actual Sb concentrations in the films are unknown, possible reduced Sb concentration due to re-evaporation might well result in the low n_e values of the Sb-doped films. Mo-doped films were apparently unpromising due to low values in both n_e and μ_H.

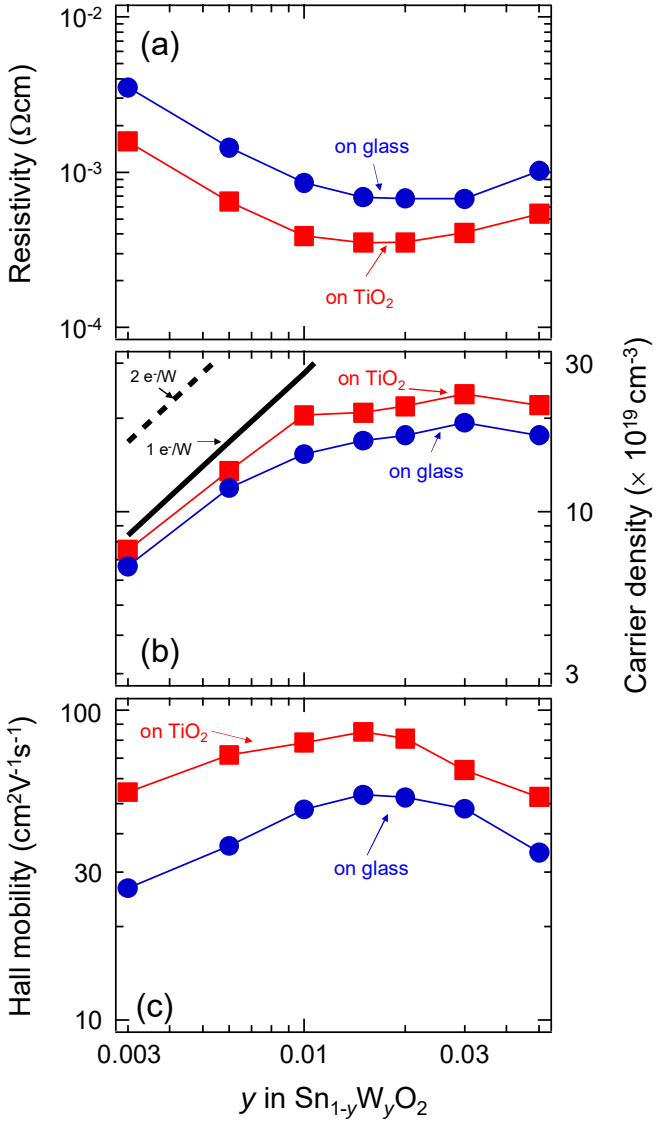

Fig. 7.3. (a) ρ, (b) n_e, and (c) μ_H of WTO films on glass (circles) and anatase TiO_2 seed layers (squares) as a function of W content, y, in $Sn_{1-y}W_yO_2$. The thick solid and dashed lines in (b) represent estimated n_e values assuming that each doped W in nominal concentration released one and two electrons, respectively.

These results demonstrate that W is a promising dopant comparable with Ta whereas Nb, Sb, and Mo are undesirable ones.

(2) Detailed Transport Properties of W-Doped SnO_2 Films

Next, I present results on WTO films with various W concentrations, y. Figure 7.2 compares the XRD patterns of the WTO thin films deposited on glass substrates with and without anatase TiO_2 seed layers (hereafter in this chapter shortly referred to as the seed layer), respectively. As seen in Fig. 7.2(a), the WTO films without the seed layers had the polycrystalline form with random grain orientations. It is also noticeable that the intensity of the 101 diffraction peak monotonically increased with increasing y. In contrast, the WTO films on the seed layers exhibited a preferred (200) orientation irrespective of y, demonstrating the epitaxial growth on the seed layer. A similar crystallographic behavior depending on the seed layer has been observed in TTO films in chapter 5.

Figure 7.3 shows the room-temperature transport properties of the WTO films. The minimum value of ρ in the WTO films on glass was approximately 7×10^{-4} Ωcm at around $y = 0.02$, which is very close to the value reported for WTO films grown using pulsed plasma deposition [113, 114]. The value of ρ was decreased further, down to 3.5×10^{-4} Ωcm ($y = 0.015$), by using the seed layer. It should be noted that this value is lower than those for Sb-doped [73] and F-doped [74] SnO_2 grown by PLD. In the lightly doped region with $y < 0.01$, the n_e value of the WTO films on the seed layers was almost proportional to y, as shown in Fig. 7.3 (b). Meanwhile, for $y > 0.01$, n_e tended to shift downward from the linear n_e-y relation, and reached the maximum, 2.4×10^{20} cm^{-3}, at $y =$

0.03. The n_e values of the WTO films on glass were approximately 20% lower than those of the WTO films on the seed layers over the entire y region. Unlike TTO, the n_e values for the WTO films were lower than the expected n_e values assuming that each doped W in nominal concentration released one or two electrons. This indicates that doping efficiency of W were inferior to that of Ta. As shown in Fig. 7.3(c), the μ_H values of the WTO films on the seed layers were much larger than those of the WTO films on glass, and the maximum μ_H of 84 $cm^2V^{-1}s^{-1}$ ($n_e = 2.1 \times 10^{20}$ cm^{-3}, $\rho = 3.5 \times 10^{-4}$ Ωcm) was obtained at y = 0.015. This μ_H value was slightly higher than those for TTO films (chapter 5), and was, more importantly, obtained at reduced n_e compared with the TTO films. The enhancement of μ_H was more prominent in the lightly doped region, where grain boundary scattering dominated μ_H.

Next, I compared the transport properties of the WTO films with those of TTO films in detail, as shown in Fig. 7.4. The transport properties of the WTO films on the seed layer were rather comparable with those of the TTO films grown on the seed layers. However, a remarkable difference is seen in n_e; the maximum value of n_e for the TTO films on the seed layers was 6.8×10^{20} cm^{-3}, which is noticeably larger than that of the WTO films on the seed layers, 2.4×10^{20} cm^{-3}. In contrast, the maximum μ_H values for the WTO and the TTO films on the seed layers were almost equivalent and exceeded 80 $cm^2V^{-1}s^{-1}$. This is because the μ_H values were mainly determined by structural parameters such as the grain size and orientation, which were strongly influenced by the seed layers. Here, it should be noted that the WTO films on glass showed much higher μ_H than the TTO films on glass at $n_e > 1 \times 10^{20}$ cm^{-3}; some WTO films exhibited μ_H exceeding 50 $cm^2V^{-1}s^{-1}$

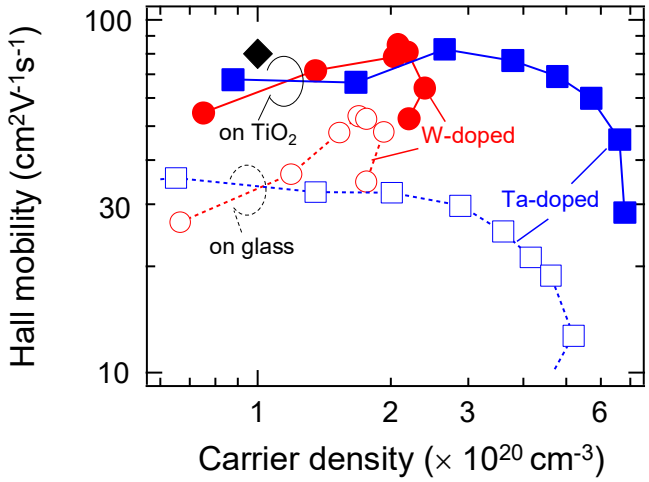

Fig. 7.4. Comparison of n_e and μ_H values for WTO (circles) and TTO (squares) films on glass (open symbols) and anatase TiO_2 seed layers (squares) with the target value in this study (diamond).

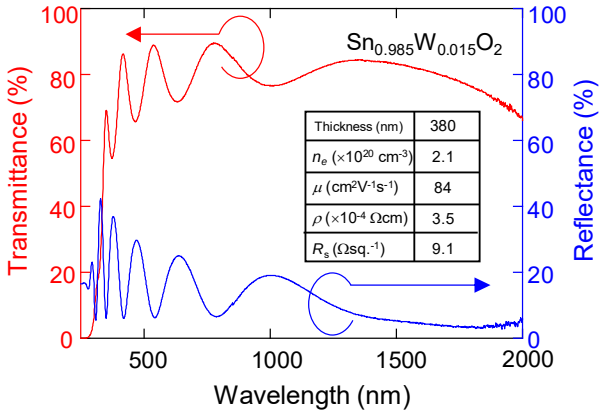

Fig. 7.5. Transmittance and reflectance spectra of a WTO with $y = 0.015$ on the anatase TiO_2 seed layer. Inset shows transport properties of the WTO film.

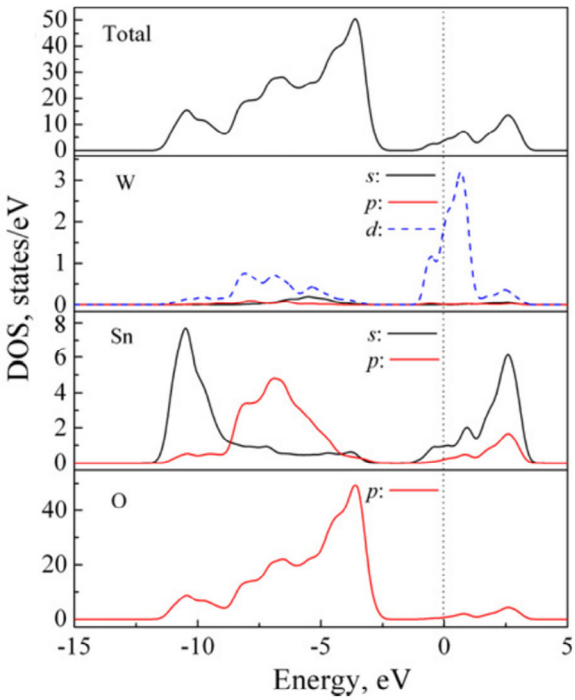

Fig. 7.6. Theoretically calculated partial density of states of W-doped SnO_2. [118] (Copyright (2012) Elsevier)

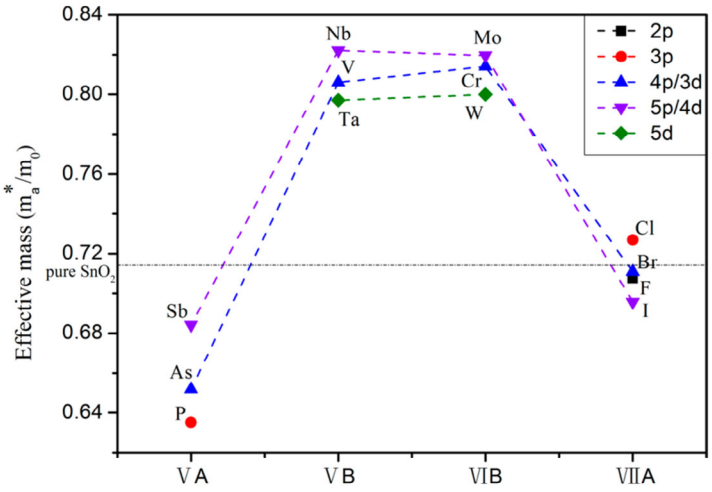

Fig. 7.7. Theoretically calculated values of effective mass for SnO_2 doped with various elements. [119] (Copyright (2014) American Chemical Society)

whereas even thick TTO films (Fig. 5.5) showed μ_H below 50 $cm^2V^{-1}s^{-1}$. This result suggests that W-doping might improve μ_H of SnO_2.

Figure 7.5 shows the transmittance and reflectance spectra of a WTO film with y = 0.015 on the seed layer. The R_s value of the film was 9.1 $\Omega sq.^{-1}$, as shown in the inset of Fig. 7.5. Obviously, the WTO film exhibited high transparency in both the visible and NIR regions due to the low n_e and high μ_H. A transmittance greater than 70% was obtained in the wavelength region of 400~1950 nm, which is wider than those obtained for the TTO films (chapter 5) owing to the reduced n_e of the WTO film.

Thus far, W-doping effects on SnO_2 were theoretically studied using first principles calculations [118, 119]. As shown in Fig. 7.6 [118], partial density of states around fermi energy was formed by W-doping, being consistent with the experimentally observed systematic carrier generations in WTO. On the other hand, possible enhanced μ_H is not straightforward; calculated effective mass in WTO was slightly larger than those in TTO and FTO [119], as shown in Fig. 7.7. I speculate that segregated W at grain boundaries, which was consistent with reduced doping efficiency, might result in passivation of dangling bonds and thus reduced barrier height at the grain boundaries. Unfortunately, such effects are difficult to demonstrate neither experimentally nor theoretically.

7.4 Summary

Structures and transport properties of the SnO_2 films doped with 1 at% Sb, Nb, Mo, and W were investigated. The film structures were mainly determined by substrates and

rather insensitive to dopant species. The WTO films exhibited high values in both n_e and μ_H comparable with TTO films whereas the Sb-, Nb-, and Mo-doped SnO_2 films showed rather poor transport properties.

Transport properties of WTO films with various y were investigated in detail. Optimized WTO films with $y = 0.015$ grown on anatase TiO_2 seed layers exhibited $\mu_H = 84$ $cm^2V^{-1}s^{-1}$ ($n_e = 2.1 \times 10^{20}$ cm^{-3}, $\rho = 3.5 \times 10^{-4}$ Ωcm). This μ_H value was slightly higher than those for the TTO films, and was obtained at reduced n_e compared with the TTO films. Unlike TTO, the n_e values for the WTO films were lower than the expected n_e values assuming that each doped W in nominal concentration released one or two electrons. In addition, the maximum value of n_e for the WTO films on the seed layers was 2.4×10^{20} cm^{-3}, which is noticeably lower than that of the TTO films on the seed layers, 6.8×10^{20} cm^{-3}. These results indicate that doping efficiency of W were inferior to that of Ta. Interestingly, WTO films on bare glass without the seed layers exhibited μ_H exceeding 50 $cm^2V^{-1}s^{-1}$, which is significantly higher than those for TTO films on glass. These results suggest that W-doping might improve μ_H of SnO_2 possibly due to passivation of dangling bonds at grain boundaries via partial segregation. The WTO film with $y = 0.015$ exhibited an optical transmittance of over 70% at wavelengths ranging from 400 to 1950 nm, which is wider than those obtained for the TTO films owing to the reduced n_e of the WTO film.

Chapter 8 High Mobility Exceeding 130 $cm^2V^{-1}s^{-1}$ in W-doped SnO_2 Thin Films on Glass Using Seed Layers of Rutile $(Ti,Nb)O_2$ Solid Solution

I investigated the structural and transport properties of WTO films grown on seed-layers that were lattice-matched to SnO_2 along the a-axis. Rutile $(Ti,Nb)O_2$ solid solutions were used as the seed layer with systematically controlled a-axis length. WTO films grown on TNO with z = 0.45 and 0.5 showed (001)-preferred growth which was most likely realized by epitaxially stabilized (001) nuclei via a nearly perfect lattice-match in the a-axis of TNO to SnO_2. The WTO films with the (001)-preferred growth exhibited an overwhelmingly high μ_H value of 136 $cm^2V^{-1}s^{-1}$ at $n_e = 1.4 \times 10^{20}$ cm^{-3}. As a consequence of this very high μ_H with reduced n_e, the WTO films with low R_s values of approximately 10 $\Omega sq.^{-1}$ exhibited a low absorption of 3.5% at the wavelength of 1400 nm. These properties sufficiently meet the requirement for the electrode of the next-generation full-spectrum PVCs.

8.1 Introduction

In the previous chapters, I have explored various dopants and seed layers to enhance the μ_H value of SnO_2. The best result, μ_H = 84 $cm^2V^{-1}s^{-1}$ at n_e = 2.1 × 10^{20} cm^{-3}, was obtained for W-doped SnO_2 films on anatase TiO_2 seed layers. Although the μ_H value exceeded the milestone of this study (80 $cm^2V^{-1}s^{-1}$), a further decrease in n_e to 1 × 10^{20} cm^{-3} is necessary.

Historically, material exploration has advanced from simple elements to compounds with more and more complicated compositions, sometimes involving dramatically improved properties. A good example is the transition temperature of superconductivity [120]. Pure elements such as Nb and Pb show superconductivity at several K. Binary compounds such as Nb_3Ge and MgB_2 exhibit transition temperatures on the order of 10 K. Superconductivity above 100 K at ambient pressure is only obtained for cuprates like $Bi_2Sr_2Ca_2Cu_3O_{10}$ with very complicated compositions and structures. Thus, one possible way to achieve higher μ_H for SnO_2 films is through exploration in more complicated systems, such as co-substitution as doping and ternary oxides as seed layers.

In this study, I focused on ternary oxides. More specifically, I focused on solid solutions of binary rutile oxides as the seed layer for SnO_2. It is well-known that some pairs of rutile oxides form wide ranges of, or perfect, solid solutions [121]. Rutile TiO_2 and NbO_2, which were separately examined for the use of the seed layer of SnO_2 in chapter 4, is the pair that forms a perfect solid solution [122]. Figure 8.1 shows lattice parameter data for rutile $Ti_{1-z}Nb_zO_2$ (TNO) [122] together with SnO_2, obtained from literature. Clearly, the a-

axis length of TNO increases linearly as Nb concentration (z) increases, demonstrating that TNO follows Vegard's law and is thus a perfect solid solution. Here, it should be stressed that the a-axis length of SnO_2 is longer and shorter than those of TiO_2 and NbO_2, respectively. Therefore, solid solutions of TiO_2 and NbO_2 are expected to show better lattice matching to SnO_2 along the a-axis than unalloyed TiO_2 and NbO_2. Even perfect lattice matching to SnO_2 along the a-axis might be achieved by using TNO with $z \sim 0.6$, as shown in the inset of Fig. 8.1(a). Unlike the a-axis length, the c-axis length of TNO shows a deviation from Vegard's law. The c-axis length of TNO always yields larger than expected values from Vegard's law, and shows the maximum value of 0.300 nm at $z \sim 0.5$. These behaviors are probably related to the structural order in NbO_2: dimerized Nb atoms along the c-axis. Because the order is destroyed by Ti substitution [122], the c-axis length of TNO is probably explained by a convolution of Vegard's law and the disorder in dimerization along the c-axis. The c-axis length of TNO is always smaller than that of SnO_2. However, the mismatch between SnO_2 and TNO is relatively small, around $z \sim 0.6$, at which perfect lattice matching along the a-axis is expected.

In this chapter, I investigated the structural and transport properties of WTO films grown on seed layers of TNO with various z. The WTO films grown on TNO with $z = 0.45$ showed (001)-preferred growth, which was most likely achieved by epitaxially stabilized (001) nuclei due to a-axis lattice matched TNO. Furthermore, the WTO film exhibited an overwhelmingly high μ_H value of 136 $cm^2V^{-1}s^{-1}$ at $n_e = 1.4 \times 10^{20}$ cm^{-3}, which is 70% higher than the target value of 80 $cm^2V^{-1}s^{-1}$.

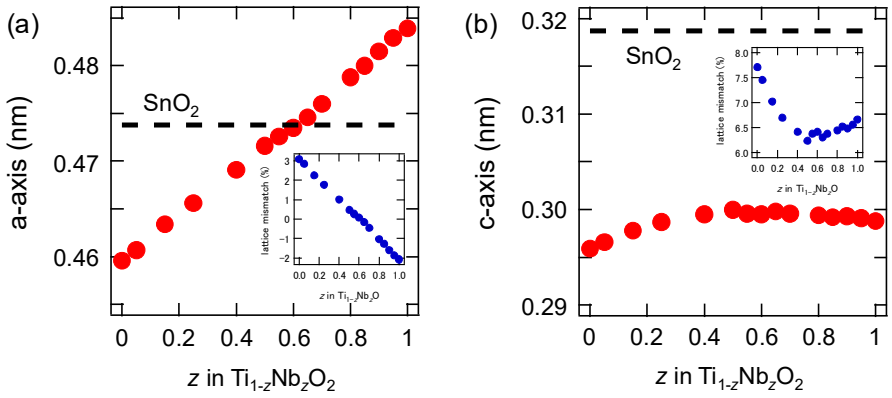

Fig. 8.1. Comparison of (a) a-axis and (b) c-axis length for rutile $Ti_{1-z}Nb_zO_2$ (TNO) solid solutions (circles) and SnO_2 (broken lines). Insets show corresponding lattice mismatch of SnO_2 to TNO. The data for TNO and SnO_2 are taken from ref 120 and JCPDS 41-1445, respectively.

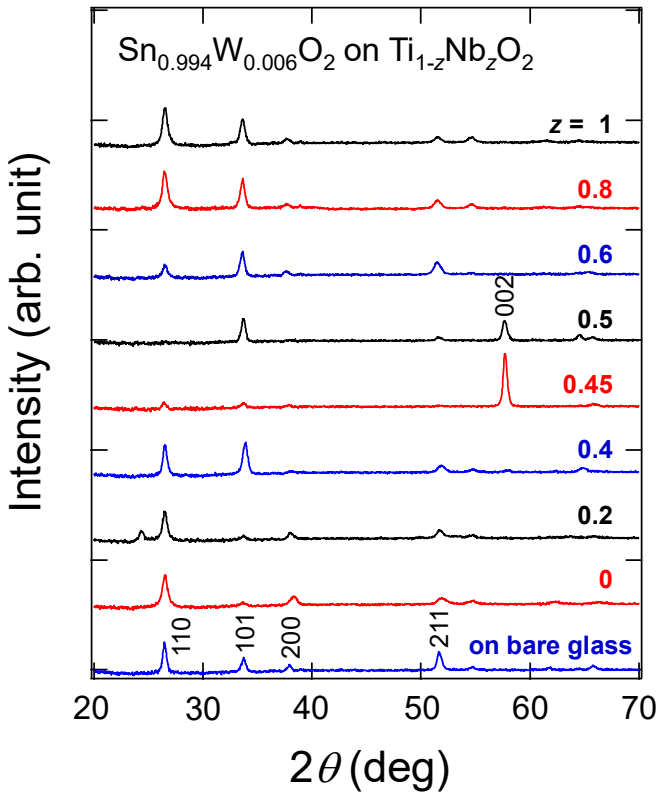

Fig. 8.2. XRD patterns of $Sn_{0.994}W_{0.06}O_2$ films on $Ti_{1-z}Nb_zO_2$ (TNO) solid solution seed layers.

8.2 Experimental

Ten nm thick amorphous precursor films for TNO solid solution seed layers were deposited on unheated alkaline-free glass substrates by PLD at a repetition rate of 5 Hz. Sintered pellets of $Ti_{1-z}Nb_zO_{2+z/2}$ were used as PLD targets. No oxygen was introduced for the deposition of TNO with $z \geq 0.6$, whereas a small amount of oxygen with a partial pressure of 3×10^{-6} Torr was introduced for the deposition of TNO with $z \leq 0.5$. The amorphous precursor films for the seed layers were then annealed at 600 °C in the PLD chamber to produce TNO with various z values. WTO with $y = 0.06$ ($Sn_{0.994}W_{0.006}O_2$) films were subsequently grown on the TNO seed layers at an oxygen partial pressure of 5×10^{-3} Torr and a substrate temperature of 600 °C. The typical thickness of the WTO films was 135 ± 15 nm. Thicker films with R_s below 10 $\Omega sq.^{-1}$ were used for optical measurements.

8.3 Results and Discussion

Figure 8.2 shows the XRD patterns of the WTO films grown on the TNO seed layers with various z values. The WTO films on unalloyed TNO, TiO_2 and NbO_2, showed XRD patterns consistent with those presented in the previous chapters. The WTO films on moderately alloyed TNO showed XRD patterns similar to those for the WTO films on the unalloyed TNO. In contrast, the WTO films grown on heavily alloyed TNO with $z = 0.45$ and 0.5 showed a characteristic feature: (001)-preferred growth. Figure 8.3 shows cross sectional TEM images of the WTO film on the TNO with $z = 0.45$.

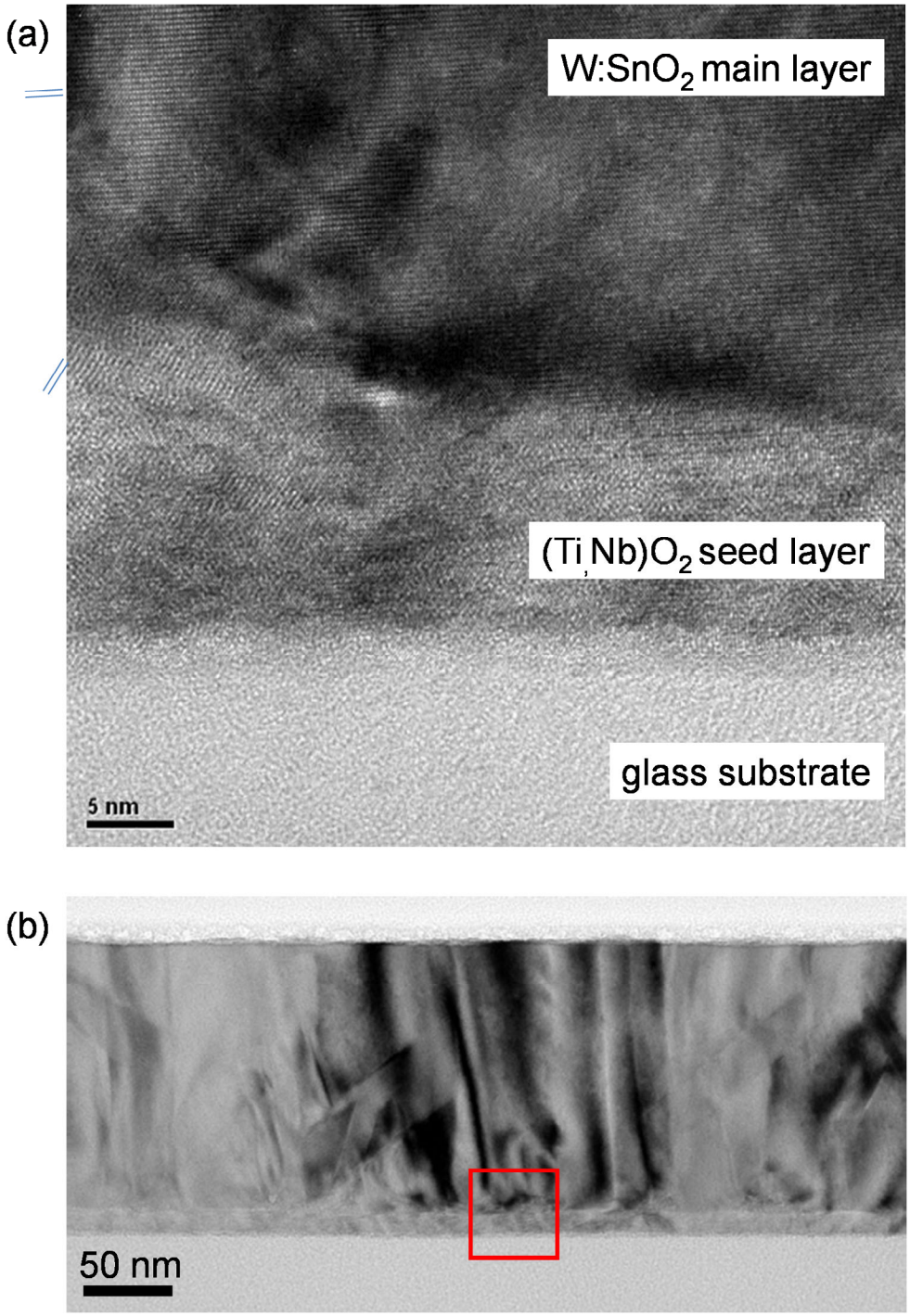

Fig. 8.3. (a) High magnification and (b) wide field of view cross-sectional TEM images of the $Sn_{0.994}W_{0.006}O_2$ film on $Ti_{0.55}Nb_{0.45}O_2$. Image (a) was taken at the location shown as the square in (b). Parallel lines with spacing of 0.32 nm in (a) are guides to eyes.

The lattice fringes parallel to the substrates in the major domain of the WTO layer showed interplanar spacing of 0.32 nm, which is in good agreement with c-axis length of SnO_2. Although minor WTO domains with other orientations were observed near the WTO/TNO interface, competing (001)-oriented major domains took over the minor domains in the early growth stage. These TEM observations are consistent with the XRD pattern for the WTO film. As discussed in Chapter 6, preferred growth with various low index surfaces such as (110), (101), (100), and (211) have been reportedly observed for SnO_2 films even without epitaxial stabilization. However, to my knowledge, (001)-preferred growth of SnO_2 films has never been reported. This is most likely because the (001) plane is the most energetically unstable among various low-index surfaces of SnO_2 [98], and thus the nucleation of the (001) planes is nearly impossible on amorphous substrates. I infer that perfect lattice matching of the a-axis of the heavily alloyed TNO seed layers might stabilize the (001)-nuclei of SnO_2. On the other hand, nucleation with other orientations is supposedly unfavorable, because of the large lattice mismatch between the c-axis of TNO and SnO_2.

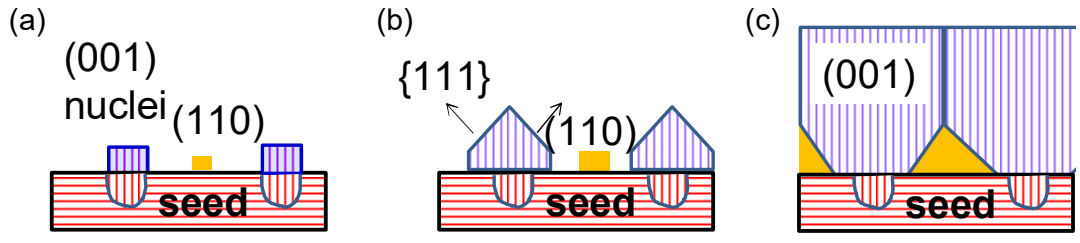

Fig. 8.4. Model for (001) oriented growth of SnO_2 on TNO seed layer. (a) Epitaxial stabilization of (001) nuclei owing to perfect a-axis lattice matching. (b) High speed growth of {111} faces. (c) Dominant growth of (001)-oriented SnO_2.

The (001) nuclei of SnO_2 probably covered the surface of the seed layers partially due to polycrystalline nature of the seed layers. Nevertheless, the optimized WTO films exhibited dominant (001) growth as seen in the XRD and TEM measurements. The mechanism behind the (001) growth of the WTO films can be explained as follows (Fig. 8.4). Lateral growth of (001) plane is unlikely due to energetically unstable nature of the plane. Thus, another growth mode should be considered. High speed growth along [001] via highly reactive {111} faces was observed for bulk single crystals of SnO_2 grown under oxygen deficient conditions [123]. If this growth mode is realized in the present study, high speed diagonal growth via {111} faces on the (001) nuclei will take over growth from nuclei with other orientations. This model is consistent with the TEM observations.

The most prominent (001)-preferred growth was observed at $z = 0.45$, which is lower than the expected $z \sim 0.6$, based on the room temperature literature data (Fig. 8.1). This discrepancy could be explained by a few reasons: compositional deviation from nominal values, difference in coefficients of thermal expansion, and lattice expansion due to oxygen off-stoichiometry. Although I performed no compositional analysis for the TNO, Furubayashi et al. observed significant compositional deviation in anatase Nb-doped TiO_2 epitaxial films grown by PLD. The analyzed composition ($Ti_{0.64}Nb_{0.36}O_2$) was Nb-rich compared to the nominal value ($Ti_{0.7}Nb_{0.3}O_2$) [15]. Thus, the actual value for nominal $z = 0.45$ might be close to $z = 0.6$. Estimating the contribution of the difference in the coefficients of thermal expansion is difficult because the values for the alloyed TNO are unknown. The coefficients of thermal expansion along the a-axis for SnO_2, TiO_2, and NbO_2 are reportedly 4.0×10^{-6}, 8.5×10^{-6} [124], and 2.5×10^{-6} $°C^{-1}$ [125], respectively. On the basis of these values, the calculated coefficient of thermal expansion along the a-axis for

TNO with z = 0.45, assuming linear interpolation [126], is 5.8×10^{-6} °C $^{-1}$. Thus, the difference in thermal expansion at the growth temperature (600 °C) compensates for the 0.0005 nm (0.1%) lattice mismatch, which corresponds to a difference of 0.02 in *z*. These estimations indicate that the difference in the thermal expansion, albeit unignorable, cannot explain the lattice matching of TNO with z = 0.45 to SnO_2 alone. Consequently, I speculate that the lattice expansion of TNO owing to oxygen off-stoichiometry plays a major role in the lattice matching of TNO with z = 0.45 to SnO_2.

Next, I discuss the transport properties of the WTO films. Figure 8.5 shows the room temperature transport properties of the WTO films grown on TNO with various *z* values. For comparison, the transport properties for a WTO film grown on bare glass are plotted as the broken lines. As shown in Fig. 8.5(b), the WTO films on TNO showed n_e values of 1.19–1.51 $\times 10^{20}$ cm^{-3}, which were almost identical to that for the WTO film on bare glass, 1.24×10^{20} cm^{-3}. A slightly decreasing tendency in n_e with the increase in *z* might be explained by effects of epitaxial strain on carrier generation, similar to those observed in Nb-doped SnO_2 (see appendix B). The increase in n_e around z = 0.4–0.5 might indicate termination of planar defects inside the films, which will be discussed in detail later in this chapter.

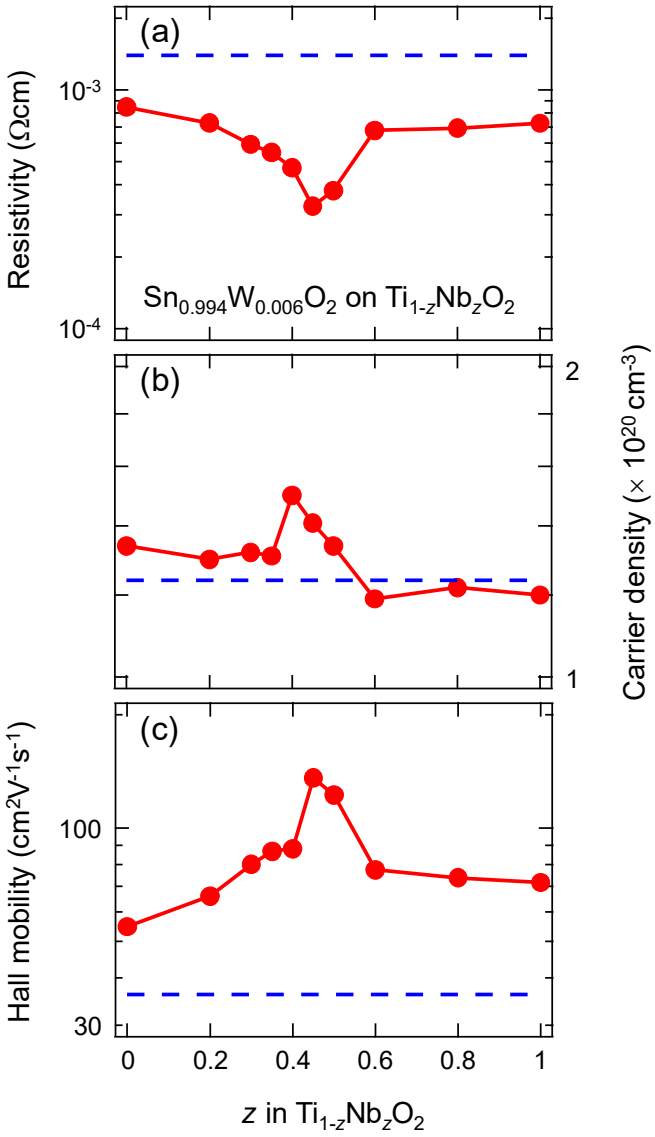

Fig. 8.5. Room temperature (a) ρ, (b) n_e, and (c) μ_H of the $Sn_{0.994}W_{0.006}O_2$ films grown on $Ti_{1-z}Nb_zO_2$ seed layers with various z. The broken lines represent the transport properties of the $Sn_{0.994}W_{0.006}O_2$ film grown on bare glass substrate.

Surprisingly, the WTO films with (001)-oriented growth exhibited dramatically enhanced μ_H. As shown in Fig. 8.5(c), the WTO films on the TiO_2 and NbO_2 seed layers showed μ_H values of 55 and 72 $cm^2V^{-1}s^{-1}$, respectively, which were higher than that for the WTO film on bare glass, 37 $cm^2V^{-1}s^{-1}$. As the alloying of the TNO seed layers proceeded, the WTO films on the alloyed TNO seed layers showed systematically increased μ_H values compared with the WTO films on the unalloyed TNO. In addition to the systematic increase in μ_H, dramatically enhanced μ_H values, which exceeded 100 $cm^2V^{-1}s^{-1}$, were obtained for the WTO films on heavily alloyed TNO with z = 0.45 and 0.5. In particular, the WTO films on TNO with z = 0.45 exhibited overwhelmingly high μ_H values of 136 $cm^2V^{-1}s^{-1}$ with $n_e = 1.4 \times 10^{20}$ cm^{-3}. This μ_H value is the highest among doped and undoped SnO_2 films, including the epitaxial films, as shown in Fig. 8.6. It should be noted that the obtained μ_H value of 136 $cm^2V^{-1}s^{-1}$ is 70% higher than the target μ_H value of 80 $cm^2V^{-1}s^{-1}$. This 70% margin suggests that high μ_H values exceeding 80 $cm^2V^{-1}s^{-1}$ might be achieved for SnO_2 films fabricated even in disadvantageous processes, such as low temperature deposition and sputtering.

In order to obtain insights into the carrier transport mechanism of the WTO film with the highest μ_H value, the temperature dependence of n_e and μ_H for the WTO film was measured, as shown in Fig. 8.7. The n_e for the WTO film was independent of temperature, indicating that the WTO film is a degenerate semiconductor. The temperature dependence of the μ_H value for the WTO film showed a negative coefficient, demonstrating that phonon scattering significantly contributes to μ_H. The μ_H value at low temperatures, where phonon scattering is negligibly small, was 200 $cm^2V^{-1}s^{-1}$. This value is in fair agreement with the

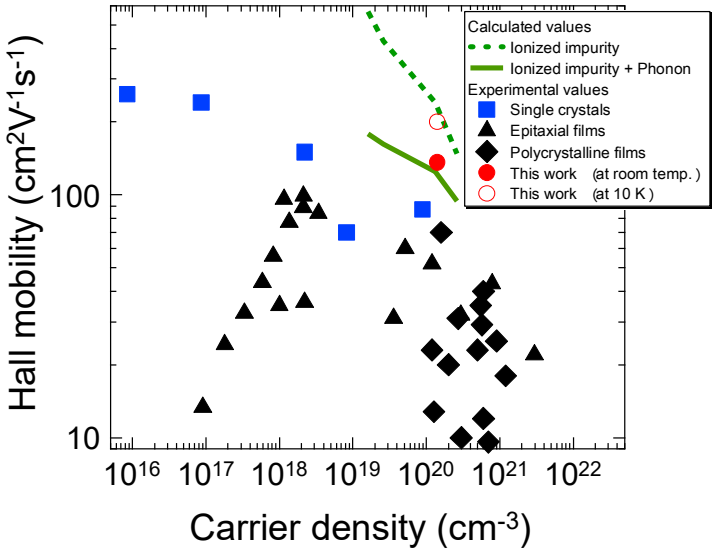

Fig. 8.6. Comparison of the transport properties of the highest μ_H film in this study (circles) with calculated and literature values. The dashed line represents calculated values assuming that only ionized impurity scattering contributes μ_H whereas the solid line represents calculated values taking additional phonon scattering into account (see appendix A). The data for bulk single crystals (squares), epitaxial films (triangles), and polycrystalline films (diamonds) are from [32, 33], [44, 47, 54, 55], and [6], respectively. Solid symbols are data measured at room temperature whereas the open symbol was the datum measured at 10 K (see Fig. 8.7).

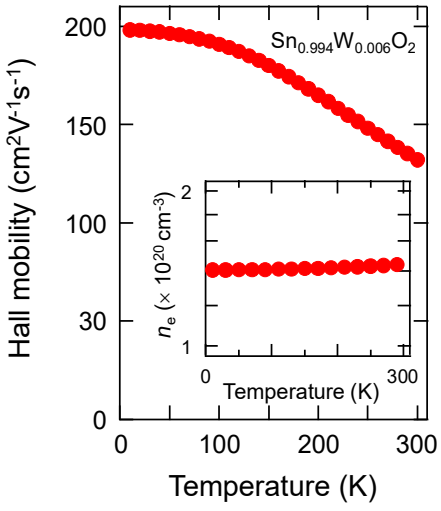

Fig. 8.7. Temperature dependence of μ_H and n_e (inset) for the $Sn_{0.994}W_{0.006}O_2$ film on $Ti_{0.55}Nb_{0.45}O_2$.

intrinsic limit by ionized impurity scattering (see appendix A for calculation), as shown in Fig. 8.6. This result suggests that the carrier transport in the WTO film is mainly dominated by ionized impurity scattering at low temperature. At room temperature, the contribution of phonon scattering should be taken into account. In this study, I employed literature data [32] for bulk single crystals (260 $cm^2V^{-1}s^{-1}$) for simplicity and used Matthiessen's rule to calculate μ_H. Again, the experimental μ_H value at room temperature agrees fairly with the calculated μ_H value, assuming that only phonon and ionized impurity scatterings contribute to μ_H. These results indicate that the carrier transport in the WTO film with the highest μ_H value can be explained by only phonon and ionized impurity scatterings, and thus other factors such as grain boundary scattering are negligible.

At present, it is still unclear why the grain boundary scattering in the WTO films on heavily alloyed TNO is significantly suppressed compared with that on the SnO_2 films in the previous chapters. However, the strong correlation of (001)-oriented growth (Fig.8.2) with the μ_H values (Fig. 8.5(c)) suggests that (001)-oriented growth plays a key role. I speculate that {101} CSPs, which are frequently observed for epitaxial SnO_2 films, act like grain boundaries [49] and dominate transport properties of the SnO_2 films. The {101} CSPs are mainly induced by misfit dislocations near the substrate/film interface, and propagate as film thickness increases. The propagation of {101} CSPs sometimes stops during film growth with oxygen vacancies left at the termination sites. In addition, the crashing of two CSPs into each other can stop the propagation without additional defects [50]. Nevertheless, some of the CSPs survive even near the film surfaces, as observed in (101) and (100) epitaxial SnO_2 films by TEM [49, 50]. Such CSPs should work as a grain boundary [49].

Table 8.1. Dihedral angles between {101} crystallographic shear planes (CSPs) and basal planes of SnO_2 with various orientations.

Orientation	(110)	(101)	(100)	(001)
Dihedral angle (deg.)	66.8	0, 46.5	90, 56.1	33.9

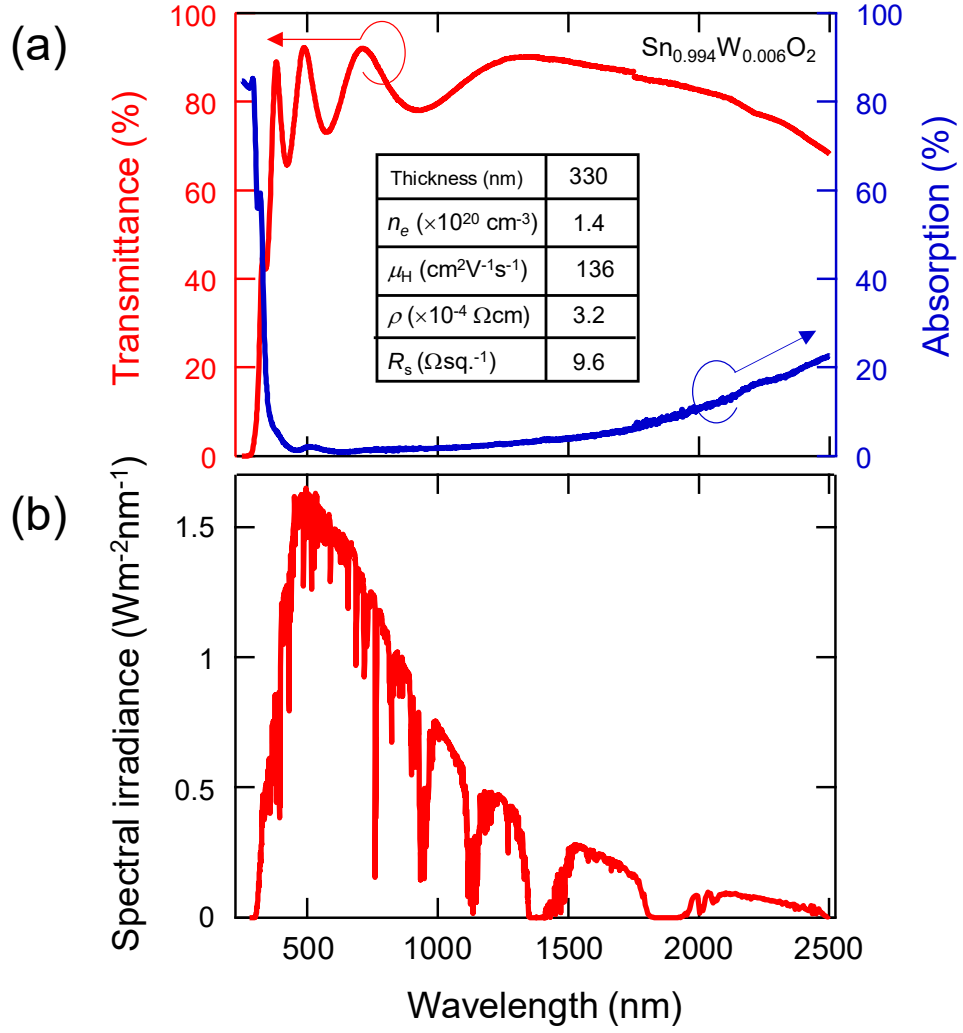

Fig. 8.8. (a) Transmittance and absorption spectra of the $Sn_{0.994}W_{0.006}O_2$ film on $Ti_{0.55}Nb_{0.45}O_2$. Inset shows the transport properties of the film. (b) Standard reference solar spectrum (AM1.5G).

Here, the orientation of the SnO_2 films is highly critical to the propagation of the {101} CSPs. Table 8.1 summarizes the dihedral angles between {101} CSPs and basal planes of SnO_2 with various orientations. Notably, (001)-oriented SnO_2 has the smallest dihedral angle to {101} CSPs among SnO_2 with various orientations. This indicates that (001)-orientation is the most energetically unfavorable for the CSP propagation, and thus most of the CSPs in (001) SnO_2 films might terminate inside the film. I planned direct visualization of {101} CSPs in (001) epitaxial SnO_2 films, and revealed that the CSPs indeed stopped propagation inside the films in the early stage of film growth [127]. A slight increase in n_e at z = 0.4–0.5 might result from oxygen vacancies at the termination sites of the CSPs inside the films. On the basis of the abovementioned discussion, the effect of the TNO composition on of the μ_H value for the WTO films can be explained as follows. The gradual and systematically increased μ_H value associated with the alloying of TNO results from the reduced density of the CSPs, owing to reduced misfit dislocations. The dramatically enhanced μ_H value at z = 0.45 and 0.5 originates from termination of the CSPs induced by the (001)-oriented growth of the WTO films.

Finally, I briefly mentioned optical properties of the WTO films with very high μ_H values. Figure 8.8 shows the transmittance, reflectance, and absorption spectra of the WTO film together with the transport properties. Although slight absorption of a few % due to the TNO seed layer was observed around 500 nm, the absorption would be reduced in films with thinner seed layers. The WTO films with very high μ_H exhibited a very wide transparency window together with sufficiently low R_s, which is suitable for PVC application. The film exhibited a transmittance of over 70% in the range of 365–2455 nm,

which is substantially wider than those obtained for other films investigated in this study. Moreover, the film exhibited absorption of 3.5% at the wavelength of 1,400 nm, which is lower than the target value (5%) in this study. The excellent transparency in NIR region of the WTO film would significantly enhance conversion efficiency of the next-generation full-spectrum PVCs.

8.4 Summary

Using rutile TNO solid solutions as the seed layer, I investigated the effects of lattice matching on the structural and the transport properties of WTO films. WTO films grown on TNO with $z = 0.45$ and 0.5 showed (001)-preferred growth. The preferred growth was probably realized by epitaxially stabilized (001) nuclei via nearly perfect lattice matching in the a-axis of TNO to SnO_2. The WTO films with the (001)-preferred growth exhibited an overwhelmingly high μ_H value of 136 $cm^2V^{-1}s^{-1}$ at $n_e = 1.4 \times 10^{20}$ cm^{-3}. I speculate that the dramatically enhanced μ_H value originates from not only the decreased density of misfit dislocations, but also the (001)-orientation; (001)-oriented growth would more effectively suppress propagation of {101} planar defects than growth in other orientations. The {101} planar defects might well act as grain boundary. As a consequence of very high μ_H with reduced n_e, the WTO films with low R_s values of ~10 $\Omega sq.^{-1}$ exhibited low absorption, 3.5%, at the wavelength of 1400 nm. These properties sufficiently meet the requirement for the electrode of the next-generation full-spectrum PVCs.

Chapter 9 Conclusions

In this study, I have established the guiding principle of materials design for high μ_H SnO_2 films with low n_e for transparency in the full ultraviolet-to-NIR spectrum of sunlight. The guiding principle includes epitaxial growth using seed layers, use of W as a preferred dopant, and lattice parameter engineering using a solid solution. Consequently, I have successfully developed SnO_2-based TCOs that can transmit the full ultraviolet-to-NIR spectrum of sunlight. The optimized films exhibited very low absorption < 5% at a wavelength of 1400 nm, together with low R_s values of ~10 $\Omega sq.^{-1}$, which was realized by an extremely high μ_H value (136 $cm^2V^{-1}s^{-1}$ at n_e of 1×10^{20} cm^{-3}). I believe that these findings would be eventually transferred to industrial deposition methods such as sputtering, which would lead to massive production of TCOs suitable for the next-generation full-spectrum PVCs. In this chapter, I summarize the obtained results and discuss future prospects in applied research and basic science.

9.1 Summary

In this study, I have developed SnO_2-based TCOs that can transmit the full ultraviolet-to-NIR spectrum of sunlight for next-generation PVCs. The transport properties obtained in this study are summarized in Fig. 9.1. The goal of this study was to achieve a μ_H value of 80 $cm^2V^{-1}s^{-1}$ at $n_e = 1 \times 10^{20}$ cm^{-3}, which will yield free carrier absorption less

than 5% at 1400 nm. I first compared the transport properties of randomly oriented polycrystalline TTO films on glass substrates with those of epitaxial TTO films on Al_2O_3 (0001) substrates. The polycrystalline TTO films showed much lower μ_H values of 30–40 $cm^2V^{-1}s^{-1}$ than the epitaxial TTO films, suggesting that high angle grain boundary in the polycrystalline TTO films significantly suppressed the μ_H values.

On the basis of results, I conceived an idea that the use of appropriate seed layers would realize epitaxial growth of SnO_2 on glass substrates and might enhance the μ_H of SnO_2 films. This idea was first tested by using materials isostructural to SnO_2, namely rutile TiO_2 and NbO_2, as the seed layers. Consequently, 10-nm-thick rutile TiO_2 and NbO_2 seed layers on glass substrates were found to promote (110)-preferred growth of TTO. Furthermore, the TTO films grown on the seed layers showed high μ_H values of 66–68 $cm^2V^{-1}s^{-1}$, which is comparable to that of the epitaxial TTO films on Al_2O_3 (0001) substrates. These results clearly demonstrate that the seed layer method is indeed effective for achieving high μ_H for SnO_2 films.

Then, I expanded material exploration for the seed layer from rutile oxides to binary oxides using several selection criteria: oriented growth, high crystallinity, large grain, availability, and nontoxicity. As a result, I found that anatase TiO_2 seed layers unexpectedly promoted (100)-preferred growth of SnO_2. Furthermore, the optimized TTO films on the anatase TiO_2 seed layers exhibited a very high μ_H value of 83 $cm^2V^{-1}s^{-1}$ at $n_e = 2.7 \times 10^{20}$ cm^{-3}. This remarkably high μ_H value is the largest ever reported for doped epitaxial or polycrystalline SnO_2 thin films, and is comparable to the μ_H values of high-μ_H

In_2O_3-based TCOs. More importantly, this is the first result that achieved the target μ_H value of 80 $cm^2V^{-1}s^{-1}$, although further reduction in n_e without reducing μ_H was required.

In order to obtain SnO_2 films with further reduced n_e and enhanced μ_H, I took two approaches: dopant optimization, and the use of seed layers with complex composition. I explored several elements for a potential dopant that enhances not only n_e, but also μ_H, as demonstrated in In_2O_3-based TCOs. Consequently, I found that SnO_2 films doped with W exhibited slightly better μ_H values than TTO films. The doping efficiencies for the WTO films were lower than those for the TTO films, suggesting that some of the doped W might locate at grain boundaries and passivate dangling bonds.

Finally, I extended material exploration for the seed layer of SnO_2 from binary oxides to ternary oxides. Using rutile TNO solid solutions as the seed layer, I investigated the effects of lattice matching on the structural and transport properties of SnO_2 films. WTO films grown on TNO with z = 0.45 and 0.5 showed (001)-preferred growth. This preferred growth was probably realized by epitaxially stabilized (001) nuclei via nearly perfect lattice matching along the a-axis of TNO to SnO_2. The WTO films with (001)-preferred growth exhibited an overwhelmingly high μ_H value of 136 $cm^2V^{-1}s^{-1}$ at $n_e = 1.4 \times 10^{20}$ cm^{-3}. I speculate that the dramatically enhanced μ_H value originates from not only decreased density of misfit dislocation, but also (001)-orientation; (001)-oriented growth would more effectively suppress propagation of {101} planar defects, which might act more effectively as a grain boundary than growth in other orientations. As a consequence of very high μ_H with reduced n_e, the WTO films with low R_s values of approximately 10 $\Omega sq.^{-1}$ exhibited a low absorption of 3.5% at the wavelength of 1400 nm.

These properties sufficiently meet the requirement for the electrode of the next-generation full-spectrum PVCs. It should be noted that the obtained μ_H value of 136 $cm^2V^{-1}s^{-1}$ is 70% higher than the target value of 80 $cm^2V^{-1}s^{-1}$. The 70% margin suggests that high μ_H values exceeding 80 $cm^2V^{-1}s^{-1}$ might be achieved for SnO_2 films fabricated even in disadvantageous processes: low temperature deposition and sputtering. I believe these findings will truly pave the way for massive production of SnO_2-based TCOs suitable for the next-generation full-spectrum PVCs.

9.2 Future Prospects

Finally, I discuss the future prospects of this study in applied research and basic science in the following section.

(1) Transfer of the Findings to Sputtering

Most importantly, the findings obtained by PLD in this study must be transferred to sputtering for the future use of commercial PVCs. As shown in Fig. 9.2, a research group including this author has already confirmed that anatase TiO_2 seed layers enhanced the μ_H values of sputtered TTO films [128]. However, the maximum μ_H value for the sputtered films was 49 $cm^2V^{-1}s^{-1}$, which is still lower than those obtained for PLD films. The origin for the decreased μ_H might be hindered epitaxial growth due to the bombardment of high energy particles and/or increased in-grain scattering due to sputtering damage [129,130]. Future studies should clarify the origin of additional scattering and develop a method that

can suppress the scattering. While binary oxides are easily fabricated by sputtering, special care should be taken during the sputter-deposition of ternary oxides. I carried out a preliminary sputtering study using solid solution seed layers in vain; sputtered WTO films on TNO with nominal z = 0.5 showed very weak (001)-preferred growth and a low μ_H value of 35 $cm^2V^{-1}s^{-1}$. This is most likely because of compositional deviation [131] of the seed layer from the nominal value due to difference in sputtering rate and scattering by the process gas. A future study should be carried out with special care dedicated to the actual composition of the seed layer. One possible way to reduce absolute compositional deviation in Ti and Nb is to use (Ti,Nb,Sn)O_2 as the seed layer.

(2) Formation of Textured Surface

Surface texture is highly critical for conversion efficiencies of thin film Si PVCs [132]. This is because light trapping by the surface texture is mandatory to complement the low absorption coefficient of Si thin films. Textured surfaces are naturally formed on as-deposited FTO [133] and B-doped ZnO films [134] grown by CVD, whereas oxide films grown by PVD generally possess flat surfaces. To date, many efforts have been dedicated to fabricate textured surfaces on Al-doped ZnO films grown by sputtering [135,136]. The etching of thick films [135] sometimes combined with annealing and high pressure deposition [136] successfully led to textured surfaces on sputtered ZnO films comparable with CVD films. However, to my knowledge no attempt has been made to obtain textured SnO_2 films grown by PVD, probably due to poor etching properties of SnO_2.

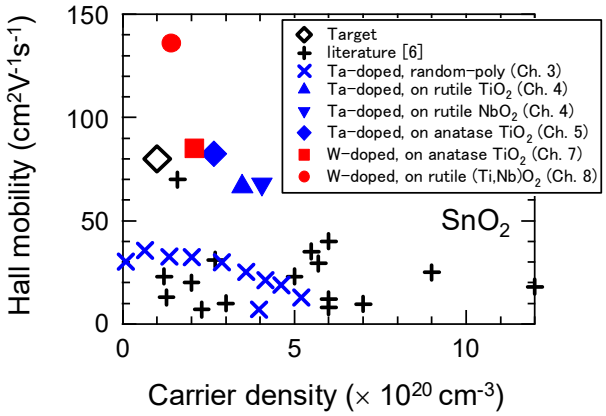

Fig. 9.1. Summary of the transport properties obtained in this study.

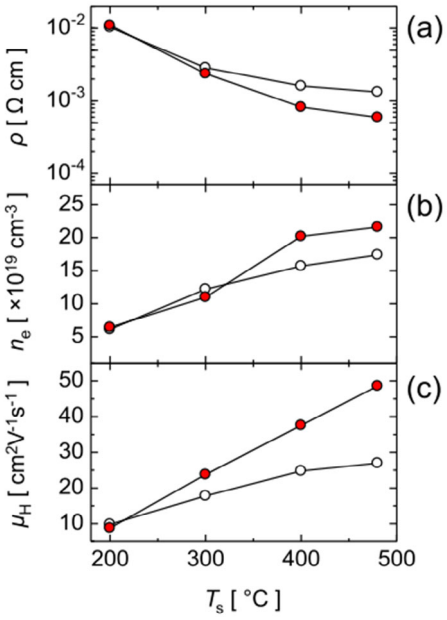

Fig. 9.2. (a) ρ, (b) n_e, and (c) μ_H of sputtered TTO films on bare glass (open circles) and on anatase TiO_2 seed layers (closed circles) deposited at various growth temperature. (Copyright (2010) The Japan Society of Applied Physics)

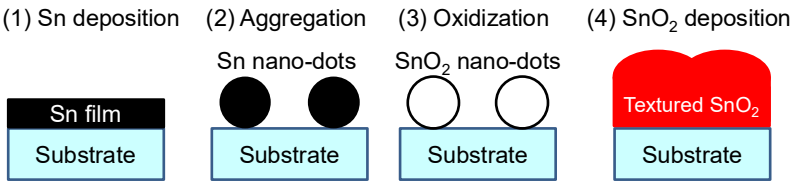

Fig. 9.3. Schematics of a proposed method for fabrication of textured surface on SnO_2 films grown by PVD.

Here, I propose a possible method for the fabrication of textured SnO_2 films by PVD. The proposed method is to use an aggregation of metallic Sn as a template for a textured surface. Sn metal has a low melting point (231.9 °C) together with low vapor pressure at the melting point. In addition, oxide surfaces are poorly wettable by Sn melt, as widely observed in daily soldering. Therefore, metallic Sn films on oxide substrates are expected to aggregate above the melting point and form self-assembled nano-dots. Kim et al. demonstrated Sn nano-dots on glass substrates using this approach [137]. They used the nano-dots as a mask for a nano-cone structure, whereas I am planning to use the nano-dots as a template for a textured surface. Conveniently, the size of the nano-dots can be systematically controlled by thickness of the Sn films. In addition, the nano-dots have a hemispheric shape that is desirable for trapping light in the NIR region. The conversion of Sn nano-dots into SnO_2 by annealing in oxidative ambient would yield transparent textured substrates. Finally, doped SnO_2 thin films would be deposited on the textured substrates. To summarize, the proposed method consists of four steps: deposition of metallic Sn films on substrates, formation of nano-dots by heating, oxidization of Sn into SnO_2, and deposition of doped SnO_2 films.

It should be stressed that this method is compatible with practical sputtering for SnO_2 deposition. Reactive sputtering using metallic targets has been preferably used to deposit doped SnO_2 films because of low target cost and high deposition rate. Metallic targets such as sintered Sn:Ta [138] and alloyed Sn:Sb [139] can be used to deposit not only SnO_2, but also metallic Sn. Furthermore, the proposed method requires only one additional process (Sn deposition on unheated substrates) to the usual SnO_2 deposition; aggregation and oxidization of the Sn films are sufficiently completed during substrate

heating and pre-sputtering under oxygen flow, respectively, for the SnO_2 deposition. Therefore, the proposed method is low cost and scalable, in principle. An experimental demonstration of this method is underway.

(3) Basic Scientific Issues to Be Addressed

This study is application-oriented and thus some basic, yet important, scientific issues remain unaddressed. Nevertheless, resolving such issues will not only be scientifically important, but also practically important, as discussed below.

One essential issue is to understand grain-boundary scattering in TCOs quantitatively and microscopically. The scattering at a high angle grain boundary in randomly oriented polycrystalline SnO_2 films remains unscreened even in the heavily doped region of n_e above 5×10^{20} cm^{-3} (Fig. 3.3). This behavior is in sharp contrast to screened grain boundary scattering in heavily doped ZnO and In_2O_3. Eliminating the high angle grain boundary from SnO_2 was demonstrated by using seed layers, resulting in dramatically enhanced μ_H. Nevertheless, the remaining low angle grain boundary and CSP introduced by the lattice-mismatched epitaxial growth most likely act as the source of grain boundary scattering in the lightly doped region of n_e below 3×10^{20} cm^{-3}. However, no quantitative analysis of these scatterings has been performed to date. Thus, it is highly challenging but worthwhile to propose a microscopic model that can quantitatively predict scatterings at the grain-boundaries with various structures, including CSPs. Such a model must be highly beneficial for analysis of transport properties of TCOs.

The most important issue is most likely to explain the mechanism behind the strong influence of growth temperature on both n_e and μ_H of SnO_2 (Fig. 6.4.). The decrease in n_e suggests the formation of inactive dopants and/or unfavorable defects such as clustered dopants [36] and accepter-like defects [16]. I performed a preliminary analysis on the optical mobility of TTO films grown at low temperature and found that the optical mobility coincides well with μ_H. This indicates that intra-grain scattering rather than grain boundary scattering is responsible for the decreased μ_H value of SnO_2 films. It is thus highly important to quantitatively clarify the origin of the decreased n_e and its influence on μ_H. A detailed investigation on lattice parameters assisted by first principle calculations might be insightful. Direct determination of defect size by using positron annihilation measurements [140] would be highly invaluable. A technique that can suppress the defect formation might be developed on the basis of those investigations. Albeit by chance, I succeeded in enhancing the doping efficiency of Nb-doped SnO_2 using tensile epitaxial strain (see appendix B). I believe that scientifically confirmed findings are beneficial for the fabrication of high quality SnO_2, even at low growth temperatures.

(4) Beyond SnO_2

Although I focused on SnO_2 in this study, I believe that most of the insight obtained in this study can be extended to other rutile compounds. Thus, functional rutile materials such as TiO_2, VO_2, and MnO_2 might be fabricated with improved properties by using the unique growth design found in this study: c-axis oriented growth of main layers on a-axis matched polycrystalline seed layers of solid solutions. Z. Hiroi [141] pointed out that

flexibility of the rutile structure leads to a wide range of lattice parameters and thus large lattice mismatch of the rutile compounds. This means perfectly matched a-axis together with largely mismatched c-axis might be realized in other systems than SnO_2 on $(Ti,Nb)O_2$. In addition, most rutile compounds probably share other requirements for this technique: highly energetically unstable (001) and high growth speed with reactive {111}. That is because these properties are mainly determined by the crystal structure. I hope this technique will eventually open up the avenue towards improved functional films with oriented growth on amorphous substrates.

Acknowledgments

This work was conducted at the Kanagawa Academy of Science and Technology.

First and foremost, I would like to express my wholehearted gratitude to my advisor, Prof. Tetsuya Hasegawa, without whom, none of this work would have been possible. Without his profound understanding of not only science but also human nature, I would have led a life detached from science, and may have occasionally suffered from the embers. I would need many more pages to express the full extent of my gratitude.

My deepest appreciation goes to Professors Hiroshi Fujioka, Kazuya Yamaguchi, Masaru Miyayama, and Yuji Noguchi for invaluable comments and discussion, which helped me to review this work from more sophisticated and generic perspectives. In particular, I would like to express my deepest gratitude to Prof. Masaru Miyayama for his kindness, generousness, and invaluable help with deep insight based on science with broad perspectives.

I would like to express my deep gratitude to Professors Naoomi Yamada, Taro Hitosugi, Toshihiro Shimada, and Yasushi Hirose for their invaluable help in experiments, comments, discussion, and encouragements. I gratefully appreciate Drs. Akira Chikamatsu, Enju Sakai, Hideyuki Kamisaka, Junpei Kasai, Kei Shigematsu, Sohei Okazaki, and Yutaka Furubayashi for their valuable discussion, comments, and help. I would also like to thank all the present and former students and secretaries of Hasegawa laboratory for their help and kindness. As representative, a special thanks is extended to Michitaka Fukumoto and Daisuke Ogawa for their substantial collaboration efforts, which have been very insightful for me.

My heartfelt appreciation goes to Mrs. Reiko Nagashima and Prof. Hidenori Takagi for their sincere encouragement. In particular, I would like to thank Mrs. Reiko Nagashima, the former secretary of the laboratory when I was a student. She kindly helped (and actually pushed) me to return to science. This work would be impossible without her unwavering kindness.

Lastly, I owe my deepest gratitude to my parents, Daisuke and Tsuneyo, and my sisters, Miyabi and Chinatsu, who willingly agreed to support my endeavors.

References

[1] *Handbook of Transparent Conductors*, ed. D. S. Ginley (Springer, New York, 2010)

[2] D.S. Ginley and C. Bright, MRS Bull. **25**, 15 (2000).

[3] G.J. Exarhos and X.-D. Zhou, Thin Solid Films **515**, 7025 (2007).

[4] K. Ellmer, Nat. Photonics **6**, 809 (2012).

[5] S.C. Dixon, D.O. Scanlon, C.J. Carmalt, and I.P. Parkin, J. Mater. Chem. C **419**, 462 (2016).

[6] *Toumeidoudenmaku No Gijutsu* (*Technology of Transparent Conductive Oxide Thin-films*) ed. The 166th Committee on Photonic and Electronic Oxide of the Japan Society for the Promotion of Science (Ohmsha, Tokyo, 2014) 3rd ed. [in Japanese]

[7] PV2030+, http://www.nedo.go.jp/library/pv2030_index.html

[8] J.M. Kroon, N.J. Bakker, H.J.P. Smit, P. Liska, K.R. Thampi, P. Wang, S.M. Zakeeruddin, M. Grätzel, A. Hinsch, S. Hore, U. Würfel, R. Sastrawan, J.R. Durrant, E. Palomares, H. Pettersson, T. Gruszecki, J. Walter, K. Skupien, and G.E. Tulloch, Prog. Photovolt: Res. Appl. **15**, 1 (2007).

[9] G. Hautier, A. Miglio, G. Ceder, G.-M. Rignanese, and X. Gonze, Nat. Commun. **4**, 2292 (2013).

[10] T.S. Moss, Proc. Phys. Soc. London, Sect. B **67**, 775 (1954).

[11] E. Burstein, Phys. Rev. **93**, 632 (1954).

[12] I. Hamberg and C.G. Granqvist, J. Appl. Phys. **60**, R123 (1986).

[13] J.R. Bellingham, W.A. Phillips, and C.J. Adkins, J. Mater. Sci. Lett. **11**, 263 (1992).

[14] J. Steinhauser, S. Faÿ, N. Oliveira, E. Vallat-Sauvain, and C. Ballif, Appl. Phys. Lett. **90**, 142107 (2007).

[15] Y. Furubayashi, N. Yamada, Y. Hirose, Y. Yamamoto, M. Otani, T. Hitosugi, T. Shimada, and T. Hasegawa, J. Appl. Phys. **101**, 093705 (2007).

[16] J. Jia, N. Oka, M. Kusayanagi, S. Nakatomi, and Y. Shigesato, Appl. Phys. Express **7**, 105802 (2014).

[17] S. Brehme, F. Fenske, W. Fuhs, E. Nebauer, M. Poschenrieder, B. Selle, and I. Sieber, Thin Solid Films **342**, 167 (1999).

[18] T. Minami, MRS Bull. **25**, 38 (2000).

[19] J.Y.W. Seto, J. Appl. Phys. **46**, 5247 (1975).

[20] T.J. Coutts, D.L. Young, and X. Li, MRS Bull. **25**, 58 (2000).

[21] E. Fortunato, D. Ginley, and H. Hosono, MRS Bull. **32**, 716 (2007).

[22] W. Shockley and H.J. Queisser, J. Appl. Phys. **32**, 510 (1961).

[23] T. Oyama, J. Surf. Finishing Soc. Jpn. **60**, 616 (2009). [in Japanese]

[24] Y. Meng, X. Yang, H. Chen, J. Shen, Y. Jiang, Z. Zhang, and Z. Hua, Thin Solid Films **394**, 218 (2001).

[25] S. Calnan and A.N. Tiwari, Thin Solid Films **518**, 1839 (2010).

[26] T. Koida, H. Fujiwara, and M. Kondo, Jpn. J. Appl. Phys. **46**, L685 (2007).

[27] T. Koida, M. Kondo, K. Tsutsumi, A. Sakaguchi, M. Suzuki, and H. Fujiwara, J. Appl. Phys. **107**, 033514 (2010).

[28] T. Koida, H. Fujiwara, and M. Kondo, Sol. Energy Mater. Sol. Cells **93**, 851 (2009).

[29] A. Polman, M. Knight, E.C. Garnett, B. Ehrler, and W.C. Sinke, Science **352**, 307 (2016).

[30] T. Mishima, M. Taguchi, H. Sakata, and E. Maruyama, Sol. Energy Mater. Sol. Cells **95**, 18 (2011).

[31] A. Tanaka, M. Hirata, Y. Kiyohara, M. Nakano, K. Omae, M. Shiratani, and K. Koga, Thin Solid Films **518**, 2934 (2010).

[32] C.G. Fonstad and R.H. Rediker, J. Appl. Phys. **42**, 2911 (1971).

[33] D.F. Morgan and D.A. Wright, Br. J. Appl. Phys. **17**, 337 (1966).

[34] Z. Galazka, R. Uecker, D. Klimm, K. Irmscher, M. Pietsch, R. Schewski, M. Albrecht, A. Kwasniewski, S. Ganschow, D. Schulz, C. Guguschev, R. Bertram, M. Bickermann, and R. Fornari, Phys. Status Solidi A **211**, 66 (2014).

[35] K.J. Button, C.G. Fonstad, and W. Dreybrodt, Phys. Rev. B **4**, 4539 (1971).

[36] K. Ellmer, J. Phys. D: Appl. Phys. **34**, 3097 (2001).

[37] L. Kaplan, R. L. Boxman, S. Goldsmith, U. Rosenberg, and M. Nathan: Thin Solid Films **253,** 1 (1994).

[38] D. Bélanger, J.P. Dodelet, B.A. Lombos, and J.I. Dickson, J. Electrochem. Soc. **132**, 1398 (1985).

[39] C. Agashe, J. Hüpkes, G. Schöpe, and M. Berginski, Sol. Energy Mater. Sol. Cells **93**, 1256 (2009).

[40] M. Isshiki, T. Ikeda, J. Okubo, T. Oyama, E. Shidoji, H. Odaka, P. Sichanugrist, and M. Konagai, Jpn. J. Appl. Phys. **51**, 095801 (2012)

[41] S. Semancik and R.E. Cavicchi, Thin Solid Films **206**, 81 (1991).

[42] K. Rachut, C. Körber, J. Brötz, and A. Klein, Phys. Status Solidi A **211**, 1997 (2014).

[43] D.H. Kim, W.-S. Kim, S.B. Lee, and S.-H. Hong, Sens. Actuators B Chem. **147**, 653 (2010).

[44] M. Okude, K. Ueno, S. Itoh, M. Kikuchi, A. Ohtomo, and M. Kawasaki, J. Phys. D: Appl. Phys. **41**, 125309 (2008).

[45] Y. Zhen, T. Ohsawa, Y. Adachi, I. Sakaguchi, B. Li, J. Li, R. Matsuoka, T. Nishimura, K. Matsumoto, H. Haneda, and N. Ohashi, J. Appl. Phys. **108**, 104901 (2010).

[46] L.C. Tien, D.P. Norton, and J.D. Budai, Mater. Res. Bull. **44**, 6 (2009).

[47] H. Toyosaki, M. Kawasaki, and Y. Tokura, Appl. Phys. Lett. **93**, 132109 (2008).

[48] Y. Kim, S.W. Lee, and H. Chen, Thin Solid Films **405**, 256 (2002).

[49] J.E. Dominguez, L. Fu, and X.Q. Pan, Appl. Phys. Lett. **81**, 5168 (2002).

[50] H. Wakabayashi, T. Suzuki, Y. Iwazaki, and M. Fujimoto, Jpn. J. Appl. Phys. **40**, 6081 (2001).

[51] A. Tsukazaki, A. Ohtomo, and M. Kawasaki, Appl. Phys. Lett. **88**, 152106 (2006).

[52] O. Bierwagen and J.S. Speck, Appl. Phys. Lett. **97**, 072103 (2010).

[53] M.E. White, M.Y. Tsai, F. Wu, and J.S. Speck, J. Vac. Sci. Technol. A **26**, 1300 (2008).

[54] M.E. White, O. Bierwagen, M.Y. Tsai, and J.S. Speck, J. Appl. Phys. **106**, 093704 (2009).

[55] H. Mun, H. Yang, J. Park, C. Ju, and K. Char, APL Mater. **3**, 076107 (2015).

[56] T. Minami, Semicond. Sci. Technol. **20**, S35 (2005).

[57] *Pulsed Laser Deposition of Thin Films*, ed. D. B. Chrisey and G. K. Hubler (Wiley, New York, 1994).

[58] S.A. Reid, W. Ho, and F.J. Lamelas, J. Phys. Chem. B **104**, 5324 (2000).

[59] Y. Furubayashi, T. Hitosugi, Y. Yamamoto, K. Inaba, G. Kinoda, Y. Hirose, T. Shimada, and T. Hasegawa, Appl. Phys. Lett. **86**, 252101 (2005).

[60] T. Hitosugi, A. Ueda, S. Nakao, N. Yamada, Y. Furubayashi, Y. Hirose, T. Shimada, and T. Hasegawa, Appl. Phys. Lett. **90**, 212106 (2007).

[61] N. Yamada, T. Hitosugi, N.L.H. Hoang, Y. Furubayashi, Y. Hirose, T. Shimada, and T. Hasegawa, Jpn. J. Appl. Phys. **46**, 5275 (2007).

[62] M. Junghähnel, T. Kopte, and O. Zywitzki, Vak. Forsch. Und Prax. **23**, 22 (2011).

[63] N. Oka, Y. Sanno, J. Jia, S.I. Nakamura, and Y. Shigesato, Appl. Surf. Sci. **301**, 551 (2014).

[64] I. Jeon, S. Nakao, Y. Hirose, T. Hasegawa, and Y. Matsuo, Adv. Electron. Mater. **2**, 1500341 (2016).

[65] N.L.H. Hoang, Y. Hirose, S. Nakao, and T. Hasegawa, Appl. Phys. Express **4**, 105601 (2011).

[66] S. Okazaki, J. Ohkubo, S. Nakao, Y. Hirose, T. Hitosugi, and T. Hasegawa, Jpn. J. Appl. Phys. **51**, 118003 (2012).

[67] S. Okazaki, T. Ohhashi, S. Nakao, Y. Hirose, T. Hitosugi, and T. Hasegawa, Jpn. J. Appl. Phys. **52**, 098002 (2013).

[68] S. Nakao, Y. Hirose, and T. Hasegawa, J. Semicond. **37**, 022001 (2016).

[69] T. Ohnishi, H. Koinuma, and M. Lippmaa, Appl. Surf. Sci. **252**, 2466 (2006).

[70] T. Ohnishi, M. Lippmaa, T. Yamamoto, S. Meguro, and H. Koinuma, Appl. Phys. Lett. **87**, 241919 (2005).

[71] T. Ohnishi, K. Shibuya, T. Yamamoto, and M. Lippmaa, J. Appl. Phys. **103**, 0 (2008).

[72] R.E. Leuchtner, Appl. Surf. Sci. **127-129**, 626 (1998).

[73] H. Kim and A. Piqué, Appl. Phys. Lett. **84**, 218 (2004).

[74] H. Kim, R.C.Y. Auyeung, and A. Piqué, Thin Solid Films **516**, 5052 (2008).

[75] S. W. Lee, Y.-W. Kim, and H. Chen, Appl. Phys. Lett. **78,** 350 (2001).

[76] Y. Mihara, R. Satoh, R. Usui, E. Morinaga, and Y. Iwata, SID Int. Symp. Dig. Tech. Pap. **38,** 399 (2007).

[77] Y. Muto, S. Nakatomi, N. Oka, Y. Iwabuchi, H. Kotsubo, and Y. Shigesato, Thin Solid Films **520**, 3746 (2012).

[78] M. Weidner, J. Brötz, and A. Klein, Thin Solid Films **555**, 173 (2014).

[79] G. Turgut, Thin Solid Films **594**, 56 (2015).

[80] M. Worsdale, A. Rabis, E. Fabbri, T.J. Schmidt, and D. Kramer, ECS Trans. **69**, 1167 (2015).

[81] M. Weidner, J. Jia, Y. Shigesato, and A. Klein, Phys. Status Solidi **B 253**, 923 (2016).

[82] E. Elangovan, S.A. Shivashankar, and K. Ramamurthi, J. Cryst. Growth **276,** 215 (2005).

[83] E. Elangovan and K. Ramamurthi, Thin Solid Films **476,** 231 (2005).

[84] C. Körber, J. Suffner, and A. Klein, J. Phys. D: Appl. Phys. **43**, 055301 (2010).

[85] N. Yamada, T. Hitosugi, J. Kasai, N.L.H. Hoang, S. Nakao, Y. Hirose, T. Shimada, and T. Hasegawa, J. Appl. Phys. **105**, 123702 (2009).

[86] L. Wang, Y. Yang, S. Jin, and T.J. Marks, Appl. Phys. Lett. **88**, (2006).

[87] C.H. Yi, I. Yasui, and Y. Shigesato, Jpn. J. Appl. Phys. **34**, 1638 (1995).

[88] *Structure and Properties of Inorganic Solids*, F. S. Galasso (Pergamon, Oxford, 1970).

[89] M. Ramamoorthy and D. Vanderbilt, Phys. Rev. **B 49**, 16721 (1994).

[90] F. Picard-Lagnel, B. Poumellec, and C. Picard, Thin Solid Films **174**, 209 (1989).

[91] J. Narayan and B.C. Larson, J. Appl. Phys. **93**, 278 (2003).

[92] Y. Hirose, N. Yamada, S. Nakao, T. Hitosugi, T. Shimada, and T. Hasegawa, Phys. Rev. B **79**, 165108 (2009).

[93] T. Hitosugi, N. Yamada, S. Nakao, K. Hatabayashi, T. Shimada, and T. Hasegawa, J. Vac. Sci. Technol. A **26**, 1027 (2008).

[94] V. Pore, M. Ritala, M. Leskelä, T. Saukkonen, and M. Järn, Cryst. Growth Des. **9**, 2974 (2009).

[95] C. Agashe, M.G. Takwale, B.R. Marathe, and V.G. Bhide, J. Mater. Sci. **24**, 2628 (1989).

[96] C. Agashe and S. S. Major, J. Mater. Sci. **31,** 2965 (1996).

[97] S.R. Vishwakarma, J.P. Upadhyay, and H.C. Prasad, Thin Solid Films **176,** 99 (1989).

[98] M. Batzill and U. Diebold, Prog. Surf. Sci. **79**, 47 (2005).

[99] G.J.A. Mannie, J. van Deelen, J.W. Niemantsverdriet, and P.C. Thüne, Appl. Phys. Lett. **98**, 051907 (2011).

[100] A. Smith, J. Laurent, D.S. Smith, J.P. Bonnet, and R.R. Clemente, Thin Solid Films **266**, 20 (1995).

[101] N. Yamada, I. Yasui, Y. Shigesato, H. Li, Y. Ujihira, and K. Nomura, Jpn. J. Appl. Phys. **39**, 4158 (2000).

[102] H. Nogawa, T. Hitosugi, A. Chikamatsu, S. Nakao, Y. Hirose, T. Shimada, H. Kumigashira, M. Oshima, and T. Hasegawa, Jpn. J. Appl. Phys. **49**, 041102 (2010).

[103] C. Agashe and S.S. Major, J. Mater. Sci. Lett. **15**, 497 (1996).

[104] N. Noor and I.P. Parkin, Thin Solid Films **532**, 26 (2013).

[105] J.P. Upadhyay, S.R. Vishwakarma, and H.C. Prasad, Thin Solid Films **169**, 195 (1989).

[106] Y.-S. Hsu and S.K. Ghandhi, J. Electrochem. Soc. **127**, 1596 (1980).

[107] K. Watanabe, I. Sakaguchi, M. Hashiguchi, N. Saito, E.M. Ross, H. Haneda, T. Ohsawa, and N. Ohashi, J. Appl. Phys. **119**, (2016).

[108] R.D. Shannon, Acta Crystallogr. Sect. A **32**, 751 (1976).

[109] V. Casey and M.I. Stephenson, J. Phys. D. Appl. Phys. **23**, 1212 (1990).

[110] B. Stjerna, E. Olsson, and C.G. Granqvist, J. Appl. Phys. **76**, 3797 (1994).

[111] A. Kurz, K. Brakecha, J. Puetz, and M.A. Aegerter, Thin Solid Films **502**, 212 (2006).

[112] Y. Huang, Q. Zhang, G. Li, and M. Yang, Mater. Charact. **60**, 415 (2009).

[113] Y. Huang, Q. Zhang, and G. Li, Semicond. Sci. Technol. **24**, 015003 (2009).

[114] Y. Huang, G. Li, J. Feng, and Q. Zhang, Thin Solid Films **518**, 1892 (2010).

[115] M. Wang, Y. Gao, Z. Chen, C. Cao, J. Zhou, L. Dai, and X. Guo, Thin Solid Films **544**, 419 (2013).

[116] S. Yu, L. Li, Z. Sun, H. Zheng, H. Dong, D. Xu, and W. Zhang, J. Am. Ceram. Soc. **98**, 1121 (2015).

[117] H. Peng, J.D. Perkins, and S. Lany, Chem. Mater. **26**, 4876 (2014).

[118] W. Zhou, L. Liu, M. Yuan, Q. Song, and P. Wu, Comput. Mater. Sci. **54**, 109 (2012).

[119] D. Cheng, M. Zhang, J. Chen, C. Yang, X. Zeng, and D. Cao, J. Phys. Chem. C **118**, 2037 (2014).

[120] *Superconductivity Conventional and Unconventional Superconductors*, ed. K.-H. Bennemann and J.B. Ketterson (Springer, New York, 2008)

[121] M. Park, T.E. Mitchell, and A.H. Heuer, J. Am. Ceram. Soc. **58**, 43 (1975).

[122] K. Sakata, J. Phys. Soc. Jpn. **26**, 1067 (1969).

[123] F. Kawamura, I. Yasui, M. Kamei, and I. Sunagawa, J. Am. Ceram. Soc., **84**, 1341 (2001).

[124] P.S. Peercy and B. Morosin, Phys. Rev. B **7**, 2779 (1973).

[125] K. Sakata, J. Phys. Soc. Japan **26**, 582 (1969).

[126] H.P. Kirchner, J. Am. Ceram. Soc. **52**, 379 (1969).

[127] M. Fukumoto, S. Nakao, K. Shigematsu, D. Ogawa, K. Morikawa, Y. Hirose, and T. Hasegawa, unpublished.

[128] N. Yamada, S. Nakao, T. Hitosugi, and T. Hasegawa, Jpn. J. Appl. Phys. **49**, 1080021 (2010).

[129] I. Petrov, P.B. Barna, L. Hultman, and J.E. Greene, J. Vac. Sci. Technol. A **21**, S117 (2003).

[130] K. Ellmer and T. Welzel, J. Mater. Res. **27**, 765 (2012).

[131] F. Lagnel, B. Poumellec, J.P. Thomas, A. Ziani, M. Gasgnier, J.F. Marucco, and C. Picard, Thin Solid Films **176**, 111 (1989).

[132] F.-J. Haug and C. Ballif, Energy Environ. Sci. **8**, 824 (2015).

[133] M. Mizuhashi, Y. Gotoh, and K. Adachi, Jpn. J. Appl. Phys. **27**, 2053 (1988).

[134] S. Faÿ, J. Steinhauser, S. Nicolay, and C. Ballif, Thin Solid Films **518**, 2961 (2010).

[135] O. Kluth, G. Schöpe, J. Hüpkes, C. Agashe, J. Müller, and B. Rech, Thin Solid Films **442**, 80 (2003).

[136] T. Minami, T. Miyata, R. Uozaki, H. Sai, and T. Koida, Thin Solid Films **614**, 56 (2016).

[137] J. Kim, A.J. Hong, J.W. Nah, B. Shin, F.M. Ross, and D.K. Sadana, ACS Nano **6**, 265 (2012).

[138] Y. Muto, S. Nakatomi, N. Oka, Y. Iwabuchi, H. Kotsubo, and Y. Shigesato, Thin Solid Films **520**, 3746 (2012).

[139] Y. Muto, N. Oka, N. Tsukamoto, Y. Iwabuchi, H. Kotsubo, and Y. Shigesato, Thin Solid Films **520**, 1178 (2011).

[140] E. Korhonen, V. Prozheeva, F. Tuomisto, O. Bierwagen, J.S. Speck, M.E. White, Z. Galazka, H. Liu, N. Izyumskaya, V. Avrutin, Ü. Özgür, and H. Morkoç, Semicond. Sci. Technol. **30**, 024011 (2015).

[141] Z. Hiroi, Prog. Solid State Chem. **43**, 47 (2015).

Appendix A: Scatterings in Carrier Transport of Transparent Conductive Oxides

In this appendix, scatterings in the carrier transport of transparent conductive oxides (TCOs) and the corresponding formulae are briefly reviewed for the aid of semi-quantitative understanding of the transport properties of SnO_2 thin films.

Introduction

Many efforts have been dedicated to formulate various scatterings in the carrier transport of elemental semiconductors, as well as compound semiconductors. These scattering include phonon, ionized impurity, neutral impurity, grain boundary, dislocation, and alloy scattering. The obtained insights have been used to analyze the transport properties of TCOs [1, 2] although alloy scattering has been usually ignored. Fortunately, phonon and ionized impurity scatterings, which are unavoidable, can be reliably estimated although other scatterings are rather poorly understood at present. As shown in Fig. 8.5, high quality SnO_2 films exhibited extremely high Hall mobility (μ_H) consistent with the upper limit owing to phonon and ionized impurity scatterings. In contrast, it is highly challenging to quantitatively identify scatterings in films with low μ_H.

Phonon Scattering

Three modes of phonon scatterings are known: Polar optical phonon (POP), acoustic deformation potential (ADP), and acoustic piezoelectric scatterings. Owing to its centrosymmetric crystal structure, acoustic piezoelectric scattering is absent from the carrier transport of SnO_2. μ_H limited by POP (μ_{POP}) is written as

$$\mu_{POP} \propto \left[\exp\left(\frac{\hbar\omega_0}{k_B T}\right) - 1\right],$$

where $\hbar$ is the reduced Planck constant, ω_0 is the phonon frequency, k_B is the Boltzmann constant, and T is temperature. On the other hand, μ_H limited by ADP (μ_{ADP}) is written as

$$\mu_{ADP} \propto T^{-\frac{3}{2}}.$$

Clearly, these formulae indicate that phonon limited μ_H (μ_{PH}) show a negative coefficient in μ_H-T curves, which was clearly observed for the bulk single crystals of SnO_2 (Fig. 1.9). In addition, the result showed that POP scattering was dominant near room T, whereas the contribution of ADP scattering was significant at low T. It should be noted that only a few studies on thin films of SnO_2 reported negative coefficients in the μ_H-T curves (Fig. 1.15(d)). Because μ_{PH} is independent of carrier density (n_e), a simple method for

considering μ_H by taking μ_{PH} into account is to use literature values of bulk single crystals as the upper limit of μ_{PH}.

Ionized Impurity Scattering

It is widely accepted that ionized impurity scattering (IIS) dominates carrier transport in heavily doped TCOs [1, 2] because dopants with the concentrations on the order of 10^{20} cm^{-3} act as ionized impurity. For example, Ta^{5+} substituted at Sn^{4+} sites acts as singly charged ionized impurities. The so-called Brooks-Herring-Dingle (BHD) formula [2, 3] is generally used to calculate IIS limited μ_H (μ_{IIS}), which is written as

$$\mu_{IIS} = \frac{24\pi^3(\epsilon_0\epsilon_r)^2\hbar^3 n_e}{e^3 m^{*2} F_{II} Z^2 n_I},$$

where ε_0 is the permittivity of free space, ε_r is the relative static dielectric constant, $\hbar$ is the reduced Planck constant, e is the elementary charge, and m^* is the effective electron mass. Z and n_I are the charge and the density of ionized impurity, respectively. The screening function, F_{II}, is given by

$$F_{II} = \ln(1 + 4/\xi) - (1 + \xi/4)^{-1}$$

with

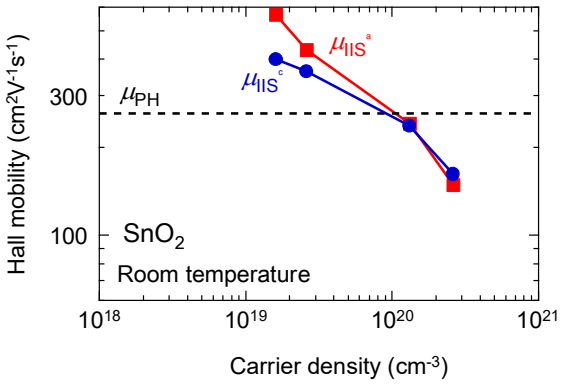

Fig. A.1. Comparison of calculated μ_{IIS} along the a-axis (μ_{IIS}^{a}) and c-axis (μ_{IIS}^{c}) with μ_{PH} derived from the data of single crystals.

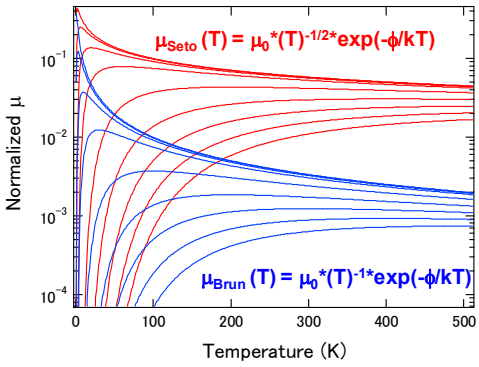

Fig. A.2. Simulated μ_{GB} based on Seto and Bruneaux models with barrier heights from 1–500 K.

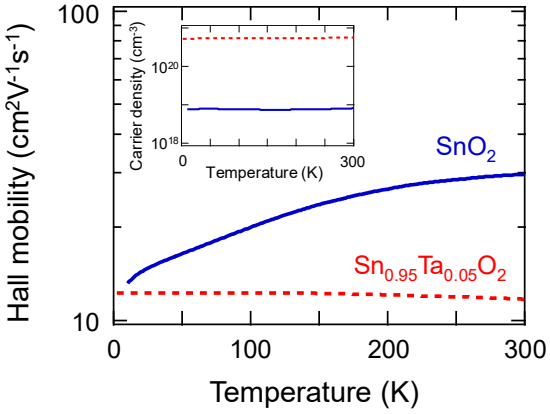

Fig. A.3. Temperature dependence of μ_H and n_e (inset) for polycrystalline SnO_2 (solid lines) and $Sn_{0.95}Ta_{0.05}O_2$ (broken lines) films on glass.

$$\xi = \frac{e^2 m^*}{\pi \epsilon_0 \epsilon_r \hbar^2 (3\pi^5)^{1/3} {n_e}^{1/3}}.$$

From the formula, it is clear that μ_{IIS} is independent of T. Here, it should be stressed that m^* increases as n_e increases due to nonparabolicity (which is difficult to estimate) of the conduction band. Fortunately, a recent ellipsometry study [4] on Sb-doped SnO_2 provides us with an experimentally determined m^* as a function of n_e. Figure A.1 shows calculated μ_{IIS} for SnO_2 in which $n_I = n_e$ is assumed and ε_r is taken from [5]. It is clear that at $n_e > 1 \times 10^{20}$ cm^{-3}, μ_{IIS} is dominant whereas at $n_e < 1 \times 10^{20}$ cm^{-3} μ_{IIS} is much higher than other scattering such as μ_{PH}.

It should be stressed that IIS in a nondegenerate regime shows different behavior from those in a degenerate region owing to the change of distribution of carriers from Fermi–Dirac to Maxwell–Boltzmann. For example, μ_{IIS} in the nondegenerate region is written as

$$\mu_{IIS}^{nondeg} \propto T^{\frac{3}{2}}.$$

This behavior has been frequently observed for compound semiconductors such as GaAs and GaN, and was indeed observed for bulk single crystals of dilutely Sb-doped SnO_2 (Fig. 1.9).

Neutral Impurity Scattering

Phonon scattering and IIS are related to host materials and carrier doping, respectively. In other words, these scatterings determine the upper limit of μ_H. Thus, achieving high μ_H is nothing but reducing other scatterings, which are absent from ideal TCOs. Neutral impurity scattering (NIS) [6, 7] is such a typical reducible scattering, which is written as

$$\mu_{NIS} = \frac{m^* e^3}{A\epsilon_0 \epsilon_r \hbar^3 n_N},$$

where A is the cross section enhancement factor and n_N is the density of neutral impurity. Typical neutral impurities are inactive dopants and unintentional impurities such as interstitial neutral H. Apparently, μ_{NIS} contains large uncertainty due to the difficulty associated with precisely determining n_N and the ambiguity associated with the evaluation of A. Thus, quantitative analysis on TCOs films with low doping efficiency is highly challenging.

Grain Boundary Scattering

As reviewed in chapter 1, carrier transport of TCOs in low n_e regime is dominated by grain boundary scattering, which was modeled and formulated by Seto [8]. In the model, μ_H limited by grain boundary (μ_{GB}) is written as

$$\mu_{GB}^{Seto} \propto T^{-\frac{1}{2}} \exp\left(-\frac{\phi}{k_B T}\right),$$

where ϕ is the barrier height. Because the Seto model originally treated transport properties in the nondegenerate regime, Bruneaux et al. [9] formulated μ_{GB} in a degenerate regime as

$$\mu_{GB}^{Brun} \propto T^{-1} \exp\left(-\frac{\phi}{k_B T}\right).$$

Figure A.2 shows simulated μ_H-T curves using Seto and Bruneaux models. It should be noted that such ideal thermal activation behaviors have seldom been observed in experiments. Figure A.3 shows typical μ_H-T curves for SnO_2 and $Sn_{0.95}Ta_{0.05}O_2$ films on glass. Detailed information is given in chapter 3. As discussed in the main text, the dominant role of grain boundary scattering in both films was evidenced by lower μ_H than both optical mobility and μ_H for epitaxial films. Nevertheless, the thermal activation behavior, which is clear evidence for grain boundary limited carrier transport, was not observed for the $Sn_{0.95}Ta_{0.05}O_2$ film. In addition, the decrease in μ_H for the SnO_2 film with

decreasing T was rather gradual, which is inconsistent with the steep decrease in the simulated curves.

One possible way to resolve this inconsistency is to include other mechanisms as parallel circuits in the grain boundary scattering. Reflection [10] and tunneling [11] at the grain boundary have been considered thus far. However, no studies have presented a comprehensive and quantitative analysis on the grain boundary scattering of TCOs thus far.

Dislocation Scattering

In general, dislocation scattering has been ignored in TCOs studies. However, epitaxial growth is the key to enhance μ_H in this study, and therefore I assessed the importance of dislocation scattering. Dislocations are treated as charged line defects and thus show a behavior similar to that of ionized impurity. μ_H limited by dislocation scattering (μ_{DS}) in the nondegenerate regime [12] is written as

$\mu_{DS}^{nondeg} \propto n_e^{\frac{1}{2}}$ and $\mu_{DS}^{nondeg} \propto T^{\frac{3}{2}}$.

A study on undoped SnO_2 epitaxial films reported $\mu_H \propto n_e^{1/2}$ relation [13].

In contrast, dislocation scattering in the degenerate region has been poorly studied. However, some studies [14, 15] insisted that dislocation scattering in the degenerate regime

is independent of T and is rapidly screened by n_e like IIS. μ_{DS} in the nondegenerate regime is written as

$$\mu_{DS}^{Fermi\ gas} \propto n_e^{\frac{7}{6}}.$$

It is noteworthy to point out the similarity of this formula to the BHD formula ($\mu_{IIS} \propto n_e$), and the drastic increase in the exponent from 1/2 to 7/6 owing to enhanced screening in the degenerate regime. Such drastic change in μ_H is not observed for doped epitaxial SnO_2 thin films (Fig. 3.3) at least around $n_e = 1 \times 10^{20}$ cm^{-3}. Therefore, dislocation scattering is supposed to be well screened and thus insignificant in this study.

Concluding Remarks

Quantitative analysis of transport properties of TCOs is extremely challenging due to rather unreliable understandings of some scatterings, and thus beyond the scope of this study. Nevertheless, it is useful to calculate the upper limit of μ_H determined by phonon and IIS, which can be reliably estimated, in order determine the potential to improve μ_H.

References

[1] *Toumeidoudenmaku No Gijutsu* (*Technology of Transparent Conductive Oxide Thin-films*) ed. The 166th Committee on Photonic and Electronic Oxide of the Japan Society for the Promotion of Science (Ohmsha, Tokyo, 2014) 3rd ed. [in Japanese]

[2] *Transparent Conductive Zinc Oxide*, ed. K. Ellmer, A. Klein, and B. Rech (Springer, New York, 2009)

[3] R.B. Dingle, Philos. Mag. **46**, 831 (1955).

[4] M. Feneberg, C. Lidig, K. Lange, M. E. White, M. Y. Tsai, J. S. Speck, O. Bierwagen, and R. Goldhahn, Phys. Status Solidi **A 211**, 82 (2014).

[5] R. Summitt, J. Appl. Phys. **39**, 3762 (1968).

[6] T.C. McGill and R. Baron, Phys. Rev. B **11**, 5208 (1975).

[7] K. Itoh, T. Kinoshita, J. Muto, N. Haegel, W. Walukiewicz, O. Dubon, J. Beeman, and E. Haller, Phys. Rev. B **56**, 1906 (1997).

[8] J.Y.W. Seto, J. Appl. Phys. **46**, 5247 (1975).

[9] J. Bruneaux, H. Cachet, M. Froment, and A. Messad, Thin Solid Films **197**, 129 (1991).

[10] A.F. Mayadas and M. Shatzkes, Phys. Rev. B **1**, 1382 (1970).

[11] D.H. Zhang and H.L. Ma, Appl. Phys. A **62**, 487 (1996).

[12] B. Pödör, Phys. Status Solidi **16**, K167 (1966).

[13] H. Mun, H. Yang, J. Park, C. Ju, and K. Char, APL Mater. **3**, 076107 (2015).

[14] D.C. Look, H. Lu, W.J. Schaff, J. Jasinski, and Z. Liliental-Weber, Appl. Phys. Lett. **80**, 258 (2002).

[15] B. Bansal, R. Ghosh, and V. Venkataraman, J. Appl. Phys. **113**, 163705 (2013).

Appendix B: Enhanced Carrier Generation in Nb-Doped SnO_2 Thin Films Grown on Strain-Inducing Substrates[1]

I report the effect of lattice strain from the substrate on carrier generation in Nb-doped SnO_2 (NTO) transparent conductive oxide (TCO) thin films. The carrier activation efficiency of Nb was strongly affected by in-plane tensile strain, and the NTO films grown on c-Al_2O_3 and anatase TiO_2 seed layers had carrier density (n_e) as high as 3×10^{20} cm^{-3}. In contrast, strain-free NTO films grown on glass exhibited much smaller n_e due to the formation of deep impurity levels. These results imply that NTO has potential as a practical TCO in the presence of substrate-film epitaxial interaction.

Introduction

Doped SnO_2 thin films have been increasing the sustainability of society as a key component in energy-saving or energy conversion technologies, such as coatings for energy-efficient windows and transparent conducting oxide (TCO) electrodes for photovoltaic cells (PVCs). Effective dopants for SnO_2 and practical film fabrication processes suitable for individual dopants have been extensively explored from both fundamental and practical viewpoints. Highly conductive F-doped SnO_2 (FTO) thin films with resistivity (ρ) as low as 3×10^{-4} Ωcm were fabricated by chemical vapor deposition

[1] A version of this chapter has been published in Appl. Phys. Express **5**, 061201 (2012).

(CVD) [1], whereas FTO films deposited by physical vapor deposition (PVD) exhibited relatively high ρ values of $\geq 5 \times 10^{-4}$ Ωcm [2]. Ta-doped SnO_2 (TTO) thin films with $\rho = 3 \times 10^{-4}$ Ωcm were fabricated by both CVD [3] and PVD [4,5,6]. Although TTO shows good conductivity and insensitivity to the deposition technique, the use of a scarce element, Ta, is a significant drawback that limits the application of TTO.

Nb is a sister element to Ta, sharing many of its physical and chemical properties, and is therefore expected to be an effective dopant for SnO_2. Indeed, a first-principles calculation predicted that Nb doping, as well as Ta doping, can generate carriers with high density (n_e) [7]. Contrary to the theoretical prediction, the n_e values attained in Nb-doped SnO_2 (NTO) thin films were less than 6×10^{19} cm^{-3}, resulting in relatively higher ρ on the order of 10^{-3} Ωcm [8,9,10,11]. This is in sharp contrast to the highly effective carrier generation by Ta doping [4,6]. Such low n_e in NTO can be explained by the formation of native donors, such as oxygen vacancies [8]. Therefore, whether Nb serves as a good dopant for SnO_2 is still an open question.

In this study, I compared the transport properties of NTO films deposited on various substrates, including bare glass and single-crystalline Al_2O_3, to examine the effect of lattice strain on carrier generation. As a result, I found that a high n_e value of 3×10^{20} cm^{-3} can be generated by introducing in-plane tensile strain from the substrate. 1 at% Nb-doped SnO_2 films on single-crystalline Al_2O_3 revealed a high activation efficiency of 65%, comparable to that of F-doped SnO_2, demonstrating that Nb can serve as an effective dopant for SnO_2 in the presence of lattice strain.

Experimental

$Sn_{1-x}Nb_xO_2$ (x = 0–0.05) thin films were deposited by PLD using a KrF excimer laser with a repetition rate of 2 Hz and a fluence of 1–2 Jcm^{-2}. The oxygen partial pressure (P_{O2}) and substrate temperature were set to 5×10^{-3} Torr and 600 °C, respectively. The deposition rate was ~0.02 nm per pulse. The thickness of the NTO films was 130 ± 20 nm unless otherwise stated. Bare alkaline-free glass (Corning, 1737), c-plane sapphire Al_2O_3 (0001), and glass coated with 10-nm-thick anatase TiO_2 and 30-nm-thick ZnO seed layers were used as substrates. The procedure for preparing an anatase TiO_2 seed layer has been described in detail elsewhere [9]. A ZnO seed layer [15] was deposited by PLD on an unheated glass substrate at a P_{O2} of 1×10^{-6} Torr. Crystal structures were characterized by X-ray diffraction (XRD). Transport properties, including resistivity (ρ), n_e, and Hall mobility (μ), were measured using a standard six-probe method.

Results and Discussion

Figure B.1 compares XRD patterns of NTO (x = 0.01) thin films deposited on various substrates. Hereafter, NTO films grown on bare glass, Al_2O_3 (0001), the TiO_2 seed layer, and the ZnO seed layer are referred to as NTO/glass, NTO/ALO, NTO/TiO_2, and NTO/ZnO, respectively. As seen from Fig. B.1, NTO/glass is a randomly oriented polycrystalline film, while NTO/ALO has the form of an epitaxial thin film with (100) orientation [3,5]. Both NTO/TiO_2 and NTO/ZnO are (100)-oriented polycrystalline films with random in-plane orientation [6,12].

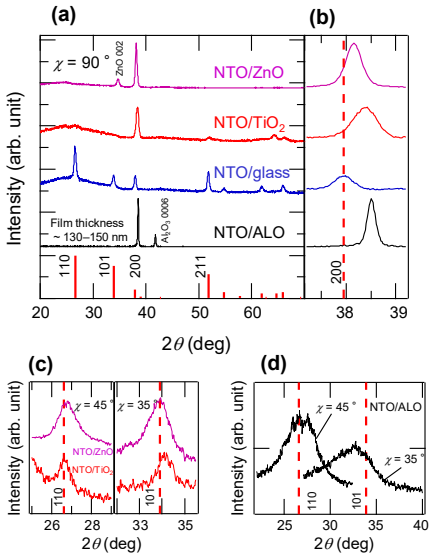

Fig. B.1. (a) XRD patterns obtained at $\chi = 90$ ° and (b) their magnification near the (200) diffraction of NTO/ALO, NTO/glass, NTO/ZnO, and NTO/TiO_2 ($x = 0.01$) films. The bar chart shows the XRD pattern of bulk SnO_2 (JCPDS 41-1445). XRD patterns obtained at various χ of (c) NTO/ZnO, NTO/TiO_2, and (d) NTO/ALO films. The dashed lines denote the position of the bulk diffraction. (Copyright (2012) The Japan Society of Applied Physics)

Table B.I. Structure, lattice parameters, and carrier density, n_e, of the NTO ($x = 0.01$) films.

Sample	Crystal	Lattice parameters				n_e (cm^{-3})
		$a_\perp$ (nm)	$a_{//}$ (nm)	$c_{//}$ (nm)	$a_{//} \times c_{//}$	
JCPDS 41-1445	Bulk	0.4738		0.3187	0.1510	-
NTO/ALO	(100) epi	0.466_7	(0.45_2)	(0.33_9)	(0.15_3)	1.8×10^{20}
NTO/glass	random poly	0.473_0		0.318_1	0.150_4	5.3×10^{19}
NTO/TiO_2	(100) poly	0.468_7	0.479_7	0.317_6	0.152_3	1.9×10^{20}
NTO/ZnO	(100) poly	0.470_8	0.471_6	0.319_3	0.150_5	8.2×10^{19}

(100) epi: (100)-oriented epitaxial film; random poly: randomly oriented polycrystalline film; (100) poly: (100)-oriented polycrystalline film

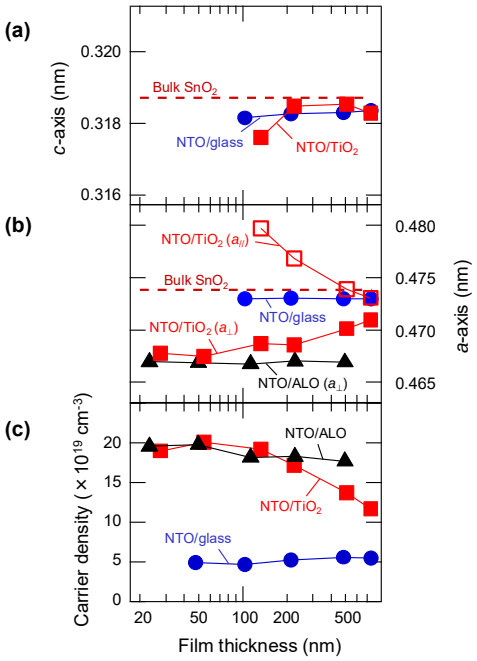

Fig. B.2. Film thickness dependences of (a) *c*-axis and (b) *a*-axis lengths and (c) carrier density (n_e) of NTO/ALO, NTO/glass, and NTO/TiO_2 (x = 0.01) films. The dashed lines denote the lattice parameters for bulk SnO_2. (Copyright (2012) The Japan Society of Applied Physics)

As shown in Fig. B.1(b), the *d*-spacing of (200) of NTO/ALO and NTO/TiO_2, corresponding to the out-of-plane *a*, is much smaller than that of bulk SnO_2 (JCPDS 41-1445), due to the large in-plane lattice mismatch. In contrast, no peak shift was observed for NTO/glass, implying the absence of strain from the amorphous substrate.

The in-plane lattice parameters were determined by the XRD measurements at various χ as shown in Fig. B.1(c) and B.1(d). The out-of-plane *a* ($a_{\perp}$), in-plane *a* ($a_{//}$), $c_{//}$, and $a_{//} \times c_{//}$ lattice parameters of these films together with n_e are summarized in Table B.I. NTO/TiO_2 has a larger $a_{//} \times c_{//}$ than NTO/glass and bulk SnO_2, indicating that NTO/TiO_2 grows under tensile strain from the substrate. Unfortunately, I could not determine the in-plane lattice parameters of NTO/ALO precisely because the in-plane diffraction peaks are substantially broadened, possibly due to the small grain sizes [3]. However, it is reasonable to assume that NTO/ALO, as well as NTO/TiO_2, is subjected to in-plane tensile strain, considering the reduced $a_{\perp}$. Meanwhile, the in-plane tensile strain in NTO/ZnO is less than that in NTO/TiO_2.

Next, I discuss the transport properties of the NTO films. As seen from Table B. I, NTO/glass and NTO/ZnO have relatively low n_e below 1×10^{20} cm^{-3}, whereas NTO/ALO and NTO/TiO_2 exhibit much higher n_e of $\sim 2 \times 10^{20}$ cm^{-3}. The enhanced n_e in NTO/ALO and NTO/TiO_2 results in a significant reduction of ρ, which will be discussed later in more detail. The marked difference in n_e between NTO/(glass or ZnO) and NTO/(ALO or TiO_2) appears to be related to the tensile strains from the substrates. To confirm this, I investigated the film thickness (*t*) dependences of lattice parameters and n_e, as shown in Fig. B.2. The lattice parameters of NTO/glass are close to those for bulk SnO_2, and n_e is

~5 × 10^{19} cm^{-3} in the entire range of t, indicating the absence of epitaxial lattice strain. The $a_{\perp}$ values of NTO/ALO are also independent of t but are clearly smaller than those of NTO/glass. This implies that the epitaxial strain is not relaxed, at least up to t = 500 nm. Although n_e for NTO/ALO is a slightly decreasing function of t, it is in the range of 1.8–2.0 × 10^{20} cm^{-3}. In sharp contrast, NTO/TiO_2 exhibits a significant increase in $a_{\perp}$ and decrease in $a_{//}$ with increasing t toward the values for NTO/glass. This behavior indicates that in NTO/TiO_2, the strain induced by the 10-nm-thick TiO_2 seed layer is relaxed at larger t. Notably, n_e for NTO/TiO_2 is rapidly decreased at t > 200 nm in synchrony with the relaxation. These results prove that lattice strain assists carrier generation in NTO.

Figures B.3(a)–B.3(c) plot the transport properties of NTO/glass, NTO/ALO, and NTO/TiO_2 at room temperature (RT) as a function of Nb concentration, x. For NTO/glass, ρ is on the order of 10^{-3} Ωcm, similar to the values in previous reports [8,9,10,11]. On the other hand, a much lower ρ of < 1 × 10^{-3} Ωcm was obtained for NTO/ALO and NTO/TiO_2. In particular, NTO/TiO_2 (x = 0.01–0.02) exhibits the lowest ρ value of ~5 × 10^{-4} Ωcm, which is comparable to those for FTO [2] and Sb-doped SnO_2 films [13] grown by PLD. Such a low ρ on the order of 10^{-4} Ωcm for NTO/ALO and NTO/TiO_2 is attributable to a substantial increase in n_e, as shown in Fig. B.3(b). For NTO/glass, the n_e – x curve is bell-shaped with a maximum of ~5 × 10^{19} cm^{-3} at x = 0.015, as reported for sputter-deposited films [8]. Meanwhile, n_e for NTO/ALO and NTO/TiO_2 increases with increasing x up to 3 × 10^{20} cm^{-3}. The activation efficiency in the lightly doped region ($x \leq 0.01$) is higher than 65%, which is comparable to that of FTO of ~80% [14]. These results demonstrate that Nb is an effective dopant for SnO_2.

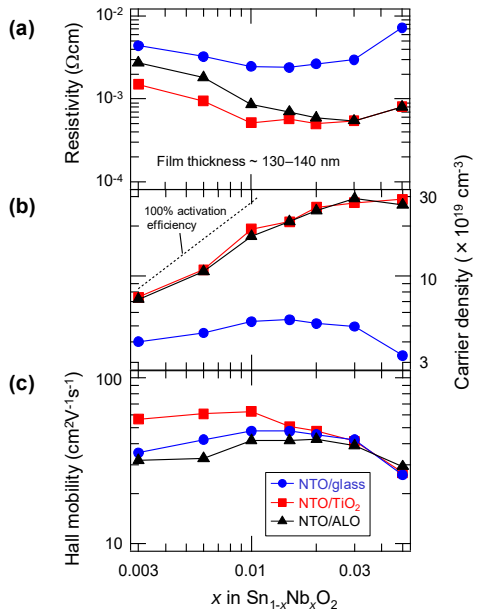

Fig. B.3. (a) Resistivity, ρ, (b) n_e, and (c) Hall mobility, μ, of NTO/glass (circles), NTO/TiO_2 (squares), and NTO/ALO (triangles) films as a function of Nb content, x, in $Sn_{1-x}Nb_xO_2$. The dashed line represents the carrier density calculated assuming that the activation efficiency is 100%, i.e., each Nb^{5+} ion substituted for a Sn^{4+} site generates one conduction electron. (Copyright (2012) The Japan Society of Applied Physics)

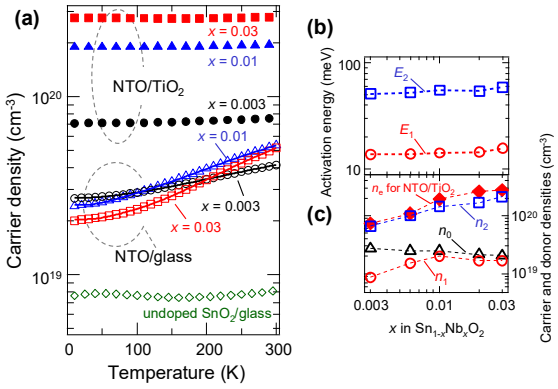

Fig. B.4. (a) Temperature dependences of n_e for NTO/glass (open symbols) and NTO/TiO_2 (closed symbols) films. The solid curves are the results of simulation assuming eq. (1). (b) Activation energies (E_1 and E_2) and (c) carrier density (n_0) and donor densities (n_1 and n_2) obtained from the curve fitting. n_e for NTO/TiO_2 is also plotted in (c) for comparison. (Copyright (2012) The Japan Society of Applied Physics)

Finally, I discuss the origin of the low n_e in NTO/glass. Figure B.4(a) shows the temperature (T) dependence of n_e measured for NTO/glass and NTO/TiO_2. The $n_e(T)$ curves exhibit characteristic features that depend on the substrate: NTO/TiO_2 is characterized by an almost T-independent $n_e(T)$, indicative of a degenerate semiconductor, whereas $n_e(T)$ for NTO/glass shows thermal-activation-type behavior. I analyzed $n_e(T)$ for NTO/glass by fitting the following empirical formula, taking donor levels 1 and 2 into account:

$$n_e(T) = n_0 + n_1\exp[-E_1/(k_BT)] + n_2\exp[-E_2/(k_BT)],$$

where n_0 corresponds to the degenerate carrier density, n_1 and n_2 are the donor densities, E_1 and E_2 ($E_1 < E_2$) are the activation energies, and k_B is the Boltzmann constant. The obtained donor density and energy parameters, together with n_e at RT for NTO/TiO_2, are plotted against x in Figs. B.4(b) and B.4(c). Remarkably, n_2 coincides very well with n_e for NTO/TiO_2 and is almost proportional to x. This implies that carriers are supplied by an impurity level located at $E_2 \sim 50$ meV below the bottom of the conduction band. Moreover, such a high donor density of up to $\sim 2 \times 10^{20}$ cm^{-3} is hardly achievable by native donors. Indeed, the concentration of unintentional dopants (e.g., oxygen vacancies and cation impurities such as Sb) is estimated to be less than 1×10^{19} cm^{-3} from the $n_e(T)$ curve of the undoped SnO_2/glass film. Therefore, I concluded that the high values of n_2 originate from doped Nb. E_2 is almost independent of x and much higher than k_BT at RT, resulting in the severe reduction of n_e(RT) for NTO/glass compared with n_e for NTO/TiO_2. At present, the physics behind the dramatic effect of in-plane tensile strain on the carrier generation of NTO remains unclear. One speculation is that under in-plane tensile strain, Nb atoms are incorporated into lattice sites that are favorable for releasing electrons. Further

experimental and theoretical studies are required to elucidate the detailed carrier generation mechanism in NTO. Stimulated by this work, Behtash *et al.* [19] reported localized impurity state in NTO by using the first principles calculation. However, the role of strain still remains unexplained.

Summary

I have studied the effect of lattice strain on the carrier generation in NTO thin films. The NTO films subjected to tensile lattice strain from substrates, i.e., NTO/ALO and NTO/TiO_2 films, were found to exhibit n_e as high as 3×10^{20} cm^{-3}, indicating that Nb can be an effective dopant for SnO_2. On the other hand, NTO/glass films had a reduced n_e of 5×10^{19} cm^{-3} due to the formation of a 50-meV-deep Nb donor level. These results demonstrate that the activation of dopants in SnO_2 is controllable by adjusting the substrate-induced lattice strain.

References

[1] D. S. Ginley and C. Bright, Mater. Res. Soc. Bull. **25**, 15 (2000).

[2] E. Fortunato, D. Ginley, H. Hosono, and D. C. Paine, Mater. Res. Soc. Bull. **32**, 242 (2007).

[3] T. Ishida, O. Tabata, J. I. Park, S. H. Shin, H. Magara, S. Tamura, S. Mochizuki, and T. Mihara, Thin Solid Films **281-282**, 228 (1996).

[4] H. Kim, R. C. Y. Auyeung, and A. Piqué, Thin Solid Films **516**, 5052 (2008).

[5] S. W. Lee, Y.-W. Kim, and H. Chen, Appl. Phys. Lett. **78**, 350 (2001).

[6] Y.-W. Kim, S. W. Lee, and H. Chen, Thin Solid Films **405**, 256 (2002).

[7] H. Toyosaki, M. Kawasaki, and Y. Tokura, Appl. Phys. Lett. **93**, 132109 (2008).

[8] S. Nakao, N. Yamada, T. Hitosugi, Y. Hirose, T. Shimada, and T. Hasegawa, Thin Solid Films **518**, 3093 (2010).

[9] S. Nakao, N. Yamada, T. Hitosugi, Y. Hirose, T. Shimada, and T. Hasegawa, Appl. Phys. Express **3**, 031102 (2010).

[10] V. M. Zainullina, Physica B **391**, 280 (2007).

[11] N. Kikuchi, E. Kusano, E. Kishio, and A. Kinbara, Vacuum **66,** 365 (2002).

[12] Y. J. Seo, G. W. Kim, C. H. Sung, M. S. Anwar, C. G. Lee, and B. H. Koo, Curr. Appl. Phys. **11**, S310 (2011).

[13] A. Yoshie Suzuki, K. Nose, A. Ueno, M. Kamiko, and Y. Mitsuda, Appl. Phys. Express **5**, 011103 (2012).

[14] V. Gokulakrishnan, S. Parthiban, K. Jeganathan, and K. Ramamurthi, J. Mater. Sci. **46**, 5553 (2011).

[15] K. Kato, P. K. Song, H. Odaka, and Y. Shigesato, Jpn. J. Appl. Phys. **42**, 6523 (2003).

[16] H. Kim and A. Piqué, Appl. Phys. Lett. **84**, 218 (2004).

[17] C.-C. Lin, M.-C. Chiang, and Y.-W. Chen, Thin Solid Films **518**, 1241 (2009).

[18] R. Saniz, H. Dixit, D. Lamoen, and B. Partoens, Appl. Phys. Lett. **97,** 261901 (2010).

[19] M. Behtash, P.H. Joo, S. Nazir, and K. Yang, J. Appl. Phys. **117**, 175101 (2015).

Appendix C: Carrier Generation Mechanism and Effect of Ta-Doping in Transparent Conductive Amorphous SnO_2 Thin Films[1]

I investigated the transport properties of amorphous undoped and Ta-doped SnO_2 thin films grown on unheated glass substrates by pulsed laser deposition. Optimized films exhibited a resistivity of 2×10^{-3} Ωcm, carrier density (n_e) of (1-2) $\times 10^{20}$ cm^{-3}, and were highly transparent in the visible region. Ta-doping had little effect on n_e in amorphous films, in contrast to in crystalline phases. These results suggest that carrier electrons in amorphous SnO_2 films originated from oxygen vacancies, similar to in In_2O_3-based amorphous films.

Introduction

Degenerately doped wide-bandgap oxide semiconductors, or transparent conducting oxides (TCOs), have received much recent attention. They have applications as transparent electrodes in optoelectronic devices including solar cells, flat panel displays and light emitting diodes [1,2]. Amorphous TCOs deposited on unheated substrates have a low process cost, excellent surface flatness, favorable etching properties and compatibility with plastic substrates [3]. Amorphous In_2O_3-based thin films are TCOs that exhibit high

[1] A version of this chapter has been published in Jpn. J. Appl. Phys. **53**, 05FX04 (2014).

conductivity and transparency, comparable to that of crystalline counterparts, and have been widely studied [3,4,5,6,7]. Carriers in amorphous In_2O_3-based films have been shown to release from oxygen vacancies, while substitutional cation-doping provides carriers in crystalline In_2O_3 films [4,5,6,7]. This is in contrast to carrier-generation in amorphous Si, where cation-substitution remains an effective way of introducing carriers [8]. This difference is because of the covalency/ionicity of the chemical bonds in these materials [6]. Bonds in oxides are more ionic, and are thus sufficiently flexible to allow slight changes in the coordination structure. This reduces the efficiency of carrier generation associated with cation substitution [6]. Carrier electrons have been shown to originate from oxygen vacancies in amorphous In_2O_3 [4,9].

Herein, I focus on SnO_2-based amorphous TCOs. These have several practical advantages over In_2O_3-based TCOs, including higher chemical stability, lower material cost and lower toxicity. SnO_2 thin films on unheated substrates have been reported by deposition from sputtering [10,11,12,13,14,15], reactive vacuum evaporation (RVE) [16] and filtered vacuum arc deposition (FVAD) [17] as summarized in Table I. Crystallization in sputtered SnO_2 films is frequently observed, even on unheated substrates [11,12,15]. This suggests the impact of high-energy particles, such as recoiled Ar and accelerated O ions, triggers crystallization, or that substrate temperature is unintentionally raised by up to several tens of °C during deposition [18,19]. Kim *et al.* recently reported sputtered undoped SnO_2 thin films exhibiting resistivity (ρ) as low as 3×10^{-3} Ωcm, even in an as-deposited amorphous state, using reduced RF power [13]. In such highly conducting amorphous undoped SnO_2 films, carrier electrons are supplied by O vacancies [13,17], whereas the

carrier doping efficiency through cation substitution in amorphous SnO_2 remains unclear. Kaplan *et al.* fabricated amorphous undoped and Sb-substituted SnO_2 thin films using FVAD, and found that conductivity was insensitive to Sb-substitution [17]. However, the relationship between carriers and Sb substitution was not conclusively demonstrated, because the possibility of Sb evaporating during deposition could not be excluded [17].

In this study, carrier generation in amorphous SnO_2 is investigated, by substituting cation sites with nonvolatile Ta. This can generate carriers in crystalline SnO_2 films [20,21,22]. Pulsed laser deposition (PLD) is employed to fabricate amorphous films. The deposition flux energy is similar to that in sputtering [23], but PLD does not involve bombardment of high energy particles. The unintentional heating of substrates is much less than in sputtering (discussed later). These features favor the growth of amorphous SnO_2 films, and conducting amorphous Ta-doped SnO_2 thin films with ρ of 2×10^{-3} Ωcm were obtained. Carrier concentration was relatively insensitive to Ta content, indicating that the carrier generation mechanism in amorphous SnO_2 is similar to that in amorphous In_2O_3.

Experimental

$Sn_{1-x}Ta_xO_2$ (TTO) thin films with x = 0-0.03 were deposited by PLD on alkaline-free glass and fused silica substrates, without intentional heating. The substrate temperature during deposition was confirmed to be < 50 °C, using a nonreversible temperature indicator (Nichiyu Giken Kogyo, Thermo Label). Sintered pellets of $Sn_{1-x}Ta_xO_2$ were used as PLD targets. The O partial pressure during deposition (P_{O2}) was 5×10^{-3}-1×10^{-1} Torr. A KrF excimer laser with repetition rate of 2 Hz and laser fluence of 1-2 J/cm^2 was used for

ablation. The typical film thickness was 100-160 nm. Crystal structures were evaluated by X-ray diffraction (XRD), using a four-axis diffractometer and two-dimensional area detector. Surface morphologies were characterized by atomic force microscopy (AFM). Transport properties including ρ, carrier density (n_e) and Hall mobility (μ) were measured at room temperature, using the six probe method with standard Hall bar geometry. Films grown on fused silica substrates were used for optical measurements. Transmittance (T) and reflectance (R) spectra were measured over the 220–2200 nm region, using a UV-visible-near-infrared spectrophotometer. Absorption (A) spectra were calculated as $A = 1 - T - R$. Absorption coefficients (α) were calculated as $\alpha = 1/d \times \ln[(1 - R)/T]$, where d is the film thickness [24,25].

Results and Discussion

The structural properties of TTO films were first investigated. Figure C.1(a) shows typical XRD patterns of $Sn_{0.99}Ta_{0.01}O_2$ films deposited at various P_{O2}. No diffraction peaks were observed, indicating amorphous growth. Diffraction peaks were absent from the XRD patterns of all the films fabricated in this study. Figures C.1(b) and C.1(c) show AFM images of amorphous $Sn_{0.99}Ta_{0.01}O_2$ films, deposited at O poor ($P_{O2} = 5 \times 10^{-3}$ Torr) and optimal O ($P_{O2} = 2.5 \times 10^{-2}$ Torr) conditions. Both images show extremely flat surfaces, characteristic of amorphous films. Root mean square roughness (R_{rms}) values were 2.6×10^{-1} and 3.7×10^{-1} nm, for Figs. C.1(b) and C.1(c), respectively.

Table C. I. Structures and transport properties of SnO_2 thin films deposited on unheated substrates by various techniques.

Deposition technique	Doping	Structure	Resistivity (Ωcm)	Carrier density (cm^{-3})	Reference
RFMS	Undoped	N.A.	3.2×10^{-3}	1.2×10^{20}	10
RFMS	Undoped	Polycrystalline	1.9×10^{-3}	1.6×10^{20}	11
RFMS	Undoped	Polycrystalline	3×10^{-3}	1×10^{20}	12
RFMS	Undoped	Amorphous	3×10^{-3}	1×10^{20}	13
DCMS	Ta-doped	N.A.	3×10^{-2}	3×10^{19}	14
DCRMS	Ta-doped	Polycrystalline or amorphous	1×10^{-2}	1×10^{20}	15
RVE	Undoped	Amorphous	N.A.	N.A.	16
FVAD	Sb-doped	Amorphous	1×10^{-3}	N.A.	17
PLD	Ta-doped	Amorphous	2×10^{-3}	$1\text{-}2 \times 10^{20}$	This work

RFMS: RF magnetron sputtering, DCMS: DC magnetron sputtering, DCRMS: DC reactive magnetron sputtering, N.A.: not available

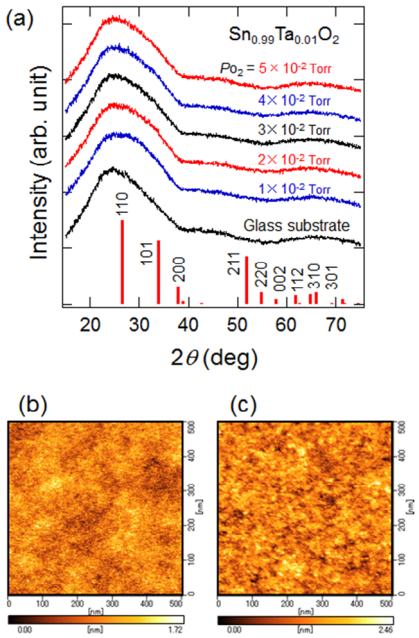

Fig. C.1. (a) XRD patterns of $Sn_{0.99}Ta_{0.01}O_2$ films on unheated glass substrates. The bar chart shows the XRD pattern of bulk SnO_2 (JCPDS 41-1445). AFM images of $Sn_{0.99}Ta_{0.01}O_2$ films deposited at (b) 5 × 10^{-3} and (c) 2.5 × 10^{-2} Torr. (Copyright (2014) The Japan Society of Applied Physics)

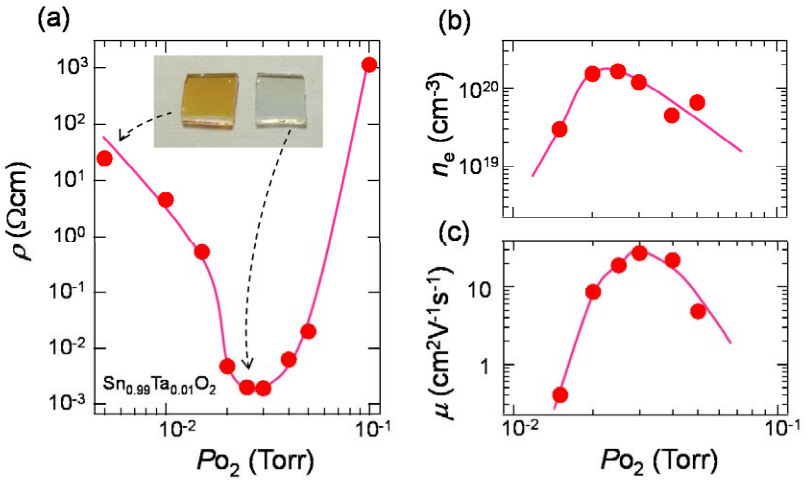

Fig. C.2. (a) ρ, (b) n_e, and (c) μ of amorphous $Sn_{0.99}Ta_{0.01}O_2$ films. Solid curves are guides to illustrate trends. The inset in (a) shows a photographic image of typical films deposited in O poor and optimal O conditions. (Copyright (2014) The Japan Society of Applied Physics)

Slight increases in R_{rms} with increasing P_{O2} may have resulted from an enhanced shadowing effect, i.e. the scattering of deposition flux by the process gas [26].

The transport properties of amorphous $Sn_{0.99}Ta_{0.01}O_2$ films were then investigated. As shown in Fig. C.2(a), films deposited in O poor conditions exhibited high ρ values. The insulating films were of a yellowish color, as seen from the photographic image inset in Fig. C.2(a). Similar yellow coloration and low conductivity have been widely reported for SnO_2 films deposited in O poor conditions by physical vapor deposition, including sputtering [10], RVE [16], FVAD [17] and pulsed plasma deposition [27]. This behavior is explained by the local formation of p-type SnO in O poor atmospheres [28]. With increasing P_{O2}, films become transparent and conductive with n-type carriers. The lowest ρ of 1.9×10^{-3} Ωcm ($n_e = 1.2 \times 10^{20}$ cm^{-3}, $\mu = 27$ cm^{2}V^{-1}s^{-1}) was achieved at $P_{O2} = 3 \times 10^{-2}$ Torr, whereas n_e reached a maximum of 1.7×10^{20} cm^{-3} at slightly O poor conditions of $P_{O2} = 2.5 \times 10^{-2}$ Torr. These transport properties are in good agreement with those previously reported in sputtering [13] and FVAD [17] studies. The highest μ of 27 cm^{2}V^{-1}s^{-1} is comparable to that of polycrystalline films on glass substrates deposited by PLD at 600 °C (32 cm^{2}V^{-1}s^{-1}) [22]. This demonstrates the potential of amorphous SnO_2 as TCOs.

To gain insight into carrier generation in amorphous TTO films, the effect of Ta-doping on n_e was investigated. Figure C.3 shows n_e of amorphous $Sn_{1-x}Ta_xO_2$ films deposited at $P_{O2} = 2.5 \times 10^{-2}$ Torr plotted as a function of x. The figure includes the n_e vs x relationship of polycrystalline films for comparison [22]. n_e values of amorphous films were almost independent of x. n_e values of polycrystalline films systematically increased with increasing x, demonstrating the effective carrier generation by Ta-doping.

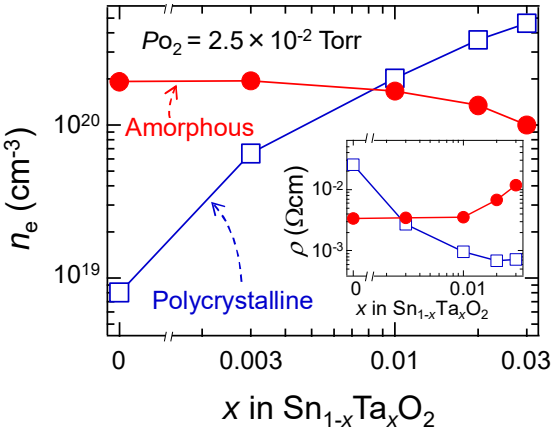

Fig. C.3. Ta concentration (x) dependence of n_e in amorphous (circles) and polycrystalline (squares) $Sn_{1-x}Ta_xO_2$ films. Data for polycrystalline films are from ref. 22. The inset shows x dependence of ρ. (Copyright (2014) The Japan Society of Applied Physics)

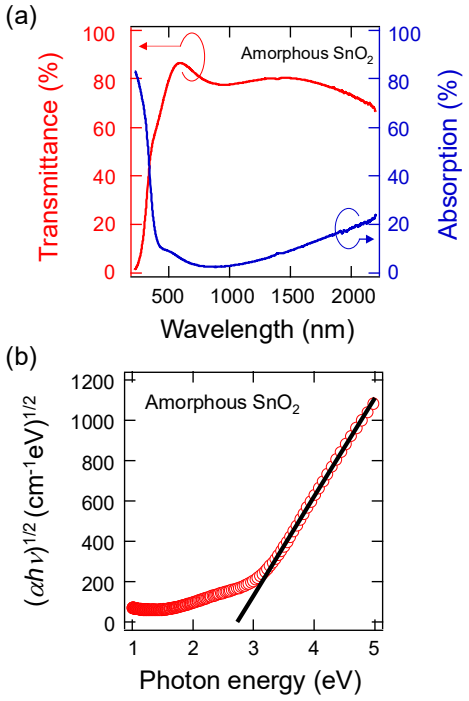

Fig. C.4. (a) T and A spectra of an amorphous SnO_2 film. (b) $(\alpha h\nu)1/2$ as a function of photon energy for the amorphous SnO_2 film. The linear extrapolation was used to determine the optical bandgap. (Copyright (2014) The Japan Society of Applied Physics)

This strongly suggests that carrier electrons in amorphous SnO_2 films originate from O vacancies, similar to in In_2O_3-based amorphous TCOs. As shown in the inset of Fig. C.3, ρ gradually increased with the increase of x due to enhanced impurity scattering. Similar ρ behavior has been observed in Sb-doped SnO_2 [17], suggesting that cation doping cannot provide free carriers in amorphous SnO_2. The maximum n_e value in amorphous SnO_2 films (~2×10^{20} cm^{-3}) is somewhat lower than those in In_2O_3-based amorphous TCOs (~6×10^{20} cm^{-3}) [7]. Excess O vacancies formed in the O poor conditions are speculated to have caused a coordination transformation from SnO_2-like octahedral to SnO-like square-pyramidal. The SnO-like local structure may generate p-type carriers, which annul n-type carriers of SnO_2, resulting in the limited n_e.

The optical properties of highly conductive amorphous SnO_2 were finally investigated. Figure C.4(a) shows T and A spectra of an amorphous undoped SnO_2 thin film ($\rho = 1.9 \times 10^{-3}$ Ωcm, $n_e = 2.2 \times 10^{20}$ cm^{-3}), deposited at $P_{O2} = 3 \times 10^{-2}$ Torr. The film was characterized by in-gap absorption in the visible region, and free carrier absorption in near infrared region. The film exhibited a high average T of 80% across the 400~800 nm region. Similar optical properties were confirmed for TTO films. To determine the optical bandgap of the amorphous SnO_2 films, I adopted the $(\alpha h\nu)^{1/2}$ versus $h\nu$ plot, which has been widely used for amorphous TCOs [29]. As shown in Fig. C.4(b), the optical bandgap of the amorphous SnO_2 film was determined as 2.7 eV, by extrapolating the linear section to $(\alpha h\nu)^{1/2} = 0$. Atomically flat amorphous SnO_2 films with such high transparency and conductivity are promising candidates for transparent electrodes in organic light emitting diodes. For this purpose, further improvement of conductivity is highly desirable. Post-

deposition annealing below crystallization temperature may lead to increases of μ and thus conductivity [13,17].

Summary

TTO thin films were fabricated on unheated glass substrates by PLD, and their structural, transport and optical properties were investigated. TTO films were amorphous with very flat surfaces. Films deposited at low P_{O2} were yellow and insulating. With increasing P_{O2}, films became transparent and conductive with n-type carriers. An optimized film exhibited ρ of 1.9×10^{-3} Ωcm ($n_e = 1.2 \times 10^{20}$ cm^{-3}, $\mu = 27$ $cm^2V^{-1}s^{-1}$). The highest observed μ is comparable to that of polycrystalline films deposited at 600 °C, suggesting the potential of amorphous TTO as a TCO. Unlike in crystalline phases, Ta-doping had little effect on n_e of the amorphous films. Therefore, electrons in amorphous TTO films originated from O vacancies, similar to in In_2O_3-based amorphous TCOs. The maximum n_e of amorphous TTO films of $\sim 2 \times 10^{20}$ cm^{-3} is considerably lower than those of In_2O_3-based amorphous TCOs ($\sim 6 \times 10^{20}$ cm^{-3}). The amorphous SnO_2 film with ρ of 2×10^{-3} Ωcm exhibited an averaged T of 80% in the visible light region, and an optical gap of 2.7 eV.

References

[1] K. Ellmer, Nat. Photonics **6,** 809 (2012).

[2] D.S. Ginley and C. Bright: MRS Bull. **25,** 15 (2000).

[3] H. Hosono: in *Handbook of Transparent Conductors*, ed. D. S. Ginley (Springer, New York, 2010), p.474.

[4] B. Yaglioglu, Y. J. Huang, H. Y. Yeom, and D.C. Paine: Thin Solid Films **496,** 89 (2006).

[5] J. R. Bellingham, A. P. Mackenzie, and W. A. Phillips: Appl. Phys. Lett. **58,** 2506 (1991).

[6] H. Hosono: J. Non-Cryst. Solids **352,** 851 (2006).

[7] A. Leenheer, J. Perkins, M. van Hest, J. Berry, R. O'Hayre, and D. Ginley: Phys. Rev. B **77,** 115215 (2008).

[8] W. E. Spear and P. G. Le Comber: Solid State Commun. **17,** 1193 (1975).

[9] S. Lee, and D. C. Paine: Appl. Phys. Lett. **102,** 052101 (2013).

[10] R. G. Goodchild, J. B. Webb, and D. F. Williams: J. Appl. Phys. **57,** 2308 (1985).

[11] T. Minami, H. Nanto, and S. Takata: Jpn. J. Appl. Phys. **27,** L287 (1988).

[12] B. Stjerna and C. G. Granqvist, Appl. Phys. Lett. **57,** 1989 (1990).

[13] I. H. Kim, J. H. Ko, D. Kim, K. S. Lee, T. S. Lee, J. H. Jeong, B. Cheong, Y. J. Baik, and W. M. Kim: Thin Solid Films **515,** 2475 (2006).

[14] Y. Mihara, R. Satoh, R. Usui, E. Morinaga, and Y. Iwata: SID Symp. Dig. Tech. Pap. **38,** 399 (2007).

[15] Y. Muto, S. Nakatomi, N. Oka, Y. Iwabuchi, H. Kotsubo, and Y. Shigesato: Thin Solid Films **520,** 3746 (2012).

[16] S. Muranaka, Y. Bando, and T. Takada: Thin Solid Films **86,** 11 (1981).

[17] L. Kaplan, R. L. Boxman, S. Goldsmith, U. Rosenberg, and M. Nathan: Thin Solid Films **253,** 1 (1994).

[18] S. Ben Amor, B. Rogier, G. Baud, M. Jacquet, and M. Nardin: Mater. Sci. Eng. B **57,** 28 (1998).

[19] A. Kinbara: in *Sputtering Jitsumu Q&A shu* (*Q&As in Practical Sputtering*), ed. N. Fujimoto (Technical Information Institute, Tokyo, 2009) p. 35 [in Japanese].

[20] H. Toyosaki, M. Kawasaki, and Y. Tokura: Appl. Phys. Lett. **93,** 132109 (2008).

[21] S. Nakao, N. Yamada, T. Hitosugi, Y. Hirose, T. Shimada, and T. Hasegawa: Thin Solid Films **518,** 3093 (2010).

[22] S. Nakao, N. Yamada, T. Hitosugi, Y. Hirose, T. Shimada, and T. Hasegawa: Appl. Phys. Express **3,** 031102 (2010).

[23] G. K. Hubler: in *Pulsed Laser Deposition of Thin Films*, ed. D. B. Chrisey and G. K. Hubler (Wiley, New York, 1994), p.327.

[24] Y. Hishikawa, N. Nakamura, S. Tsuda, S. Nakano, Y. Kishi, and Y. Kuwano: Jpn. J. Appl. Phys. **30,** 1008 (1991).

[25] T. Yamamoto, H. Song, and H. Makino: Phys. Status Solidi C **10,** 603 (2013).

[26] J. A.Thornton: J. Vac. Sci. Technol. **A 4,** 3059 (1986).

[27] Y. Huang, Q. Zhang, and G. Li: Semicond. Sci. Technol. **24,** 015003 (2009).

[28] H. Luo, L.Y. Liang, H.T. Cao, Z.M. Liu, and F. Zhuge: ACS Appl. Mater. Interfaces **4,** 5673 (2012).

[29] H. Hosono, M. Yasukawa, and H. Kawazoe: J. Non-Cryst. Solids **203,** 334 (1996).

Appendix D: Effects of Post-deposition Annealing on Transport Properties of Undoped and Ta-Doped SnO_2 Thin Films: Insights into Intrinsic Defects and Sensing Properties

I investigated the effect of post-deposition annealing on the transport properties of undoped and Ta-doped SnO_2 thin films in order to obtain insights into intrinsic defects and sensing properties of SnO_2 films. Undoped SnO_2 films with carrier density (n_e) of approximately 10^{19} cm^{-3} showed slight decrease in n_e after annealing in air at 600 ºC. This result is consistent with negligibly slow oxygen diffusion in bulk SnO_2 at this temperature. Ta-doped SnO_2 films showed decrease in n_e of 5×10^{19} cm^{-3} with annealing not only in air but also in vacuum. The insensitiveness to annealing atmosphere suggests that the decrease in n_e is unassociated with oxygen vacancies. Reversible decrease in conductivity was observed in air above 400 ºC. Highly suppressed response was observed in epitaxial Ta-doped SnO_2 films, suggesting that the response was derived from reversible adsorption of molecules at grain boundary of the films.

Introduction

High values of carrier density (n_e) for transparent conductive oxides (TCOs) are achieved by extrinsic doping; ideally, undoped host materials such as ZnO, TiO_2, In_2O_3,

and SnO_2 should be highly insulating. Nevertheless, nominally undoped films sometimes show high n_e values [1,2] even on the order of 10^{21} cm^{-3} [3] due to unintentional dopants, or intrinsic defects. The source of such high n_e in unintentionally doped films is still a matter of debate at present. Although some researchers put stress on possible carrier generation by impurity H [4,5] and interstitial cations, oxygen vacancies are generally regarded as the source of high n_e in undoped films. In addition to the important role in undoped materials, oxygen non-stoichiometry plays a critical role even in extrinsically doped TCOs. For example, achieving high conductivity in TCOs frequently requires optimized introduction of process oxygen. Oxygen rich TCOs often show reduced doping efficiencies due to carrier compensation by excess oxygen. On the other hand, oxygen poor TCOs generally show reduced mobility (μ_H) mainly due to inferior crystallinity. Moreover, doubly charged oxygen vacancies show half of μ_H compared with singly charged extrinsic dopants for the same n_e (see appendix A). The n_e values for the oxygen poor TCOs are nonsystematic due to competition of n_e from oxygen vacancies and reduced doping efficiency because of inferior crystallinity.

Post-deposition annealing is another example that clearly demonstrates the importance of oxygen non-stoichiometry in extrinsically doped TCOs [6]. This method affects crystallinity less severely than process oxygen tuning [7] and is therefore suitable for studies on the intrinsic defects associated with oxygen non-stoichiometry. In addition to the motivation in basic science as mentioned above, post-deposition annealing on TCOs has been extensively studied for practical reasons. For example, high substrate temperature is usually unavailable for large scale sputtering. Instead of substrate heating during deposition,

post deposition annealing in air is frequently performed. Some applications such as dye-sensitized photovoltaics require high temperature process in air without reducing conductivity of TCOs. It is well established that TiO_2-based TCOs are very fragile to air-annealing; complete carrier compensation by excess oxygen was observed for both epitaxial [8] and polycrystalline [6] films. ZnO-based TCOs as well shows loss of conductivity due to air-annealing [1,9,10]. In contrast, In_2O_3-based TCOs retained rather high n_e values even after air-annealing probably because of limited incorporation of excess oxygen [11]. SnO_2-based TCOs are so robust against air-annealing [12] that it was used as protective coating for high temperature use in air [13]. No studies, however, investigated post-deposition annealing effects on SnO_2 in detail.

In this appendix, I investigated the effect of post-deposition annealing on the transport properties of undoped and Ta-doped SnO_2 (TTO) thin films in order to obtain insights into intrinsic defects of SnO_2 films.

Experimental

Undoped SnO_2 and TTO films used in chapter 3 and 5 were subjected to post deposition annealing in this study. A rapid thermal annealing furnace (Ulvac-Riko, MILA-3000-pn) equipped with four electrical leads was used to measure resistivity (ρ) in-situ during annealing. Au wires annealed in air at 800 ^{o}C were directly attached to the films using Ag paste (Dupont, 4922N). The furnace was evacuated to the base pressure of 10^{-2} Pa

by using a turbo molecular pump for annealing in vacuum. Ramping rate of the temperature was 3 °C/min and annealing duration at the highest temperature of 600 °C was 1 h.

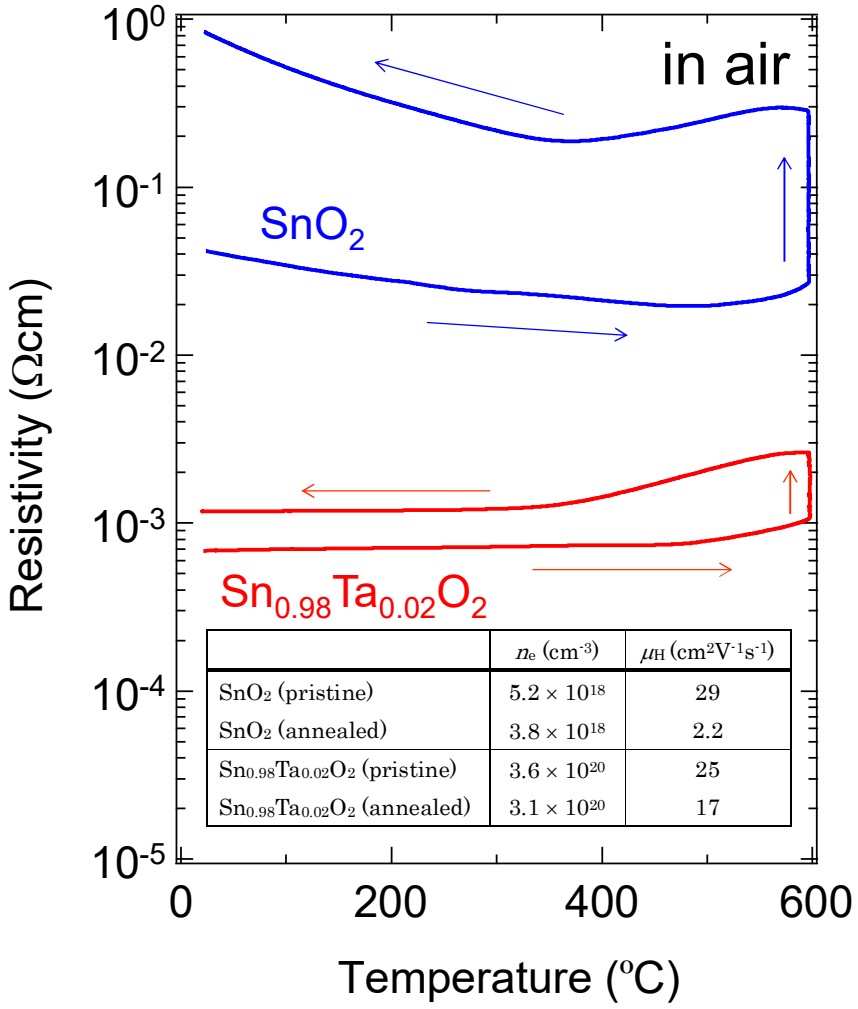

	n_e (cm^{-3})	μ_H (cm^{2}V^{-1}s^{-1})
SnO_2 (pristine)	5.2×10^{18}	29
SnO_2 (annealed)	3.8×10^{18}	2.2
$Sn_{0.98}Ta_{0.02}O_2$ (pristine)	3.6×10^{20}	25
$Sn_{0.98}Ta_{0.02}O_2$ (annealed)	3.1×10^{20}	17

Fig. D.1. In-situ monitoring of resistivity (ρ) for undoped SnO_2 and $Sn_{0.98}Ta_{0.02}O_2$ films grown on glass substrates in air. The inset shows the transport properties of the films

Results and Discussion

Figure D.1 shows ρ for undoped SnO_2 and TTO films grown on glass substrates at elevated temperatures in air. Transport properties (n_e and μ_H) before and after annealing were summarized in the inset of Fig. D.1. Air-annealing resulted in increased ρ mainly due to decreased μ_H, which is probably due to increased grain boundary scattering, in both undoped and doped films. The decrease in n_e is, however, much smaller than those in other TCOs annealed at conditions similar to this study. This result indicates that carrier compensation due to excess oxygen and annihilation of oxygen vacancies are much insignificant in SnO_2 compared with other TCOs, at least below 600 ^oC in air. A gravimetric study on bulk SnO_2 [14] revealed that oxygen non-stoichiometry below 900 ^oC is caused by adsorbed oxygen whereas oxygen vacancies are formed above 1000 ^oC. The report is consistent with the present study, in which possible oxygen vacancies were insensitive to air-annealing. The undoped SnO_2 (99.9% purity) target used in the present study contained 0.01~0.02% Sb ($3–6 \times 10^{18}$ cm^{-3}) in the starting powder. Because the impurity Sb might be the source of the n_e ($5 \times 10^{18}–2 \times 10^{19}$ cm^{-3}) in this study, I fabricated undoped films with a commercial SnO_2 (99.99% purity) target for comparison. Major impurity of the target was not Sb but Pb. The films from the high purity target showed conductivity similar to the undoped films with the 99.9% pure target, suggesting that impurity Sb plays minor role in this study.

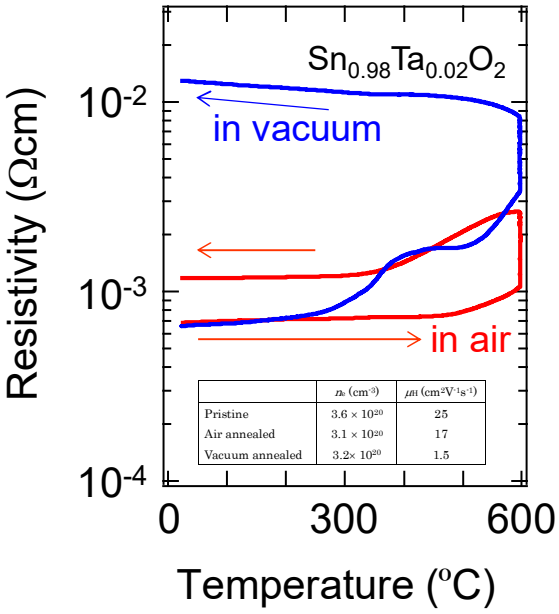

Fig. D.2. In-situ monitoring of ρ for $Sn_{0.98}Ta_{0.02}O_2$ films grown on glass substrates in air and vacuum. The inset shows the transport properties of the films

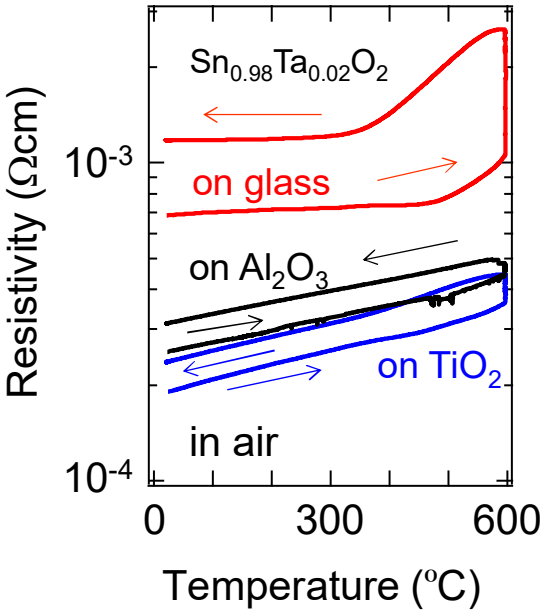

Fig. D.3. In-situ monitoring of ρ for $Sn_{0.98}Ta_{0.02}O_2$ films grown on various substrates measured in air. Al_2O_3 (0001) single crystalline substrates and glass substrates coated with anatase TiO_2 seed layer are denoted as Al_2O_3 and TiO_2, respectively.

Interestingly, the TTO film showed much larger decrease in n_e of 5×10^{19} cm^{-3} than that in undoped SnO_2, 1.4×10^{18} cm^{-3} with air annealing. I believe that systematically increased n_e values corresponding well to nominal concentrations of dopants such as Ta [15] and Sb [16] is a strong, yet indirect, evidence for the negligible contribution of the intrinsic defects in n_e. However, possible increase of intrinsic defects in doped films, as observed in Ga-doped ZnO [6], might explain the largely decreased n_e in the TTO films with air annealing. In order to obtain insight into the intrinsic defects, namely oxygen vacancies, in TTO, I measured ρ of the TTO films under vacuum, as shown in Fig. D.2. Surprisingly, the vacuum-annealed films showed decrease in n_e similar to that in the air-annealed films. The decrease in n_e insensitive to the annealing ambient suggests that the change in n_e of the annealed TTO films is unassociated with oxygen non-stoichiometry. At present, it is highly challenging to elucidate the mechanism behind the change in transport properties of the annealed films.

Another interesting feature in Fig. D.1 is the marked and probably reversible increase in ρ above 400 ^oC. This behavior may be related to the sensing ability of SnO_2 films [17] although the films in this study are not intended to apply sensors. It is widely believed that grain boundary and molecules reversibly adsorbed there play a critical role in the sensing properties. Therefore, I investigated air annealing effects on films with different structure of grain boundary: TTO films grown on anatase TiO_2 seed layers and Al_2O_3 (0001) single crystalline substrates. As shown in Fig. D.3, these epitaxial TTO films showed highly suppressed increase in ρ above 400 ^oC. This means that high angle grain boundaries and reversibly adsorbed molecules there are crucial for the sensing ability.

From the practical viewpoint, durability against various ambient at high temperatures is important. As shown in Fig. D.3, the TTO films grown on the anatase TiO_2 seed layers showed much lower increase in ρ than the polycrystalline TTO films. The robust conductivity against annealing in air makes the TTO films on the seed layers promising for application that requires high temperature process in air.

Summary

I investigated the effect of post-deposition annealing on the transport properties of undoped SnO_2 and TTO thin films on various substrates under reductive and oxidative annealing ambient. Polycrystalline undoped SnO_2 films with n_e of approximately 5×10^{18} cm^{-3} showed slight decrease in n_e after annealing in air at 600 ^oC. This result is consistent with negligibly slow oxygen diffusion in bulk SnO_2 at this temperature. Polycrystalline TTO films with high n_e of 3.6×10^{20} cm^{-3} showed decrease in n_e of approximately 5×10^{19} cm^{-3} with annealing not only in air but also in vacuum. The insensitiveness to annealing atmosphere suggests that the decrease in n_e is unassociated with oxygen vacancies. Reversible decrease in conductivity was observed in air above 400 ^oC. The response was highly suppressed in epitaxial TTO films, suggesting that the response was derived from reversible adsorption of molecules at the grain boundary of the films. The highly robust conductivity against annealing in air for TTO films grown on anatase TiO_2 seed layers makes them promising for application that requires high temperature process in air.

References

[1] T. Minami, H. Nanto, and S. Takata, Jpn. J. Appl. Phys. **23**, L280 (1984).

[2] T. Minami, H. Nanto, and S. Takata, Jpn. J. Appl. Phys. **27**, L287 (1988).

[3] A. Kitada, S. Kasahara, T. Terashima, K. Yoshimura, Y. Kobayashi, and H. Kageyama, Appl. Phys. Express **4**, 2 (2011).

[4] T. Koida, H. Fujiwara, and M. Kondo, Jpn. J. Appl. Phys. **46**, L685 (2007).

[5] K. Watanabe, M. Hashiguchi, I. Sakaguchi, A. Bryant, Y. Adachi, Y. Zhen, T. Ohgaki, T. Ohsawa, H. Haneda, and N. Ohashi, Appl. Phys. Lett. **104**, (2014).

[6] Y. Sato, H. Makino, N. Yamamoto, and T. Yamamoto, Thin Solid Films **520**, 1395 (2011).

[7] S. Nakao, Y. Hirose, and T. Hasegawa, J. Semicond. **37**, 22001 (2016).

[8] H. Nogawa, T. Hitosugi, A. Chikamatsu, S. Nakao, Y. Hirose, T. Shimada, H. Kumigashira, M. Oshima, and T. Hasegawa, Jpn. J. Appl. Phys. **49**, 41102 (2010).

[9] H. Makino, N. Yamamoto, A. Miyake, T. Yamada, Y. Hirashima, H. Iwaoka, T. Itoh, H. Hokari, H. Aoki, and T. Yamamoto, Thin Solid Films **518**, 1386 (2009).

[10] T. Yamada, A. Miyake, H. Makino, N. Yamamoto, and T. Yamamoto, Thin Solid Films **517**, 3134 (2009).

[11] N. Yamada, I. Yasui, Y. Shigesato, H. Li, Y. Ujihira, and K. Nomura, Jpn. J. Appl. Phys. **39**, 4158 (2000).

[12] T. Minami, T. Miyata, and T. Yamamoto, J. Vac. Sci. Technol. A **17**, 1822 (1999).

[13] K. Goto, T. Kawashima, and N. Tanabe, Sol. Energy Mater. Sol. Cells **90**, 3251 (2006).

[14] J. Mizusaki, H. Koinuma, J.I. Shimoyama, M. Kawasaki, and K. Fueki, J. Solid State Chem. **88**, 443 (1990).

[15] S. Nakao, N. Yamada, T. Hitosugi, Y. Hirose, T. Shimada, and T. Hasegawa, Appl. Phys. Express **3**, 031102 (2010).

[16] M.E. White, O. Bierwagen, M.Y. Tsai, and J.S. Speck, J. Appl. Phys. **106**, 093704 (2009).

[17] S. Das and V. Jayaraman, Prog. Mater. Sci. **66**, 112 (2014).